1965

Use of Mitrovic's method in the analysis of a control system with two gain-variable feedback nonlinearities.

Yockey, Harry M.

Monterey, California: U.S. Naval Postgraduate School

USE OF MITROVIC'S METHOD IN THE ANALYSIS OF A CONTROL SYSTEM WITH TWO GAIN-VARIABLE FEEDBACK NONLINEARITIES

HARRY M. YOCKEY

USE OF MITROVIC'S METHOD IN THE ANALYSIS OF A CONTROL SYSTEM WITH TWO GAIN-VARIABLE FEEDBACK NONLINEARITIES

* * * * *

Harry M. Yockey

USE OF MITROVIC'S METHOD IN THE ANALYSIS OF A CONTROL SYSTEM WITH TWO GAIN-VARIABLE FEEDBACK NONLINEARITIES

By

Harry M. Yockey

Lieutenant, United States Navy

Submitted in partial fulfillment of
the requirements for the degree of

MASTER OF SCIENCE
IN
ELECTRICAL ENGINEERING

United States Naval Postgraduate School
Monterey, California

1965

USE OF MITROVIC'S METHOD IN THE ANALYSIS OF A CONTROL SYSTEM WITH TWO GAIN-VARIABLE FEEDBACK NONLINEARITIES

by

Harry M. Yockey

This work is accepted as fulfilling

the thesis requirements for the degree of

MASTER OF SCIENCE

IN

ELECTRICAL ENGINEERING

from the

United States Naval Postgraduate School

ABSTRACT

The basic Mitrovic's method is an effective technique in the analysis and design of linear feedback control systems. Mitrovic's method has been successfully applied to analyze feedback control systems with single nonlinearities. The objective of this work was to employ Mitrovic's method, which permits the variation of two coefficients of a characteristic equation, in the analysis of a control system with two gain-variable nonlinear feedback paths.

After predictions of system performance were made, the predictions were tested by simulating the feedback control system on a Donner Scientific Corporation analog computer, Model 3100. Computer results were analysed in order to support or reject prediction techniques.

TABLE OF CONTENTS

APPENDICES

LIST OF ILLUSTRATIONS

List of Illustrations (continued)

List of Illustrations (Continued)

LIST OF TABLES

CHAPTER I

USE OF THE BASIC MITROVIC'S METHOD

In general, the analysis and design of feedback control systems centers around the solution to an ordinary, linear, differential equation with constant coefficients. Specifically, the application of LaPlace transforms to the differential equation produces a transfer function which is a ratio of the output signal to the input signal. By proper placement of the poles and zeros of the transfer function, the frequency and/or time response are adjusted to produce results which meet with some set of specifications for the system. This procedure may be followed because the form of the solution to a linear differential equation is unique. The resulting solution is predictable and invariant.

The introduction of a single nonlinear element in a control system produces a nonlinear differential equation where one or more of the coefficients may be variable. There are as many specific solutions to a nonlinear differential equation with variable coefficients as there are values of the coefficients. Therefore, the accurate prediction of system performance is stringently curtailed. The use of describing functions provides an adequate solution to the problem of one nonlinear element within the limitations imposed on the describing function itself.

Consider a feedback control system with a transfer function $G(j\omega)$ and a nonlinear device which may be represented by a describing function $G_D(j\omega)$ both in the forward path as shown in Fig. I-1a. Then the transfer function for this system is:

$$\frac{\theta(s)}{\theta_i(s)} = \frac{G(j\omega)\ G_D(j\omega)}{1 + G(j\omega)\ G_D(j\omega)}\ , \qquad \text{(I-1)}$$

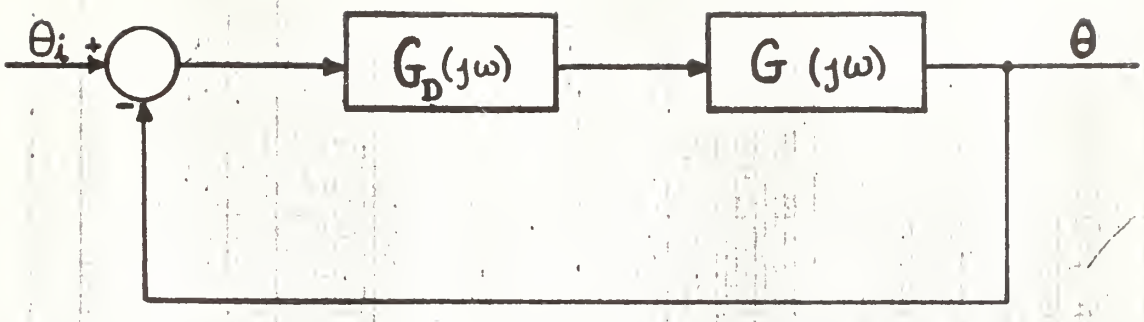

(a) Feedback control system block diagram.

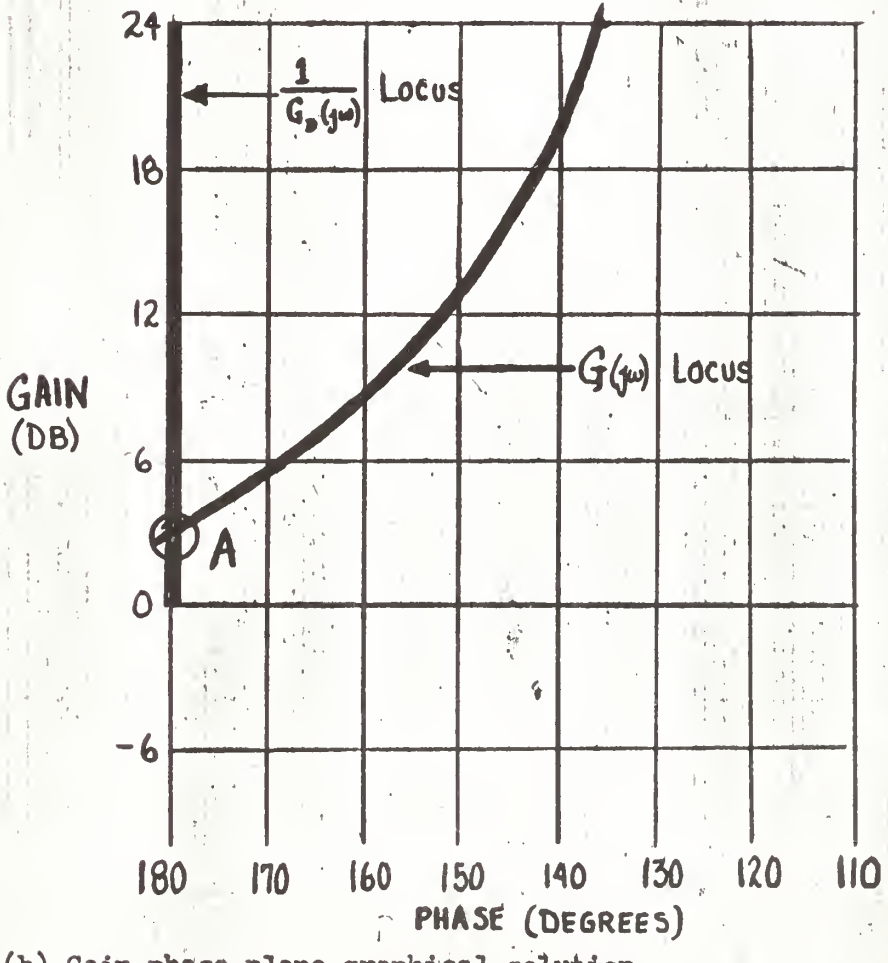

(b) Gain-phase plane graphical solution.

Figure I-1. Control system with single nonlinearity.

from which the characteristic equation may be found by setting the denominator of Eq. (I-1) equal to zero. Thus,

$$1 + G(j\omega) G_D(j\omega) = 0. \tag{I-2}$$

The solution to Eq. (I-2) is:

$$G(j\omega) = - \frac{1}{G_D(j\omega)} . \tag{I-3}$$

Where $G_d(j\omega)$ is a gain nonlinearity only and has no phase angle associated with it - which is the case for such nonlinearities as saturation, ideal relay, dead zone, and relay with dead zone - the problem is conveniently solved on a gain-phase plot. This graphical solution is illustrated in Fig. I-1b. The system operates in a limit cycle at the intersection of the two curves. This is shown as point "A" in the figure. A root-locus plot may be used to arrive at the same result providing the single nonlinear gain is not a function of frequency.

When two nonlinear devices appear in a control system, only a family of gain-phase plots or root-loci plots can provide a complete solution to the problem. Thus the problems of analysis and design become complex and cumbersome. Analysis would be convenient if:

1. Some method of simultaneously looking at two nonlinear gains were available, and,
2. Some relationship between these two nonlinear gains could be found.

Mitrovic's method [1] provides the answer to the first requirement for control systems in which each nonlinear gain appears in a different coefficient of the characteristic equation. The purpose of this thesis is to fulfill the second requirement for a particular feedback control

system.

The mathematical derivation of Mitrovic's method is based on a theorum by Cauchy and will not be pursued here. The algebraic manipulations give some insight into Mitrovic's method and will serve to provide the reader with some feeling for the method.

Consider a feedback control system with a transfer function

$$G(s) = \frac{K}{S(S+p_1)(S+p_2)} . \tag{I-4}$$

The characteristic equation for this system is

$$S^3 + (p_1+p_2)S^2 + p_1p_2S + K = 0 , \tag{I-5}$$

which is of the form

$$A_3S^3 + A_2S^2 + A_1S + A_0 = 0 . \tag{I-6}$$

If the coefficients to be varied are A_0 and A_1 then the characteristic equation may be rewritten as

$$A_3S^3 + A_2S^2 + B_1S + B_0 = 0 , \tag{I-7}$$

where the values of s have the general form of

$$S = -\xi\omega_n + j\omega_n\sqrt{1-\xi^2} \tag{I-8}$$

and lie in the second quadrant of the s-plane. Then the values of s which must be substituted in Eq. (I-7) are:

$$\begin{aligned} S^2 &= \omega_n^2(2\xi^2-1) - j2\xi\omega_n^2\sqrt{1-\xi^2} \\ S^3 &= \xi\omega_n^3(3-4\xi^2) + j\omega_n^3(4\xi^2-1)\sqrt{1-\xi^2} . \end{aligned} \tag{I-9}$$

Substituting the values of s from Eqs. (I-8) and (I-9) in Eq. (I-7) and requiring the real and imaginary parts to go to zero independently

yields:

$$A_3\omega_n^3 + A_2\omega_n^2(2\xi^2-1) - B_1\xi\omega_n + B_0 = 0 \qquad \text{(I-10)}$$

$$j\omega_n\sqrt{1-\xi^2}\left[-A_3\omega_n^3(1-4\xi^2) - A_2 2\xi\omega_n + B_1\right] = 0. \qquad \text{(I-11)}$$

The solution of these two simultaneous equations, after first dividing Eq. (I-11) by $j\omega_n\sqrt{1-\xi^2}$ becomes:

$$B_0 = -\left[A_3\omega_n^3(2\xi) - (1)A_2\omega_n^2\right] \qquad \text{(I-12)}$$

$$B_1 = \left[A_3\omega_n^2(1-4\xi^2) + A_2\omega_n(2\xi)\right].$$

By plotting the results of Eq. (I-12) on a B_0 - B_1 coordinate system for constant ξ lines as ω_n is varied, it is possible to map radial lines from the s-plane onto the B_0 - B_1 plane. Thus the result of simultaneously varying two coefficients of the characteristic equation is plainly evident from a single plot. When the $\xi = 0$ line ($s = j\omega$ in the s-plane) is selected as radial line to be mapped, the stability curve is plotted on the B_0 - B_1 plane.

Mitrovic's method may be expanded to solve any order characteristic equation for any two coefficients. The generalized solutions for Mitrovic's equation pairs are listed in Appendix B, Table I. In a generalized solution, certain functions of ξ only $[\phi_k(\xi)]$ are repeated, such as 2ξ in Eqs. (I-12). A listing of these functions of ξ is made in Appendix B, Table II.

The analysis of feedback control systems with single gain variable nonlinearities using Mitrovic's method is straight forward and produces results consistent with root-locus, describing function, and analog computer techniques. Since the author had no previous experience in

either Mitrovic's method or analysis of feedback control systems with two gain variable nonlinearities, three control systems were selected and analyzed before study on the two gain-variable nonlinear problem was begun. The results of the study of these three systems appear in Appendix A and corroborate the results obtained by LT P. L. WILSON, USN. [6].

CHAPTER II

THE FEEDBACK CONTROL SYSTEM WITH ACCELERATION AND VELOCITY FEEDBACK COMPENSATION

A block diagram of the system to be studied in this thesis is shown in Fig. II-1. The root locus of the transfer function for the system, without acceleration or velocity feedback paths, is plotted on the s-plane in Fig. II-2a. For a gain of 60, the system has complex roots in the right half plane and is unstable. The addition of velocity and acceleration feedback compensation, when saturation is not present, produces a characteristic equation which is

$$s^3 + 63s^2 + 62s + 60 = 0, \qquad \text{(II-1)}$$

when K_a and K_t are both unity.

Eq. (II-1) may be factored to give

$$(s + 62.016) (s^2 + 0.984s + 0.984) = 0. \qquad \text{(II-2)}$$

Thus, the system has been compensated to approximate a second order system with a damping ratio, ζ, equal to 0.5 and a natural frequency, ω_n, equal to 0.984. The root locations for the compensated system are shown in Fig. II-2b. In response to a step input, the system would have a maximum overshoot, M_{pt}, of 1.15 and a settling time of about four seconds.

The addition of two nonlinear elements produces a characteristic equation with two nonlinear coefficients. This equation is:

$$s^3 + (3 + 60N_2K_a)s^2 + (2 + 60N_1K_t)s + 60 = 0 , \qquad \text{(II-3)}$$

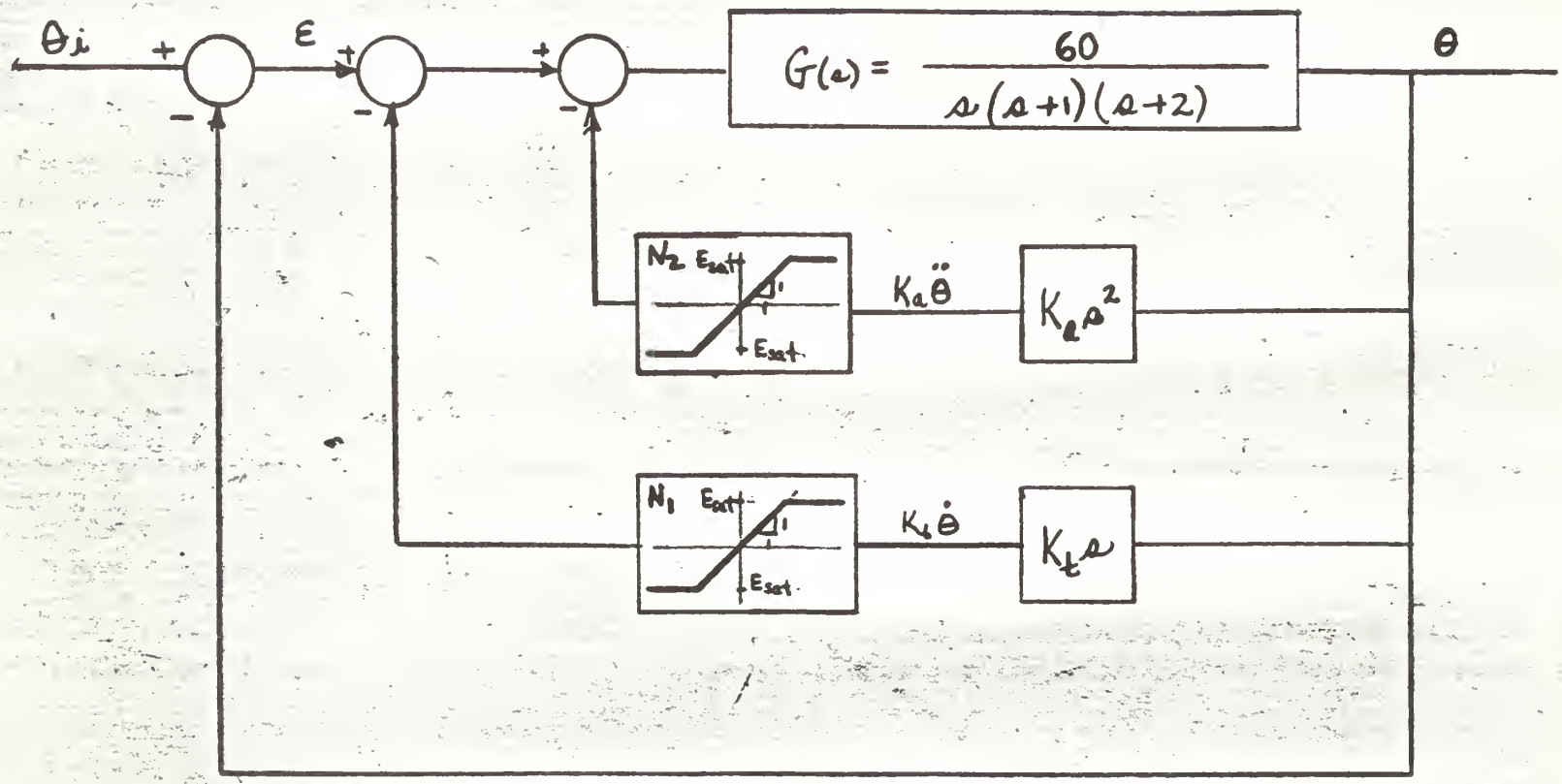

FIGURE II-1

Feedback control system block diagram.

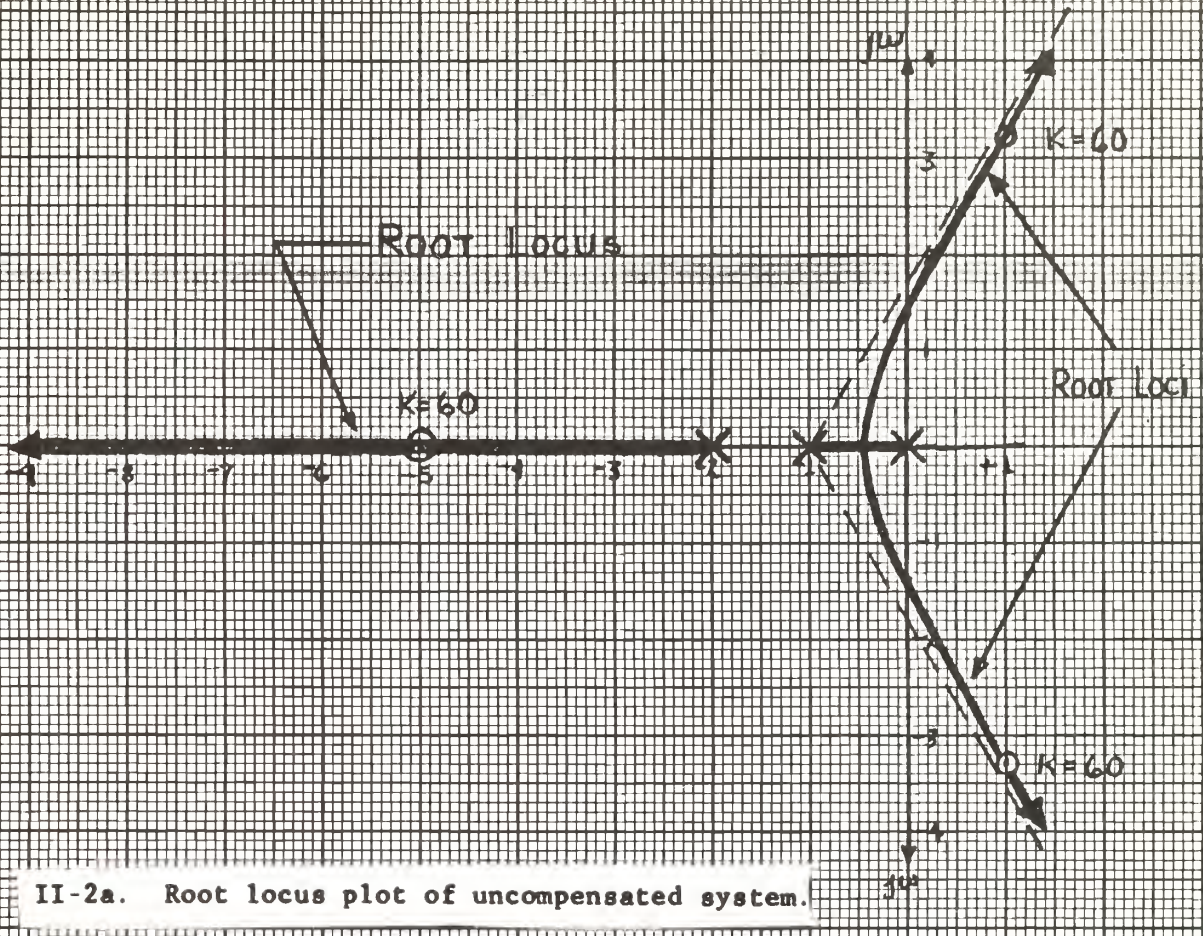

II-2a. Root locus plot of uncompensated system.

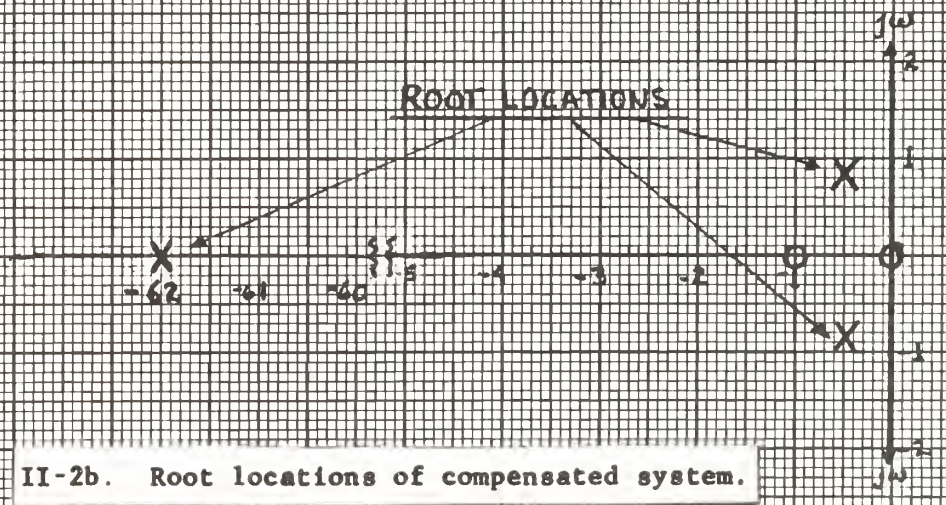

II-2b. Root locations of compensated system.

FIGURE II-2

Root loci of the feedback control system.

where N_1 and N_2 represent the instantaneous gains of the velocity and acceleration saturating amplifiers, respectively. The instantaneous value of N_1 and N_2 may be either unity or a magnitude determined by Eqs. (II-4).

$$N_1 = \frac{E_{sat}}{K_t(\dot{\theta})}$$
$$N_2 = \frac{E_{sat}}{K_a(\ddot{\theta})} \qquad \text{(II-4)}$$

The root locations for Eq. (II-3) vary with time as $\dot{\theta}$ and $\ddot{\theta}$ vary. This is evident if the block diagram is first reduced by including unity feedback.

Then,

$$G_2(s) = \frac{60}{s^3 + 3s^2 + 2s + 60} \qquad \text{(II-5)}$$

and the feedback path is $H(s)$ where

$$H(s) = N_2 K_a s^2 + N_1 K_t s \ . \qquad \text{(II-6)}$$

Therefore, $G_2(s)H(s)$ is found from Eqs. (II-5) and (II-6) as:

$$G_2(s)\,H(s) = \frac{60\,N_2 K_a\, s\left(s + \frac{N_1 K_t}{N_2 K_a}\right)}{s^3 + 3s^2 + 2s + 60} \ . \qquad \text{(II-7)}$$

The location of the system zero at $s = -\frac{N_1 K_t}{N_2 K_a}$ will fluctuate during any given cycle of the system and the gain, given by $60N_2K_a$, will also fluctuate. The difficulties encountered in further root-locus analysis are obvious.

However, there is one useful piece of information which may be gleaned from the root-locus plot. One root of the characteristic equation will

always lie between $5 < s < 62.016$. Therefore, even the nonlinear system will always approximate a second order system since the other two roots will be dominant.

The system of Fig. II-1 was simulated on a Donner Scientific Corporation Analog Computer, Model 3100. The analog computer simulation is shown in Fig. II-3. The $\dot{\theta}$ signal is picked off before the final integration step. The simulation for $\ddot{\theta}$ was accomplished after $\ddot{\theta}$ was derived as shown in Eqs. (II-8).

$$\frac{\dot{\theta}(s)/10}{Y(s)} = \frac{2}{(s+2)}$$

$$s\,\dot{\theta}(s)/10 = 2Y(s) - 2\,\dot{\theta}(s)/10 \qquad \text{(II-8)}$$

$$\ddot{\theta}(s)/10 = 2Y(s) - 2\dot{\theta}(s)/10$$

By using the above method for simulating $\ddot{\theta}$, differentiating circuits, which tend to saturate with steep wavefronts, were avoided. Much of the work involved the use of initial conditions. The initial condition for $\dot{\theta}$ was set first. Then the initial condition of the integrating amplifier, whose output is the signal marked "Y" in Fig. II-3, was adjusted so that the summing amplifier for $\ddot{\theta}$ had the desired initial value of $\ddot{\theta}$ as its output. Since this system does not represent any particular physical system, the terms θ, and its derivatives, inputs, and error signals will be used with units in volts.

The experimental procedure to be followed in this thesis will be to look at the characteristic equation using Mitrovic's method in conjunction with the $B_2 - B_1$ plane. After predictions about system performance are made, the predictions will be tested using the analog computer

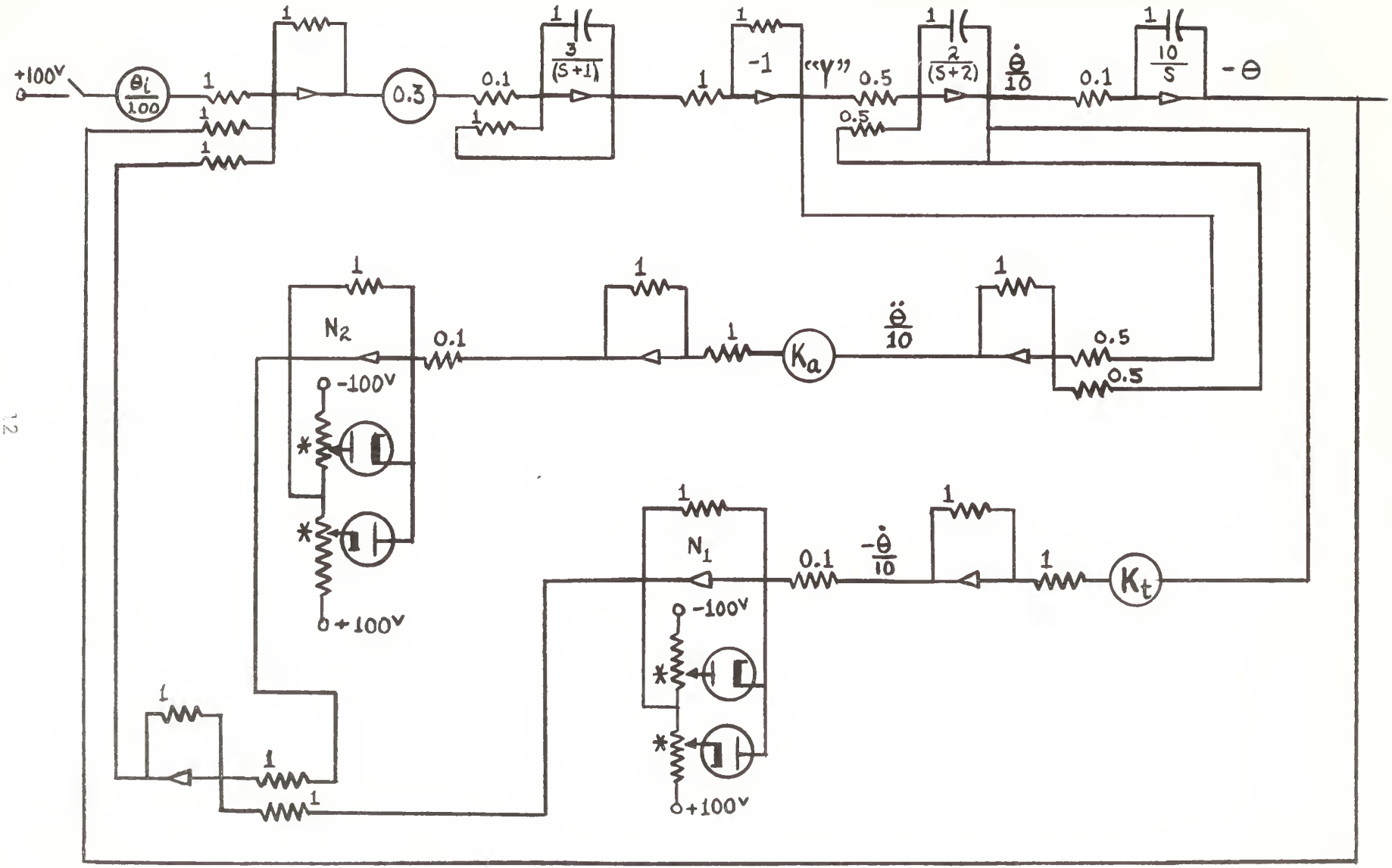

FIGURE II-3

ANALOG COMPUTER SIMULATION. (Resistance in megohms, capacitance in microfarads, *- pot set for saturation voltage)

simulation. The results of computer runs will be analyzed and compared to the predictions which were made. Finally, an attempt will be made to expand any successful methods of predicting performance for application to other systems with two nonlinear elements.

CHAPTER III

MITROVIC'S METHOD APPLIED TO THE CONTROL SYSTEM WITH TWO GAIN-VARIABLE NONLINEARITIES

For the feedback control system described in Chapter II, the characteristic equation may be put in the form:

$$A_3 S^3 + B_2 S^2 + B_1 S + A_0 = 0. \tag{III-1}$$

The appropriate Mitrovic's equation pair from Appendix B is:

$$B_1 = -\frac{1}{\omega_n}\left[A_0 \phi_2(\xi) + A_3 \omega_n^3 \phi(\xi)\right]$$
$$B_2 = \frac{1}{\omega_n^2}\left[-A_0 \phi_1(\xi) + A_3 \omega_n^3 \phi_2(\xi)\right]. \tag{III-2}$$

From Eqs. (III-2) it is evident that the parametric equations for B_1 and B_2 are not functions of the nonlinearities but have constant coefficients which are $A_3 = 1$ and $A_0 = 60$. Substituting these constants and the appropriate $\phi(\xi)$ functions from Appendix B in Eqs. (III-2) results in Eqs. (III-3).

$$B_1 = \frac{60(2\xi)}{\omega_n} + \omega_n^2$$
$$B_2 = \frac{60}{\omega_n^2} + \omega_n(2\xi) \tag{III-3}$$

To study this system for stability only, a mapping of the ξ equals zero line of the s-plane into the $B_1 - B_2$ plane is desired. When ξ equals zero,

$$B_1 = \omega_n^2 \tag{III-4a}$$

and

$$B_2 = \frac{60}{\omega_n^2}. \tag{III-4b}$$

ω_n^2 can be eliminated from Eqs. (III-4). Thus, the parametric equation for stability becomes

$$B_1 B_2 = 60. \qquad \text{(III-5)}$$

When values of B_1 and B_2 which satisfy Eq. (III-5) are plotted on the B_1 - B_2 plane, a graphical solution for the stability curve is obtained. This is shown in Fig. III-1. Also shown in Fig. III-1 is the curve obtained for ζ equal to 0.5.

The values of B_1 and B_2 from the characteristic equation are given by Eqs. (III-6).

$$B_1 = 2 + 60 N_1 K_t$$
$$B_2 = 3 + 60 N_2 K_a \qquad \text{(III-6)}$$

A linear M point may be defined as a point on the B_1 - B_2 plane when the magnitude of the nonlinear gains, N_1 and N_2 in Eqs. (III-6), are unity, i.e., when the system is linear.

With K_a and K_t both equal to one, the linear M-point, from Eqs. (III-6), is at B_1 equal to 62 and B_2 equal to 63. There are minimum values for B_1 and B_2 which occur when $N_1 K_t$ or $N_2 K_a$ become zero. These minimum values are given by Eqs. (III-6) as $B_1 = 2$ and $B_2 = 3$. These minimum regions are lined out on the B_1 - B_2 plane in Fig. III-1. Since N_1 and N_2 can have maximum values of unity, then $B_1 = 62$ and $B_2 = 63$ define an upper limit for M-point movement. These boundaries are shown as dashed lines in Fig. III-1. Therefore, movement of the M-point is completely bounded in a region where $2 = B_1 = 62$ and $3 = B_2 = 63$.

LIMIT CYCLES. There are no limit cycles for this system by the reasons which follow. Eqs. (III-6) may be rewritten as:

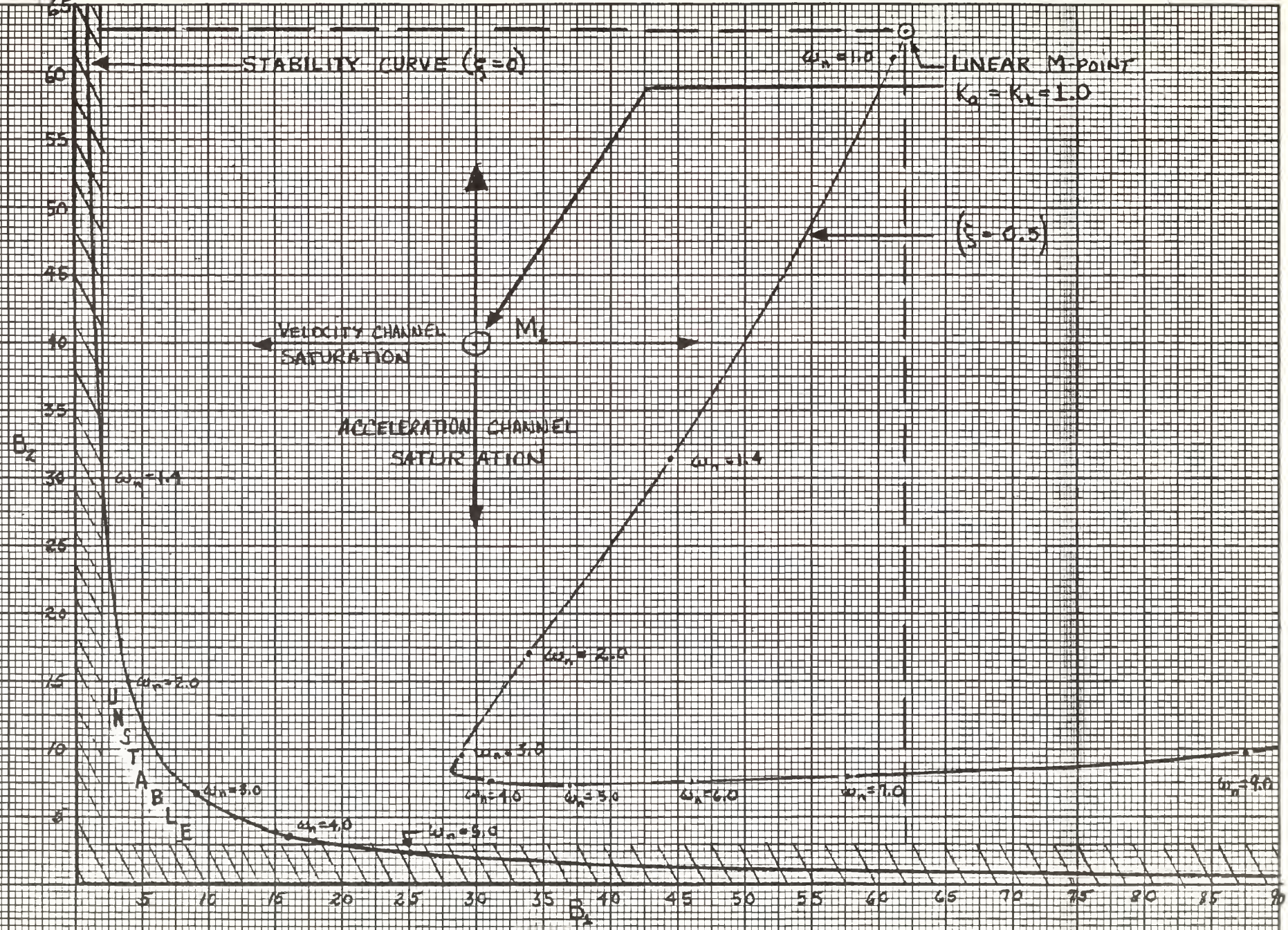

Figure III-1. The B_1 - B_2 plane.

$$B_1 = 2 + \frac{60\,|E_{sat}|}{|\dot{\theta}|}$$

$$B_2 = 3 + \frac{60\,|E_{sat}|}{|\ddot{\theta}|} \qquad \text{(III-7)}$$

If the M-point moves into the unstable region for a significant period of time, the oscillations in the system will tend to grow. This growth results in larger peak magnitudes of acceleration, $\ddot{\theta}$, and velocity, $\dot{\theta}$. As the magnitudes of $\dot{\theta}$ and $\ddot{\theta}$ increase, B_1 and B_2 become smaller, according to Eqs. (III-7), which drives the M-point farther into the unstable region and the peak magnitudes of the oscillations increase even more. Conversely, if the M-point does not move into the unstable region, the peak magnitudes of any oscillations would decrease and the M point would move in the direction of the linear M-point. In theory a limit cycle could exist. However, it would be an unstable limit cycle and the slightest deviation from such a limit cycle would create either a stable or an unstable system. Therefore, in the actual system no limit cycles can exist and none were found.

M POINT MOTION. The M-point does not move in a linear system. Therefore, operation of the system is defined by the M-point location, two roots are specified ($s = -\zeta\omega_n \pm j\omega_n\sqrt{1-\zeta^2}$), the third root can be found, and system performance can be predicted. The M-point location on the B_1 - B_2 plane can be adjusted to give any desired value of ζ and ω_n by adjusting the acceleration and velocity feedback gains.

If only the tachometer feedback channel saturates, M-point motion is along a horizontal line since B_1 can vary but B_2 is fixed by the value of acceleration feedback gain. Conversely, if only the acceleration feedback channel saturates, movement of the M-point would be along

a vertical path.

When both feedback paths saturate, the M-point can move anywhere in the $B_1 - B_2$ plane within the boundaries previously defined. The exact nature of the M-point motion can be predicted only if the exact $\dot{\theta}$ vs $\ddot{\theta}$ phase portrait can be predicted. However, a qualitative description of M point motion can be made using only a few approximations.

Consider the transfer function of the linear system:

$$\frac{\theta(s)}{\theta_i(s)} = \frac{60}{s^3 + 63s^2 + 62s + 60},$$

which may be rearranged as

$$\theta(s)\left(s^3 + 63s^2 + 62s + 60\right) = 60\,\theta_i(s). \qquad \text{(III-8)}$$

An approximation of Eq. (III-8) is made by factoring out $s + 62.016$ from the left side of the equation and discarding this term. Then, Eq. (III-8) becomes:

$$\theta(s)\left(s^2 + .984s + .984\right) \cong 60\,\theta_i(s). \qquad \text{(III-9)}$$

For zero input to the system, Eq. (III-9) becomes

$$\theta(s)\left(s^2 + .984s + .984\right) \cong 0. \qquad \text{(III-10)}$$

Eq. (III-10) may be changed to an approximate differential equation for the system which is:

$$\ddot{\theta} + \dot{\theta} + \theta \cong 0 \qquad \text{(III-11)}$$

Within the tolerances of the approximations made, Eq. (III-11) will govern the linear system. If the system is driven by initial conditions, then, at $t = 0+$, Eq. (III-11) must be satisfied. Also, at $t = 0+$, θ

has not had time to change from its initial value. If $\dot{\theta}(0)$ is zero, then,

$$\ddot{\theta} \cong -\dot{\theta} \qquad \text{for } 0 < t < 0+ . \qquad \text{(III-12)}$$

To test the validity of the assumptions which have been made, the linear system was checked out on the analog computer. Fig. III-2 is a phase portrait of the $\dot{\theta}$ vs $\ddot{\theta}$ plane. In the brief time when $0 < t < 0+$, the approximation given by Eq. (III-12) applies. This time period is indicated by the 24 single trace lines in Fig. III-2. Regardless of the initial value of acceleration, when $\dot{\theta}(0) = 35$ volts, $\ddot{\theta}(0+) = -35$ volts. After $t = 0+$, each of the 12 runs for positive values of $\dot{\theta}(0)$ have essentially the same phase portrait. Similarly, each of the 12 runs for negative values of $\dot{\theta}(0)$ have the same phase portrait after $t = 0+$. (It is interesting to note here that, if the s^3 term were eliminated from Eq. (III-8), no significant difference in the ensuing Eqs. (III-10, 11, and 12) would have resulted. Use of this fact is made at a later point in this chapter.)

Consider this system operating in an underdamped condition. The system is then oscillatory. If the velocity has a sinusoidal waveshape, the acceleration has a sinusoidal waveshape which will lead the velocity waveshape by 90 degrees. When the velocity is at a positive or negative maximum, the acceleration will be zero.

If the criteria developed through the aid of the assumptions in the preceding paragraphs are applied to the B_1-B_2 plane, a qualitative description of M-point motion can be made. Assume the analysis of M-point motion is begun when the velocity passes through a maximum value. The acceleration is, therefore, zero and the acceleration feedback channel is linear. Figure III-3 shows the location of this point as M_1. When

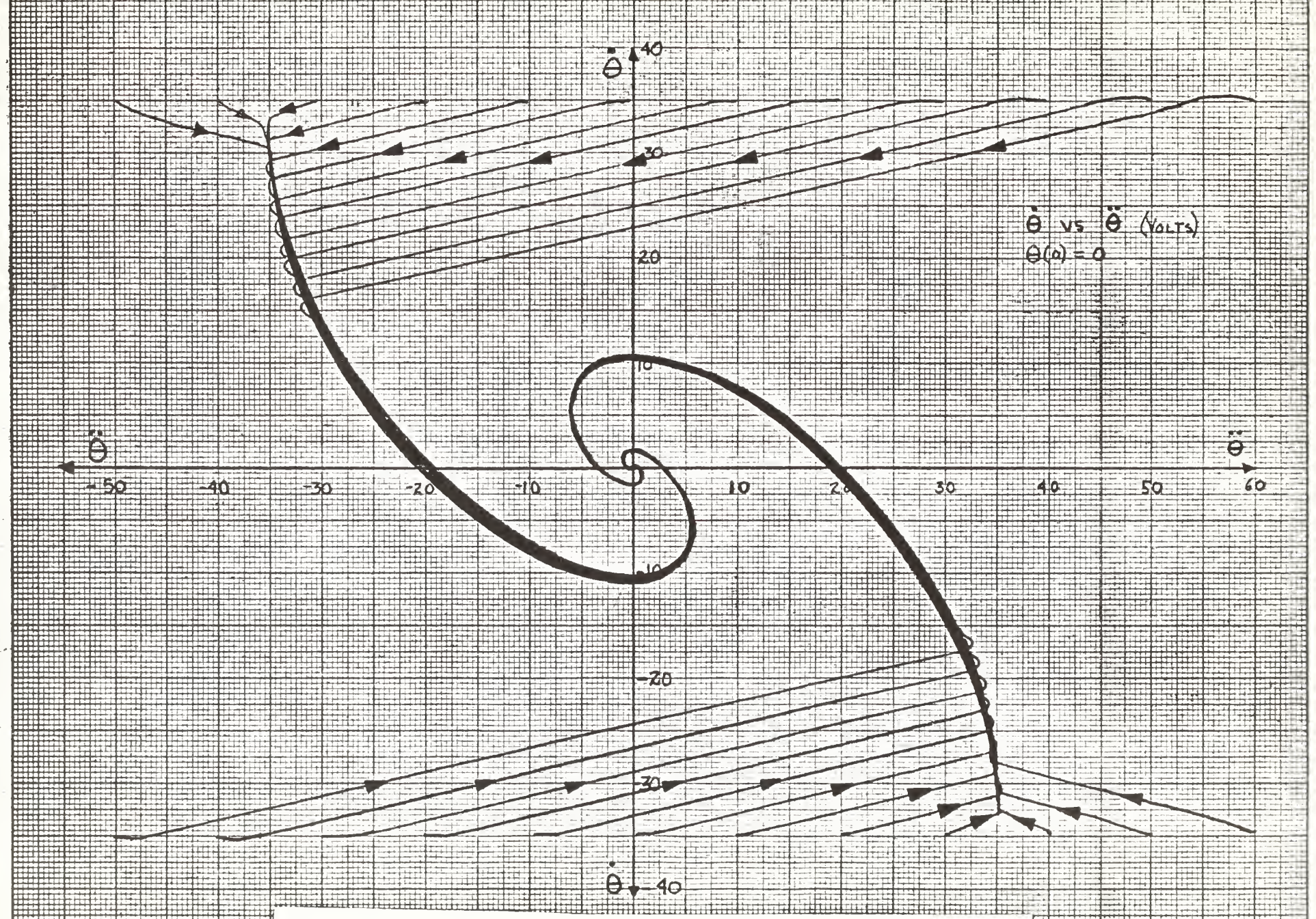

Figure III-2. Phase portrait of the $\dot{\theta}$ vs $\ddot{\theta}$ plane, linear system.

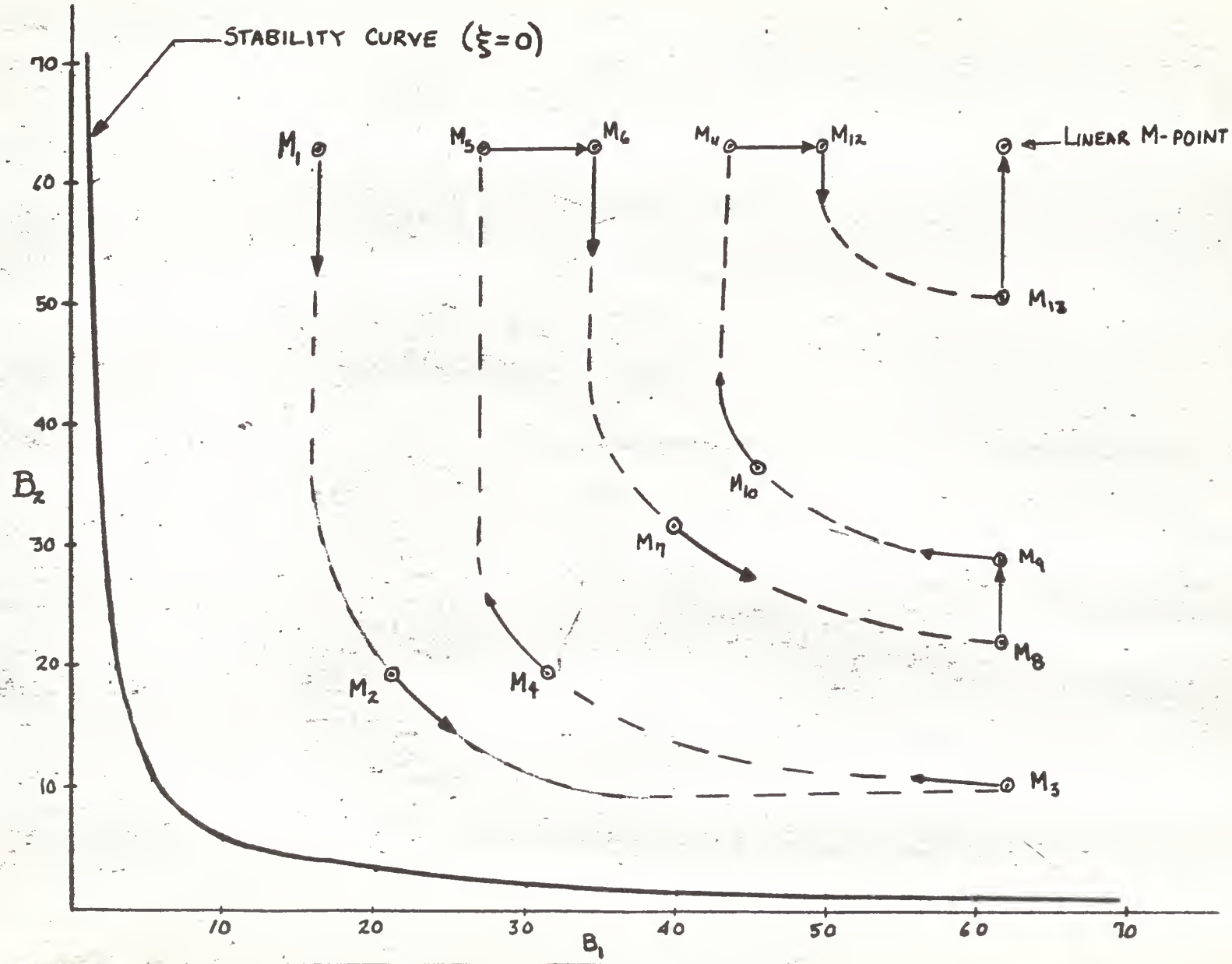

Figure III-3. Predicted M-point motion on the B_1 - B_2 plane.

the magnitude of the acceleration becomes greater than the saturation voltage the magnitude of B_2 decreases according to Eq. (III-7) and the M point moves downward as shown by the arrow from M_1 in Fig. III-3. This motion would continue until the velocity begins to change its magnitude, say at M_2. When this happens, the velocity feedback amplifier saturates to a lesser degree and B_1 begins to increase. The M-point motion is then shown by the arrow from M_2. A short time later the velocity channel goes out of saturation and the acceleration channel reaches a maximum degree of saturation. The M-point has then moved to M_3. As the velocity channel is driven into saturation in the opposite direction and the acceleration channel becomes saturated to a lesser degree, the M-point moves away from M_3 in the direction indicated. Assuming a damped system, the M-point could then pass through M_4 and arrive at M_5. If, at M_5, the acceleration channel remains unsaturated for an appreciable amount of time, the M-point would move in the indicated direction as the magnitude of the velocity signal decreases. At M_6 the acceleration channel saturates again and the entire process is repeated through M_7 to M_8. At M_8 the velocity channel remains unsaturated as the acceleration magnitude decreases to M_9. This process continues until the linear M-point is reached, after which neither channel saturates. The above discussion has been for a theoretical M-point motion. Before taking up actual M point movement, the theoretical aspects of stability will be discussed.

STABILITY

Theoretically, if the system begins operation in the stable region of the B_1 - B_2 plane, there is some damping ratio, ζ, which will

cause the system to have successively smaller peak signals at the maximum of each complete cycle or half-cycle. Therefore a stable system would remain stable and M-point motion would follow a trajectory similar to that shown in Fig. III-3. Conversely, if the system begins operation in the unstable region, then a growth in the peak magnitudes of each succeeding cycle occurs and the system can only remain unstable. However, from Fig. III-4, a set of initial conditions can be imposed on the system so as to place the M-point in the unstable region, say at M_0. An unstable system may be cyclic as well as unstable. For a cyclic system driven with initial conditions, $\dot{\theta}$ and $\ddot{\theta}$ will pass through zero. As either one passes through zero the nonlinearity imposed on the system by saturation is removed. On the B_1 - B_2 plane, if the value of either parameter is the same as the value at the linear M-point, the instantaneous M-point in question must lie in the stable region. (M_1). Additionally, at any instant when B_1 is greater than 20 ($\dot{\theta} <$ 10 volts) or B_2 is greater than 30 ($\ddot{\theta} <$ 6.66 volts) the instantaneous M-point must lie inside the stable region (M_3).

Therefore, for the non-linear system, the stability curve is not an inviolate boundary! It must be possible to start in the unstable region and pass into the stable region. Two questions then arise.

1. Can a system be started in the stable region and become unstable?

2. Can a system be initially unstable and go stable?

Equation (III-10) was obtained by assuming that the system at hand was essentially a second order system. As previously stated, the same result would have been obtained if the s^3 factor had been dropped from Eq. (III-8). Equation (III-13) results when the s^3 factor is disregarded but the non-linear coefficients are retained.

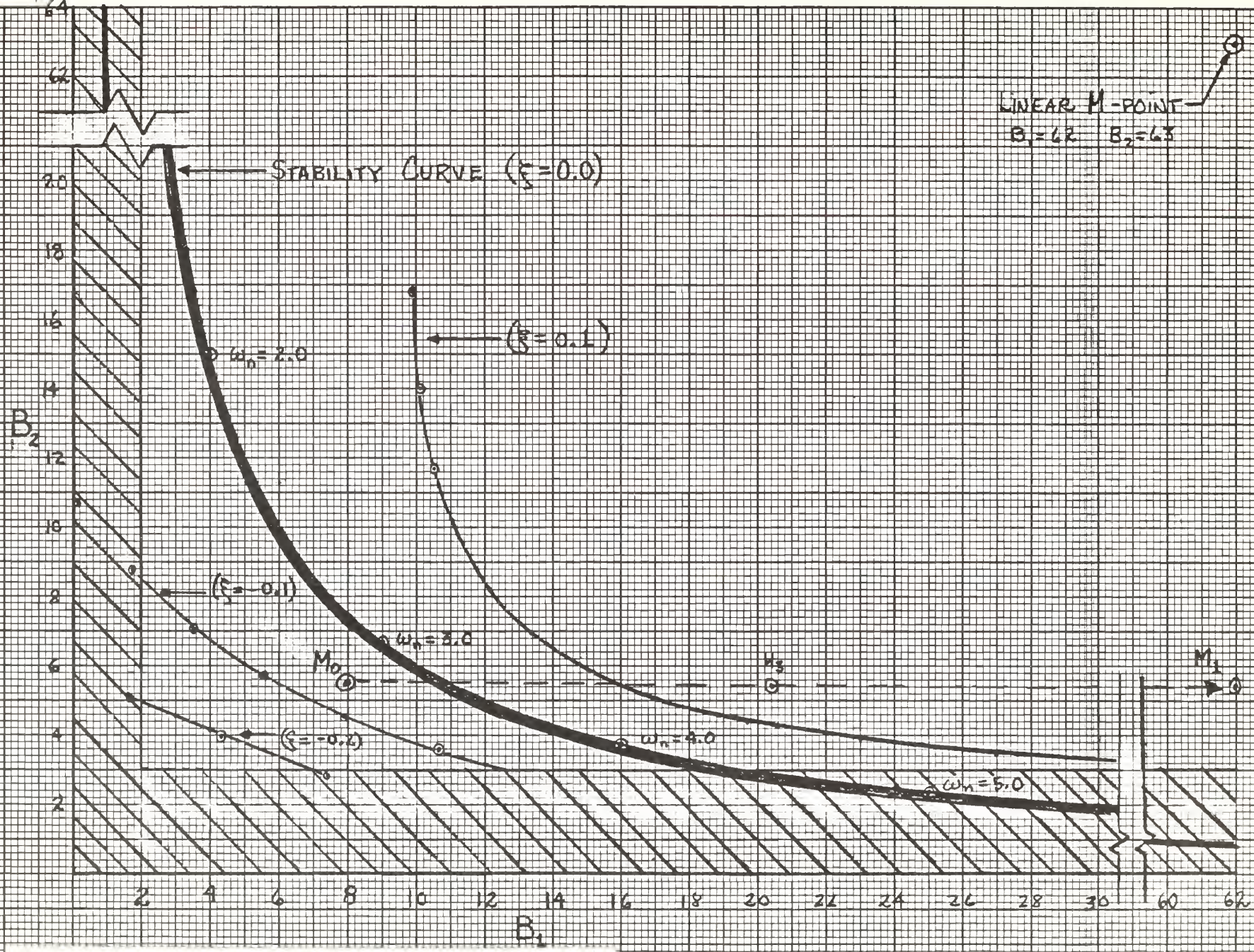

Figure III-4. Expanded view of the B_1 - B_2 plane.

$$\theta(s)\left[(3+60N_2K_a)s^2+(2+60N_1K_t)s+60\right]\cong 0. \qquad \text{(III-13)}$$

Thus, the non-linear differential equation is approximated by:

$$(3+60N_2K_a)\ddot{\theta}+(2+60N_1K_t)\dot{\theta}+60\theta\cong 0. \qquad \text{(III-14)}$$

To move the M-point to a desired location as a starting point, initial conditions are imposed on $\dot{\theta}$ and $\ddot{\theta}$ while $\theta(0) = 0$. Thus, Eq. (III-14) may be rewritten with the values of the nonlinear gains inserted and for the time period $0 < t < 0+$ as,

$$\left(3+\frac{180}{|\dot{\theta}|}\right)\ddot{\theta}+\left(2+\frac{180}{|\dot{\theta}|}\right)\dot{\theta}\cong 0 \qquad \text{(III-15)}$$

for $E_{sat} = \pm 3$ volts in each channel.

Consider initial conditions of $\dot{\theta}(0) = +30$ volts and $\ddot{\theta}(0) = +10$ volts. This condition places the M-point at M_0 in Fig. III-5. If Eq. (III-15) is rearranged as Eq. (III-16) and solved for $\ddot{\theta}$ when $\dot{\theta} = +30$ volts then, $\ddot{\theta} = -140$ volts and B_2, the coefficient for $\ddot{\theta}$, will be at 4.29 shown as M_2.

$$\ddot{\theta} = -\frac{2\dot{\theta}(0)}{3}-60\left[\operatorname{sign}\dot{\theta}(0)+\operatorname{sign}\ddot{\theta}(0)\right] \qquad \text{(III-16)}$$

In order for $\ddot{\theta}(0+)$ to arrive at -140 volts, it must pass through zero. Therefore, M-point motion would be through M_1 to M_2 and the system would be driven immediately into the unstable region.

Consider the same M_0 point but with $\dot{\theta}(0) = -30$ volts. Then the solution to Eq. (III-16) is $\ddot{\theta} = +20$ volts and the M-point of $t = 0+$ would be driven to M_3 without passing through M_1.

If the system is started at M_{10} by having $\dot{\theta}(0) = +10$ volts and $\ddot{\theta}(0) = +60$ volts, where would the M-point be at $t = 0+$? Again, Eq.

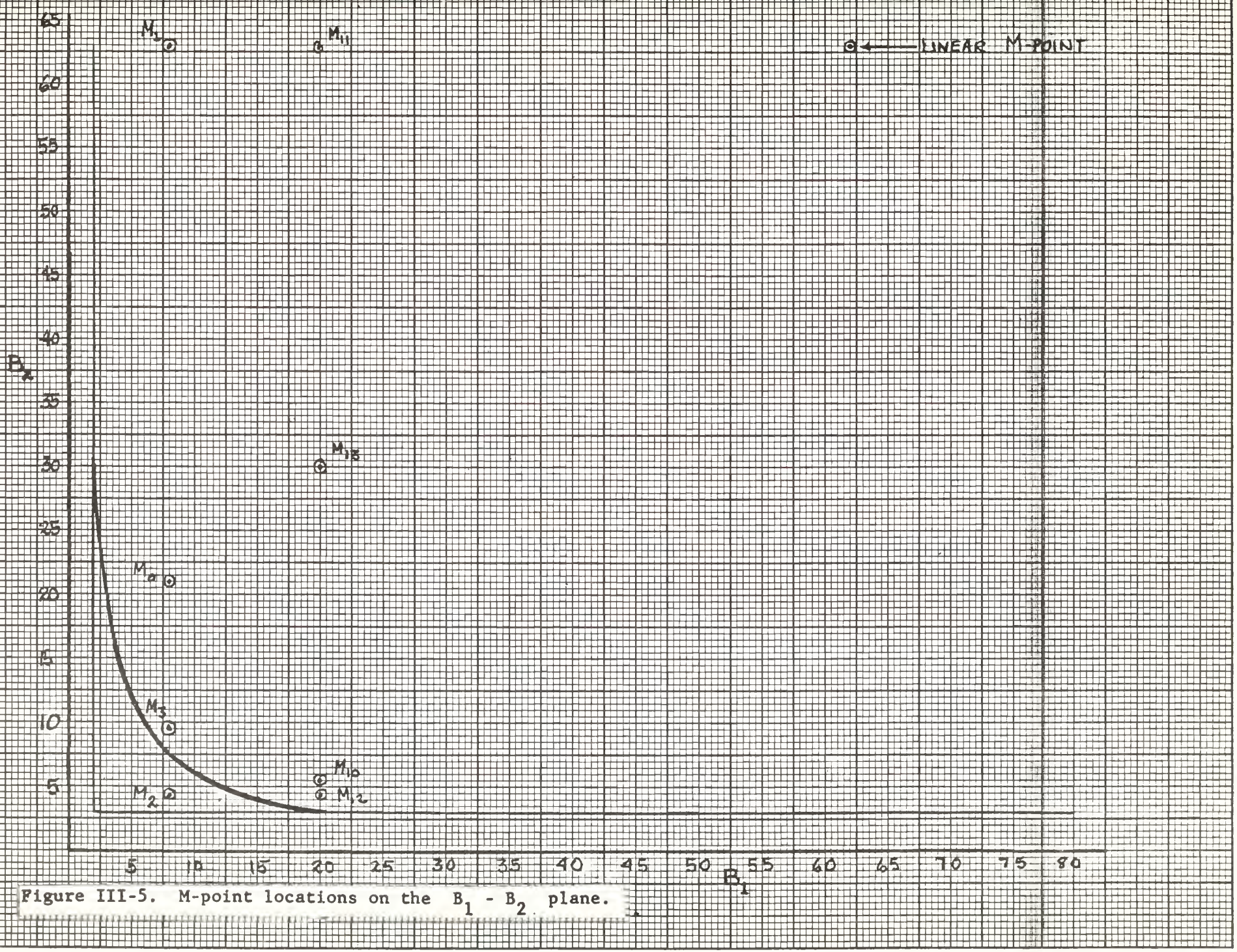

Figure III-5. M-point locations on the B_1 - B_2 plane.

(III 16) is solved for $\ddot{\theta}$. The solution is $\ddot{\theta}$ = -126 volts and, therefore, B_2 = 4.43. The M-point would move to M_{12} passing through M_{11}. For $\dot{\theta}(0)$ = -10 volts and $\ddot{\theta}(0)$ = +60 volts, then $\ddot{\theta}(0+)$ would be +6.7 volts (B_2 = 30). This sequence drives the M-point to M_{13} without passing through M_{11}.

Although the above discussion is based on approximations, some idea of initial M-point movement has been obtained. When initial conditions are imposed on $\dot{\theta}$ and $\ddot{\theta}$ so that they both have the same sign, the system apparently would be hit harder than if $\dot{\theta}$ and $\ddot{\theta}$ were of opposite sign. Thus, the question of stability would hinge, in part, on the question of the sign of the initial conditions imposed.

When Eq. (III-16) is solved for $\ddot{\theta}$ under varying initial conditions for $\dot{\theta}$ and $\ddot{\theta}$, Table III-1 results. In lieu of all the approximations which have been made, Table III-1 can not be regarded as an exact prediction of system stability. It does indicate the type of initial condition settings which would tend to make the system stable, marginally stable, or completely unstable. At this point it is concluded that experimental tests must be conducted to determine stability limits for this system.

To investigate stability, the system was driven with various initial conditions. The starting point on the B_1 - B_2 plane is defined by the magnitudes of the $\dot{\theta}$ and $\ddot{\theta}$ initial conditions. The $\dot{\theta}$ vs $\ddot{\theta}$ phase plane was selected as the appropriate method of recording data because of the direct correlation between this phase plane and the B_1 - B_2 plane.

After conducting several computer runs, it became obvious that some regions of the $\dot{\theta}$ vs $\ddot{\theta}$ plane would produce stable runs and some regions would produce an unstable system. To delineate the stable region, the

TABLE III-1

$\dot{\theta}(0)$	$\ddot{\theta}(0)$	$B_1(0)$	$B_2(0)$	Initially: Stable (S) Unstable (U)	$\ddot{\theta}(0+)$	$B_2(0+)$	Predicted: Stable (S) Unstable (U) Marginal (S/U)
+15	+30	14	9	S	-130	4.38	S/U
+15	+60	14	6	S	-130	4.38	S/U
+15	+90	14	5	S	-130	4.38	S/U
+15	-30	14	9	S	- 10	21.00	S
+15	-60	14	6	S	- 10	21.00	S
+15	-90	14	5	S	- 10	21.00	S
-15	+30	14	9	S	+ 10	21.00	S
-15	+60	14	6	S	+ 10	21.00	S
-15	+90	14	5	S	+ 10	21.00	S
-15	-30	14	9	S	+130	4.38	S/U
-15	-60	14	6	S	+130	4.38	S/U
-15	-90	14	5	S	+130	4.38	S/U
+30	+30	9	9	S	-140	4.29	U
+30	+60	9	6	U	-140	4.29	U
+30	+90	9	5	U	-140	4.29	U
+30	-30	9	9	S	- 20	12.00	S
+30	-60	9	6	U	- 20	12.00	S
+30	-90	9	5	U	- 20	12.00	S
-30	+30	9	9	S	+ 20	12.00	S
-30	+60	9	6	U	+ 20	12.00	S
-30	+90	9	5	U	+ 20	12.00	S
-30	+30	9	9	S	+140	4.29	U
-30	-60	9	6	U	+140	4.29	U
-30	-90	9	5	U	+140	4.29	U

$\dot{\theta}$ vs $\ddot{\theta}$ phase plane was searched until a stable run resulted from one initial condition but, an unstable run resulted from an initial condition displaced a small distance from the original starting point. Figures III-6a through III-6g are a sampling of these type runs. When the locus of all stable starting points is drawn, the $\dot{\theta}$ vs $\ddot{\theta}$ phase plane is divided into a stable region and an unstable region. This is shown in Fig. III-7. For all these runs, θ (0) equals zero.

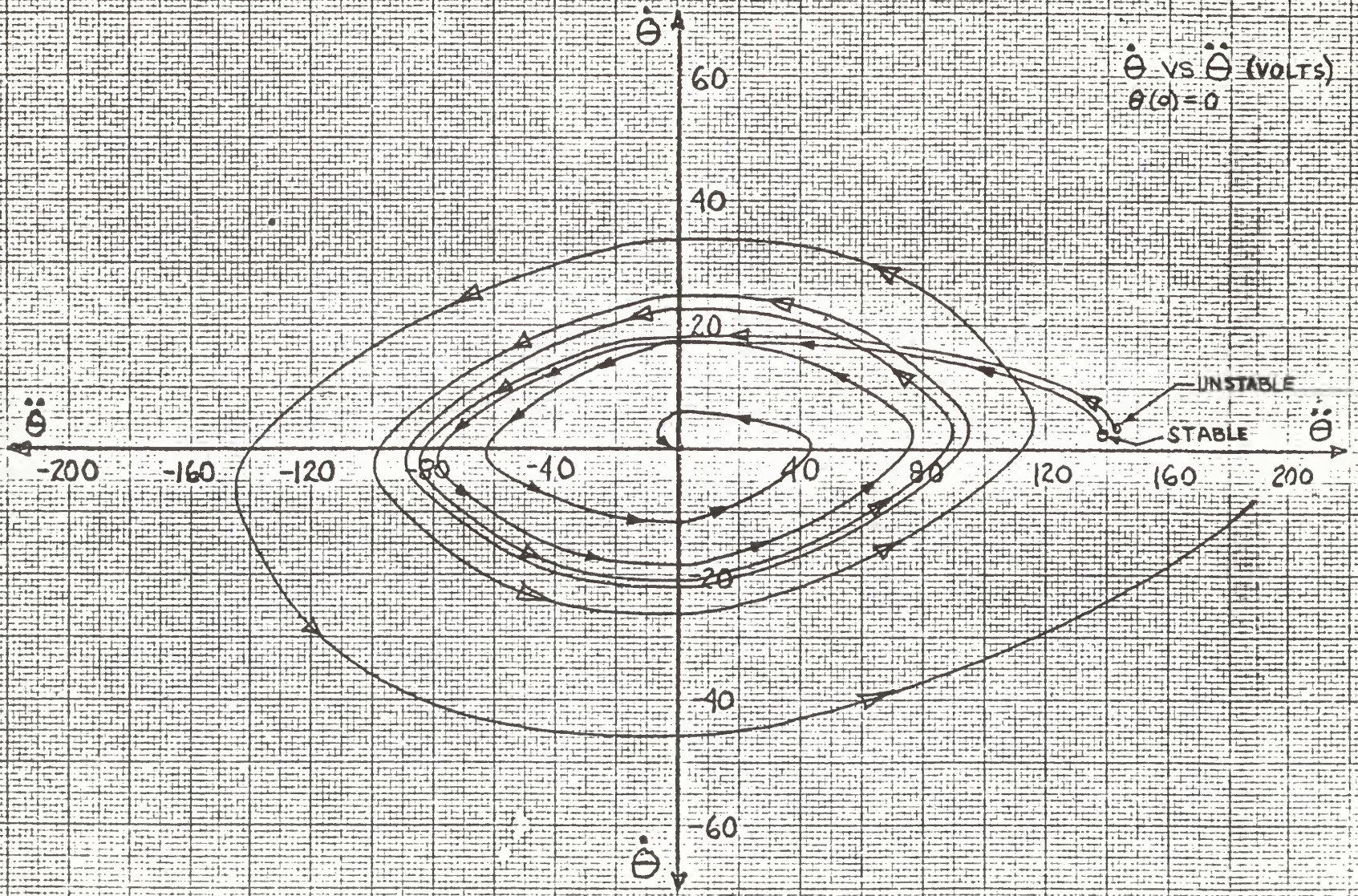

Figure III-6a. $\dot{\theta}$ vs $\ddot{\theta}$ trajectories.

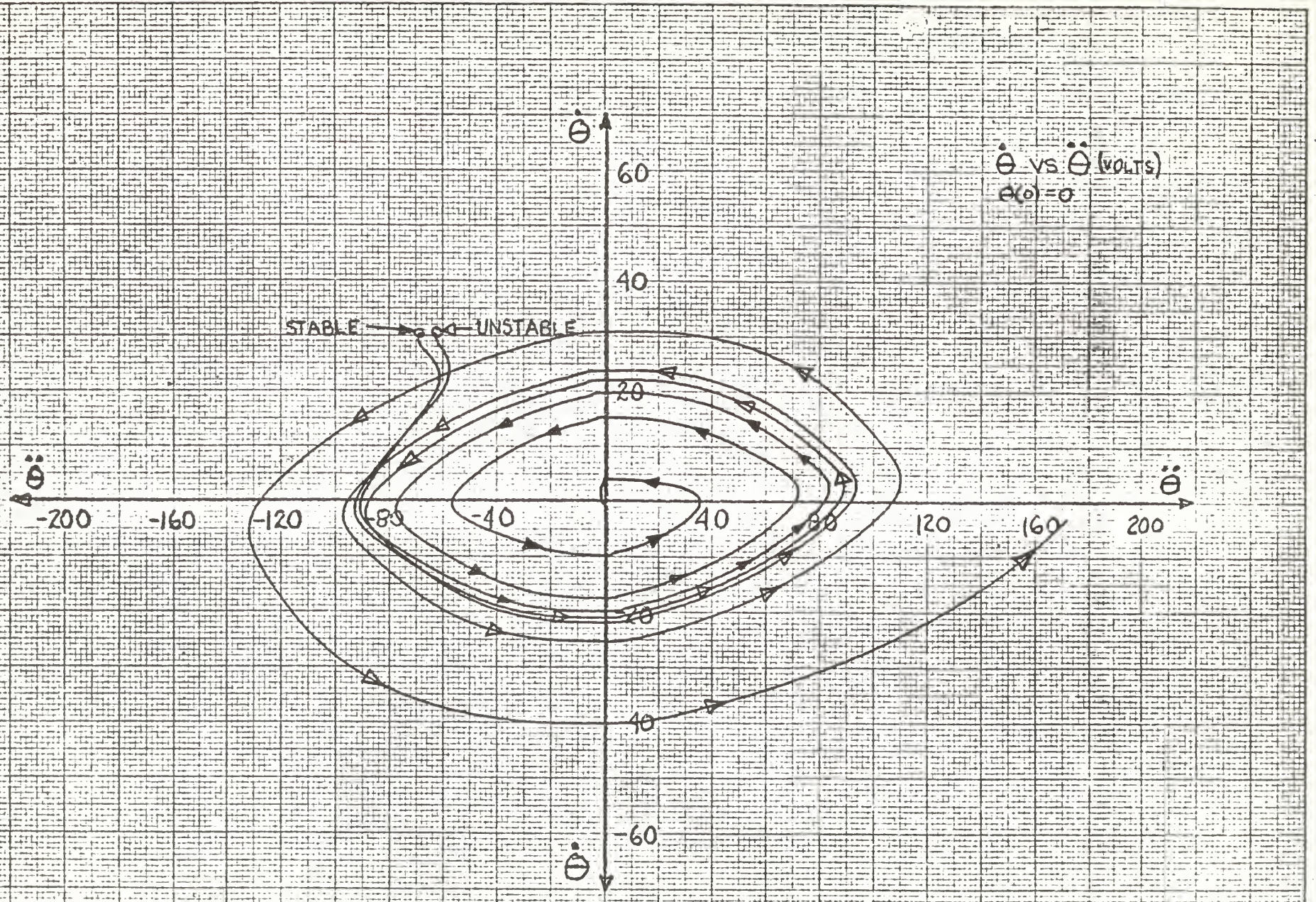

Figure III-6b. $\dot{\theta}$ vs $\ddot{\theta}$ trajectories.

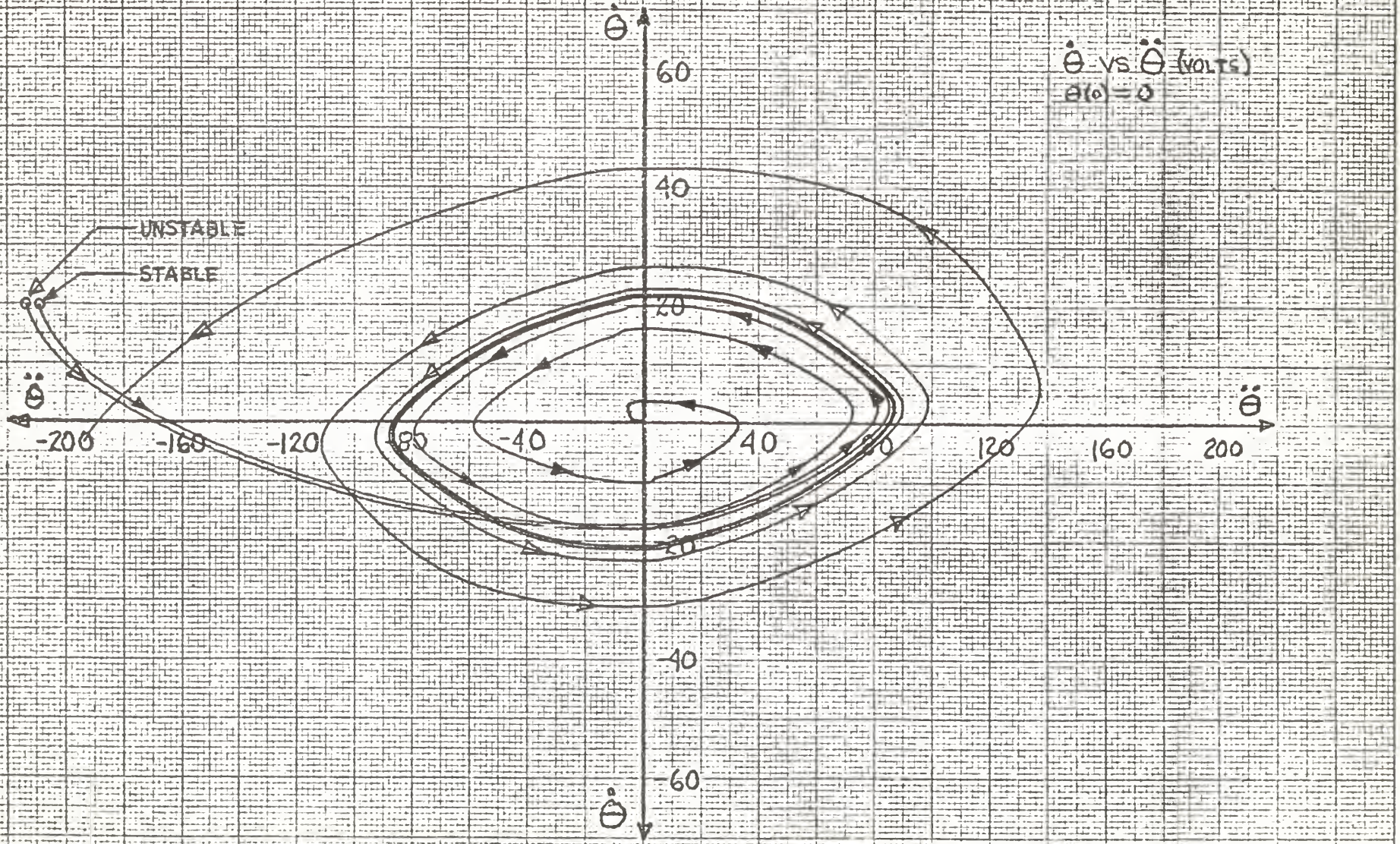

Figure III-6c. $\dot{\theta}$ vs $\ddot{\theta}$ trajectories.

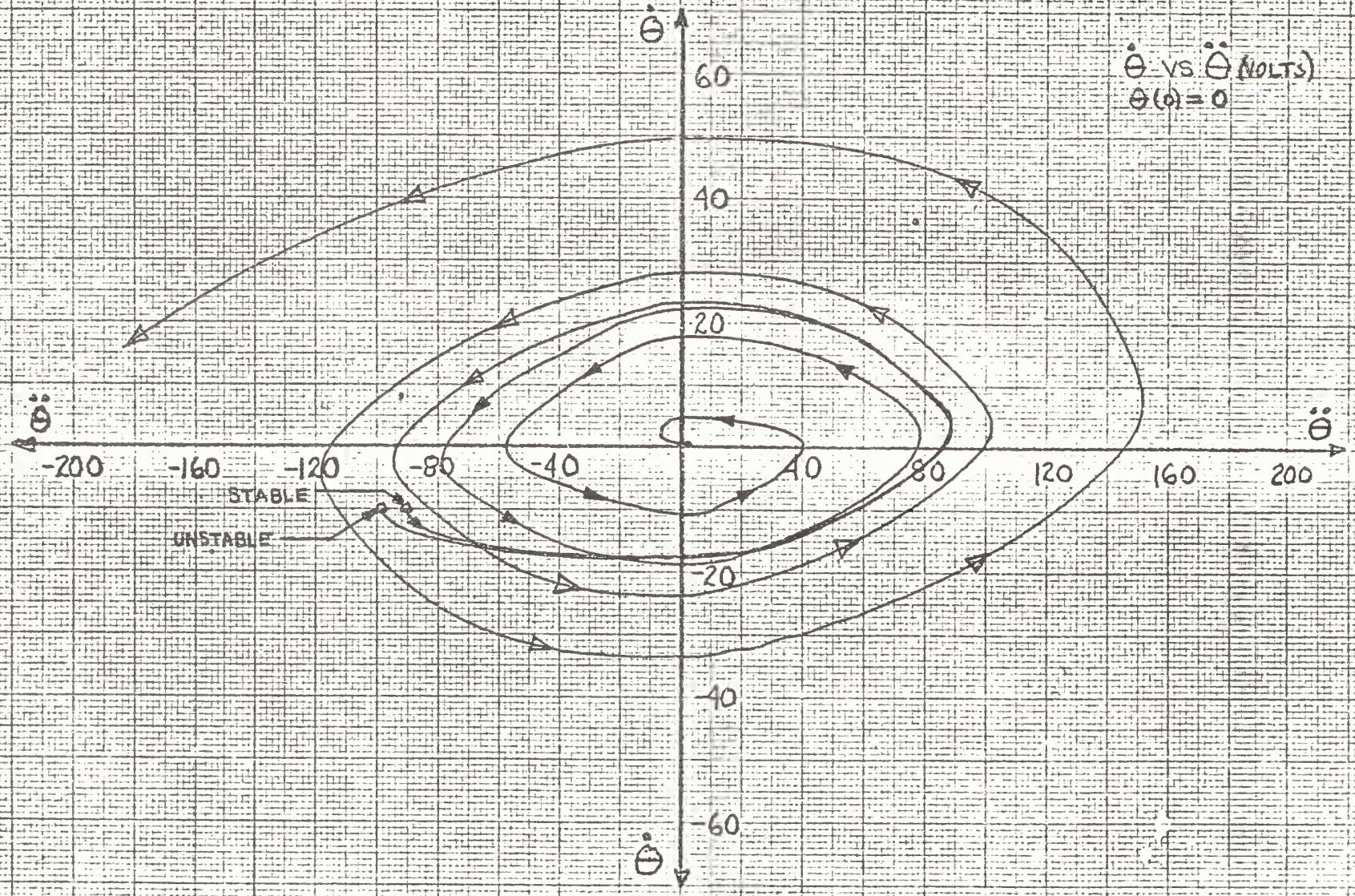

Figure III-6d. $\dot{\theta}$ vs $\ddot{\theta}$ trajectories.

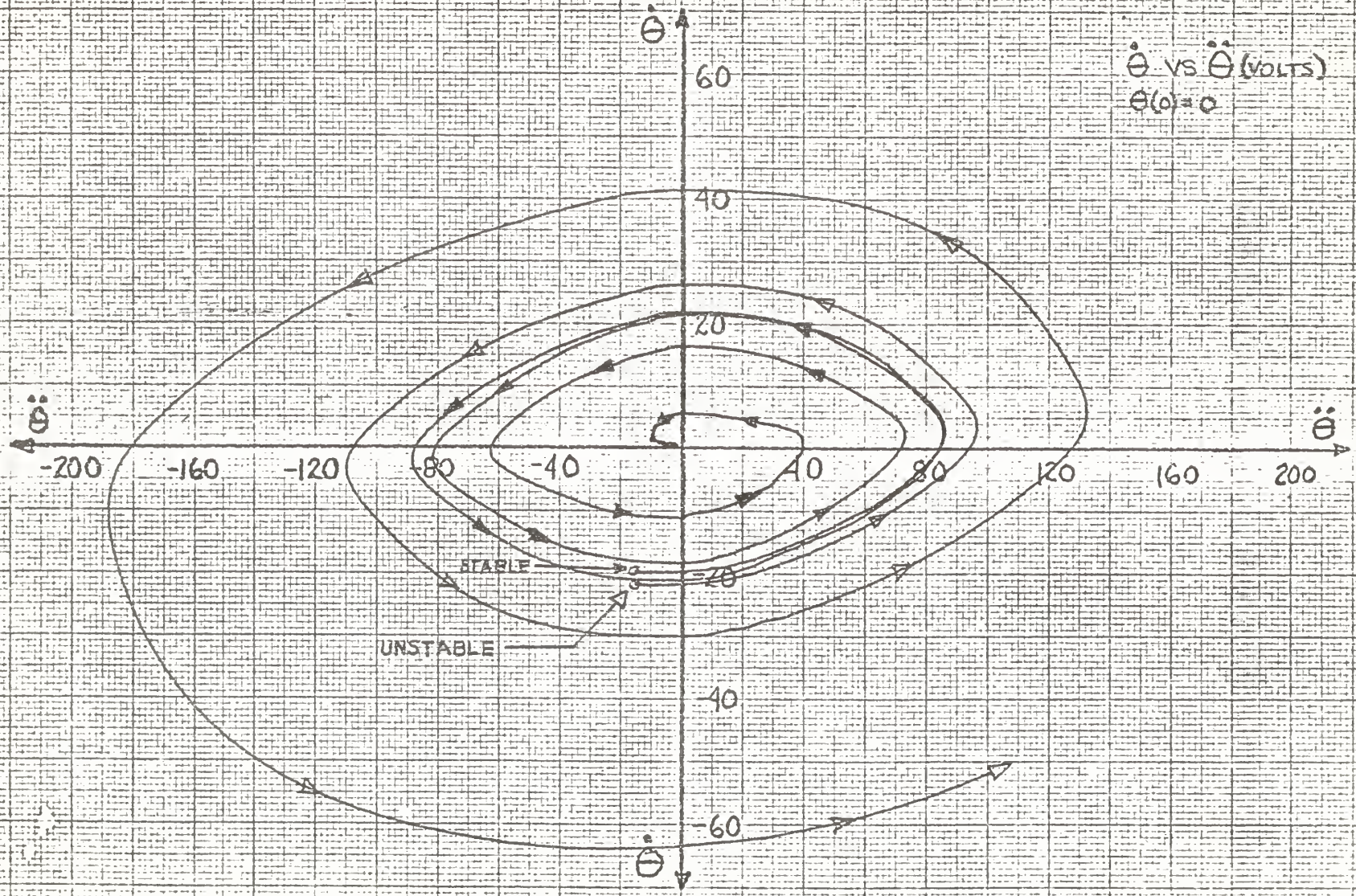

Figure III-6e. $\dot{\theta}$ vs $\ddot{\theta}$ trajectories.

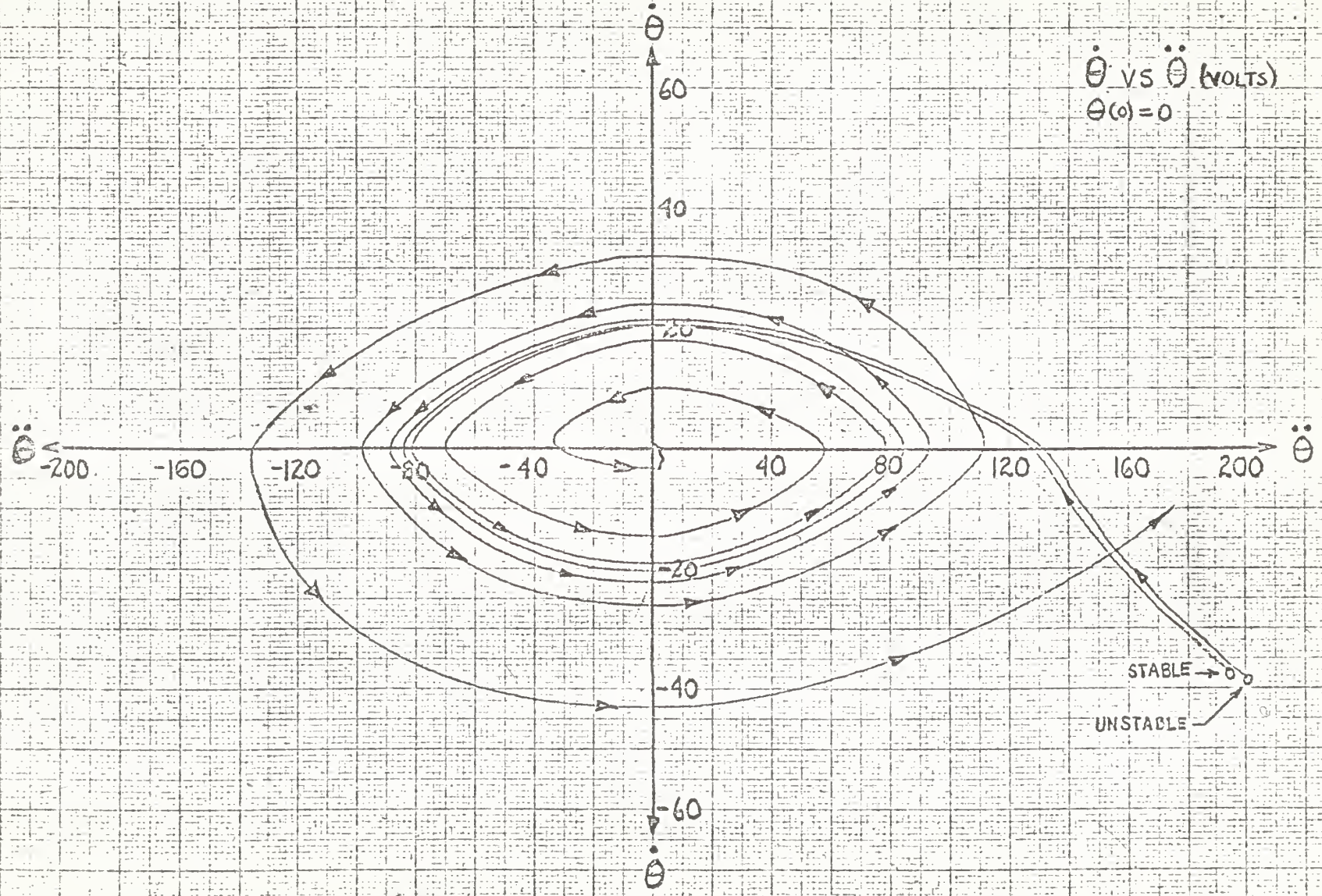

Figure III-6f. $\dot{\theta}$ vs $\ddot{\theta}$ trajectories.

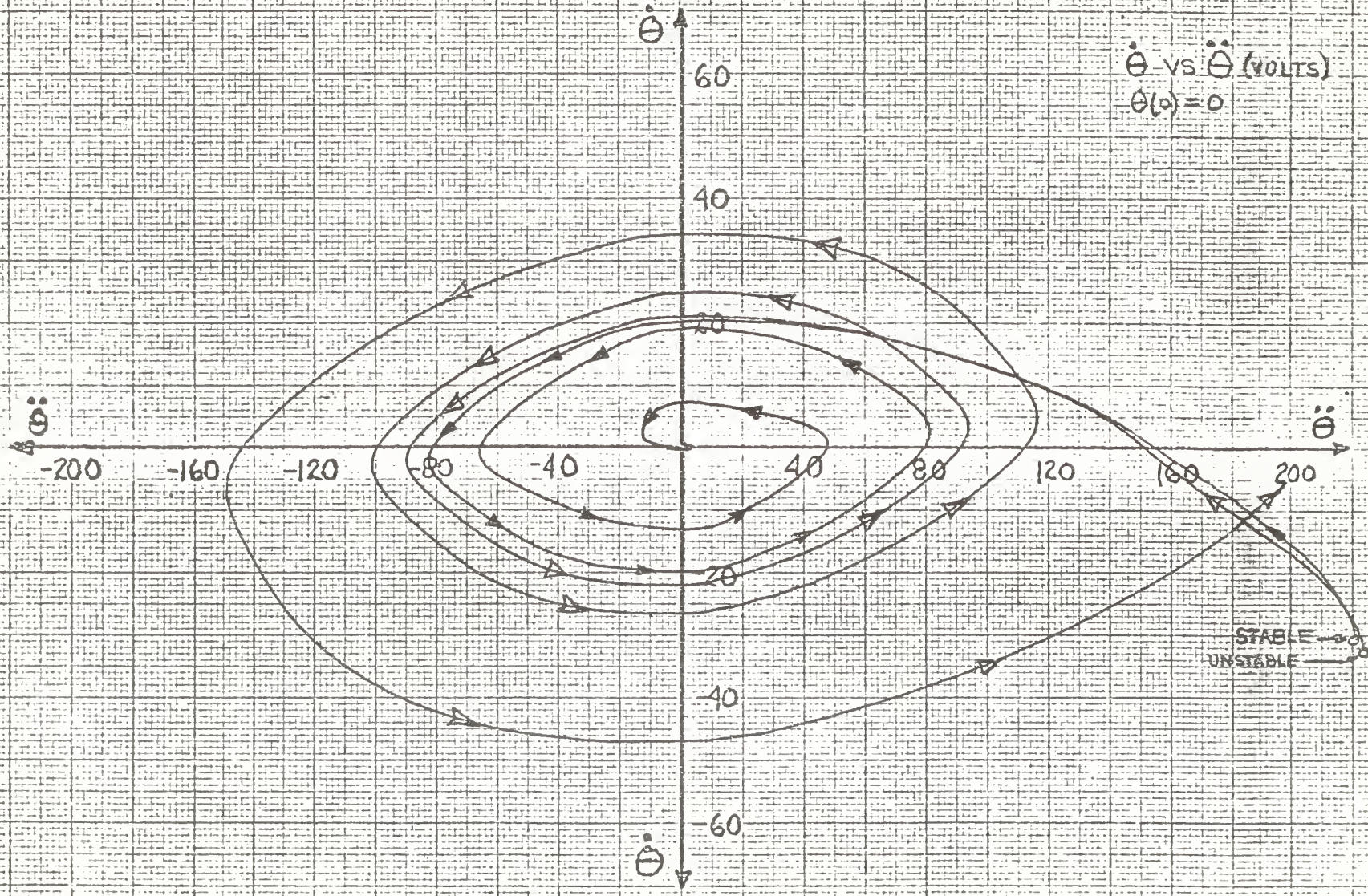

Figure III-6g. $\dot{\theta}$ vs $\ddot{\theta}$ trajectories.

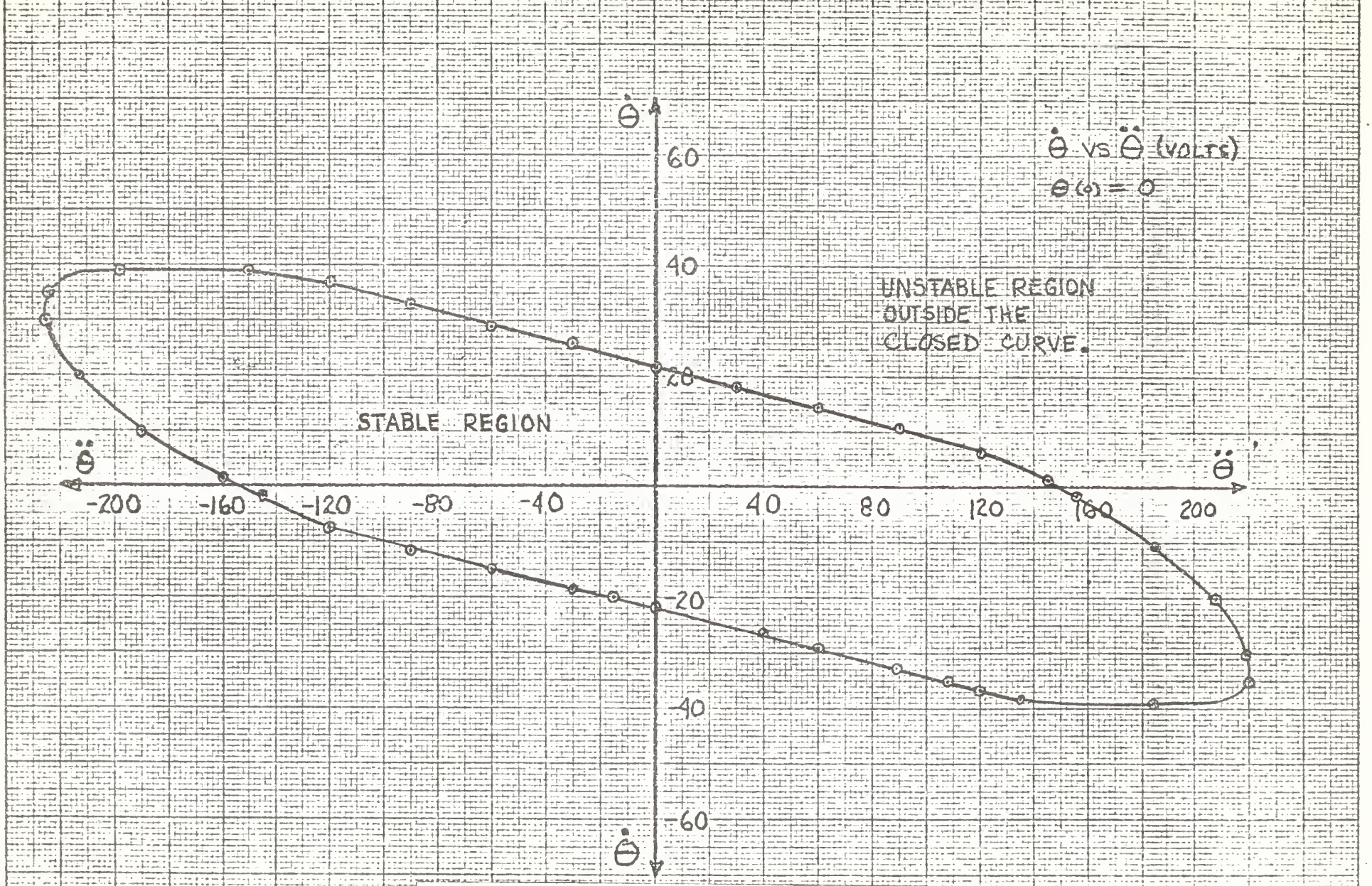

FIGURE III-7

$\dot{\theta}$ vs $\ddot{\theta}$ experimental stability limits.

Figure III-7 confirms the idea that stability depends on the signs of the initial conditions as well as the magnitudes. When the locus of stable runs is plotted on the $B_1 - B_2$ plane, as in Figure III-8, two principal dividing lines result. The first, shown as a dashed line, is for initial conditions of $\dot{\theta}$ and $\ddot{\theta}$ of opposite signs. The second dividing line results from $\dot{\theta}$ and $\ddot{\theta}$ intiial conditions of the same sign.

The qualitative prediction of M-point motion is confirmed, in part, when the runs of Fig. III-6e are plotted on the $B_1 - B_2$ plane, as in Fig. III-8. The unstable run is not predictable from the qualitative description of M-point motion.

Unless the $\dot{\theta}$ vs $\ddot{\theta}$ trajectory can be predicted, stability can not be predicted. To assist in predicting the $\dot{\theta}$ vs $\ddot{\theta}$ trajectory, isocline theory seems to be the only available method. The differential equation for this control system is rewritten as:

$$\dddot{\theta} + B_2\ddot{\theta} + B_1\dot{\theta} + 60\theta = 0. \qquad \text{(III-17)}$$

Since,

$$\frac{d\ddot{\theta}}{dt} = \dddot{\theta} \qquad \text{(III-18)}$$

and,

$$\frac{d\dot{\theta}}{dt} = \ddot{\theta} \qquad \text{(III-19)}$$

then substituting Eqs. (III-18 and 19) in Eq. (III-17) and rearranging gives:

$$\frac{d\ddot{\theta}}{dt} = -B_2\ddot{\theta} - B_1\dot{\theta} - 60\theta. \qquad \text{(III-20)}$$

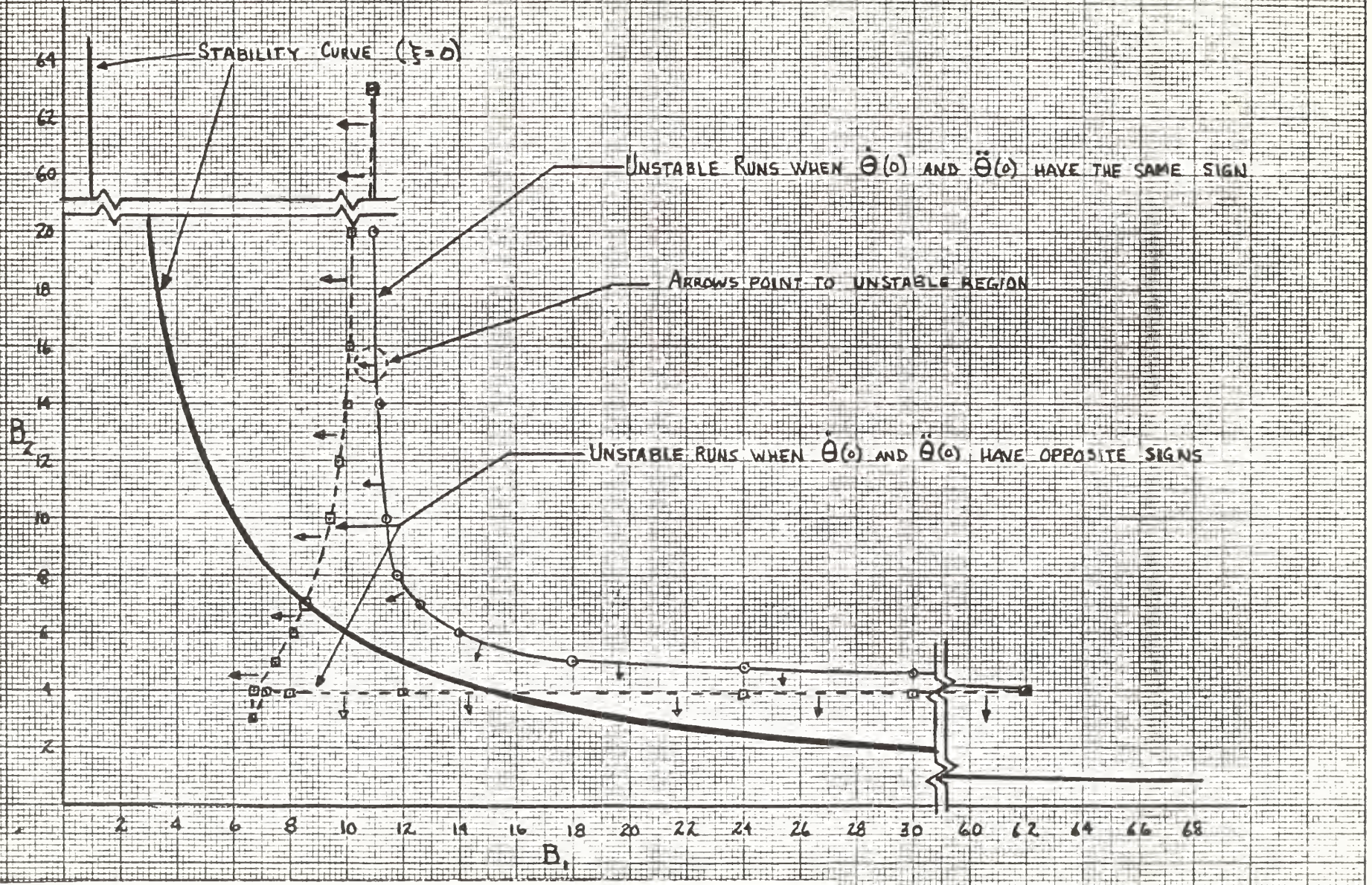

Figure III-8. Experimental stability limits on the B_1 - B_2 plane.

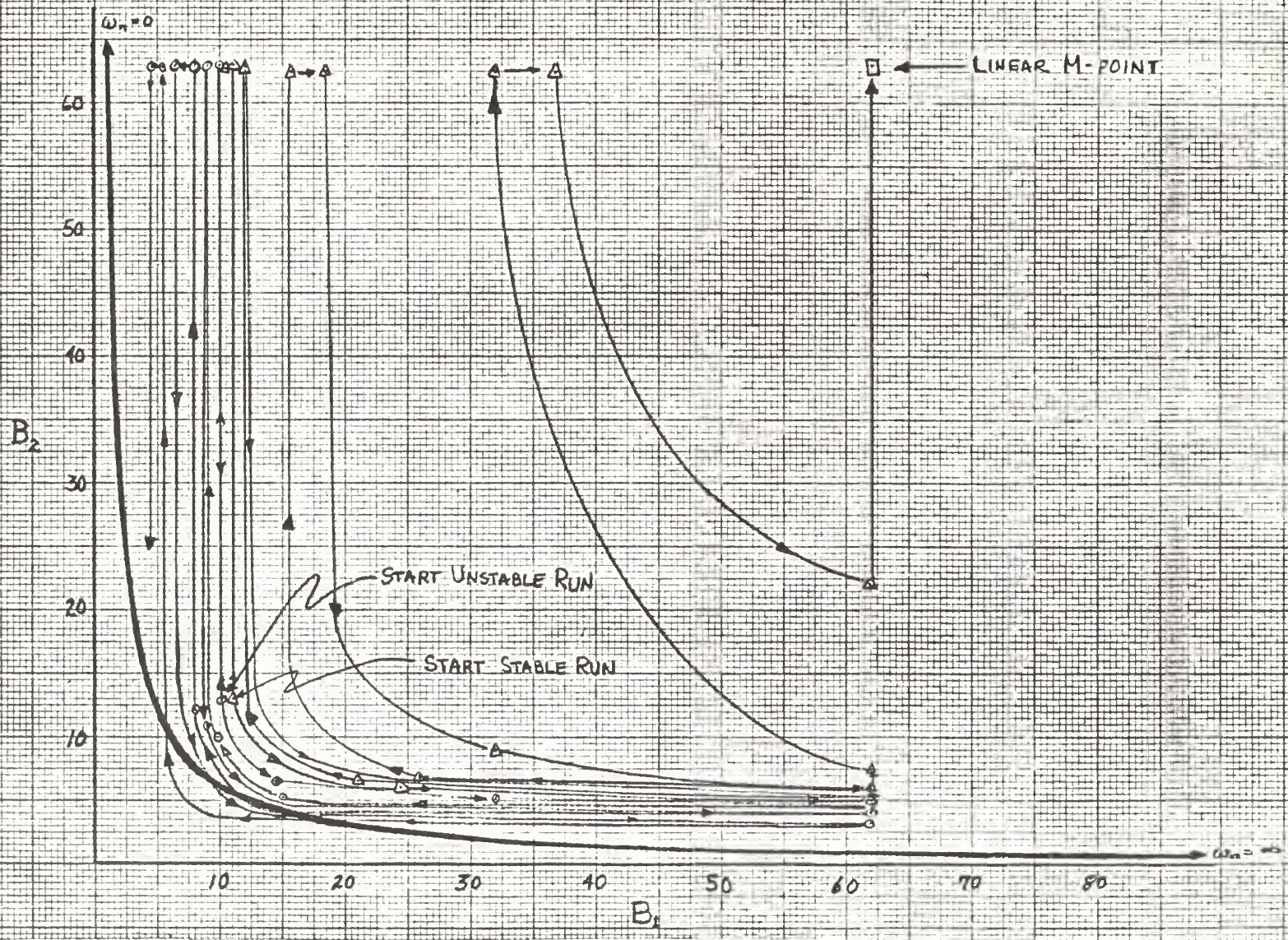

Figure III-9. Actual M-point motion on the B_1 - B_2 plane.

If the slope on the $\dot{\theta}$ vs $\ddot{\theta}$ phase plane is defined as N, then

$$N \triangleq \frac{d\ddot{\theta}}{d\dot{\theta}}. \qquad \text{(III-21)}$$

When the left side of Eq. (III-20) is divided by $d\dot{\theta}/dt$ and the right side by $\ddot{\theta}$, Eq. (III 22) results.

$$\frac{d\ddot{\theta}/dt}{d\dot{\theta}/dt} = -\frac{B_2\ddot{\theta} + B_1\dot{\theta} + 60\theta}{\ddot{\theta}}. \qquad \text{(III-22)}$$

Eliminating dt from the left side of Eq. (III-22) and replacing $d\ddot{\theta}/d\dot{\theta}$ by the slope, N, produces the desired equation for the isoclines in the $\dot{\theta}$ vs $\ddot{\theta}$ phase plane. When the non-linear factors, B_1 and B_2, are substituted in the isocline equation, it becomes:

$$N = \frac{-\left(3 + \frac{180}{|\ddot{\theta}|}\right)\ddot{\theta} - \left(2 + \frac{180}{|\dot{\theta}|}\right)\dot{\theta} - 60\theta}{\ddot{\theta}}. \qquad \text{(III-23)}$$

Equation III-23 may be rewritten as:

$$N = \frac{-3\ddot{\theta} - 2\dot{\theta} - 60\theta - 180\,\text{sign}\,\ddot{\theta} - 180\,\text{sign}\,\dot{\theta}}{\ddot{\theta}}. \qquad \text{(III-24)}$$

The only unknown, when Eq. (III-24) is applied to the $\dot{\theta}$ vs $\ddot{\theta}$ phase plane for given values of N, is θ. If some value of θ is assumed, the isoclines can be drawn. Figures III-10a through 10c show these isoclines for θ equal to zero, 10, and 20, respectively.

From Fig. III-7, it appears that, for a stable system, the maximum value of $\dot{\theta}$ when $\ddot{\theta}$ is zero is approximately 20 volts. By starting with $\dot{\theta}$ at -20 volts in Fig. III-10b, and tracing a trajectory away from that point in a reverse direction, a path results such that, for initial conditions anywhere on the path and for θ remaining at a value of +10 volts, the trajectory would return to the starting point. For a positive velocity and a positive displacement, the displacement can only increase. Thus,

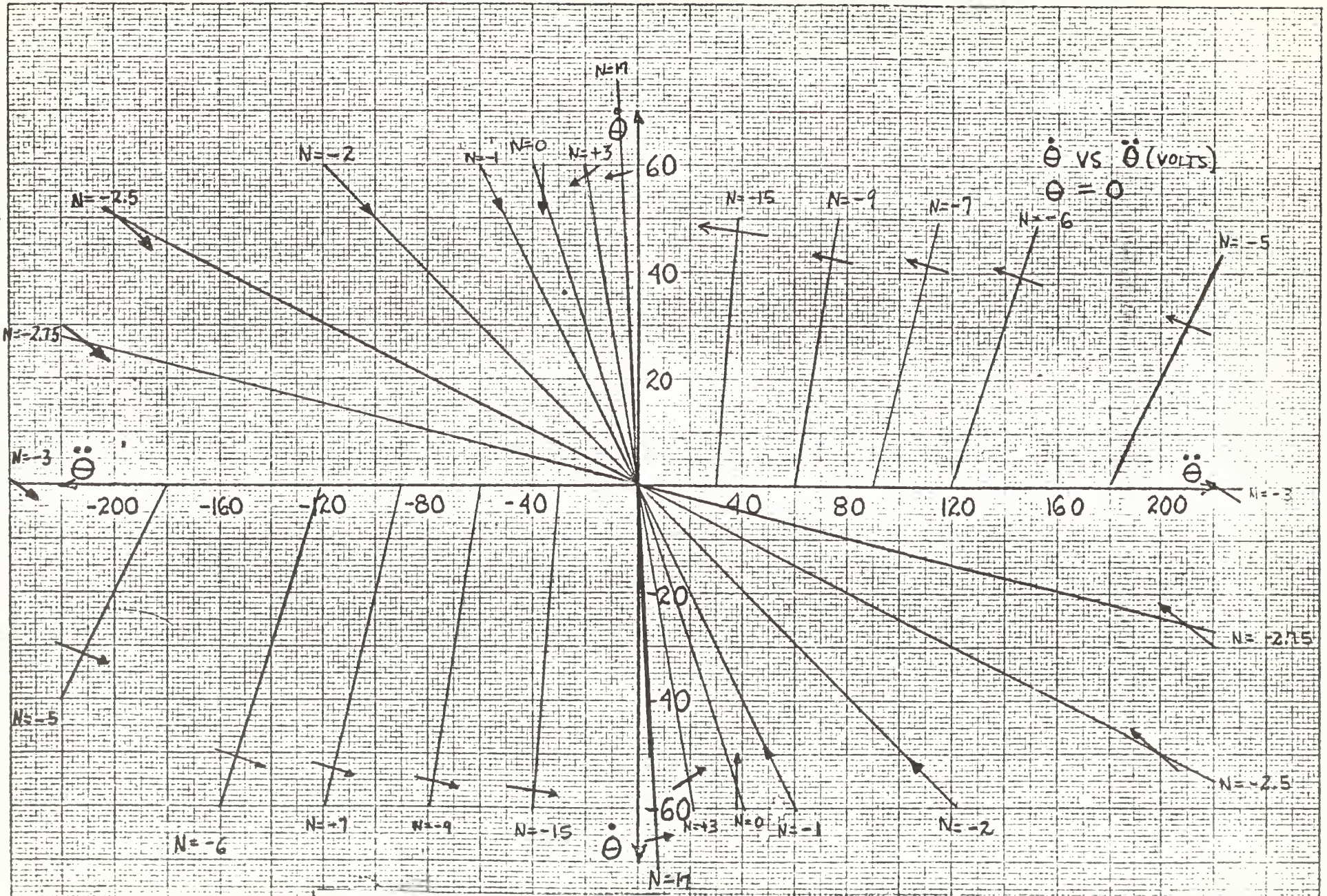

Figure III-10a. $\dot{\theta}$ vs $\ddot{\theta}$ isoclines for zero displacement.

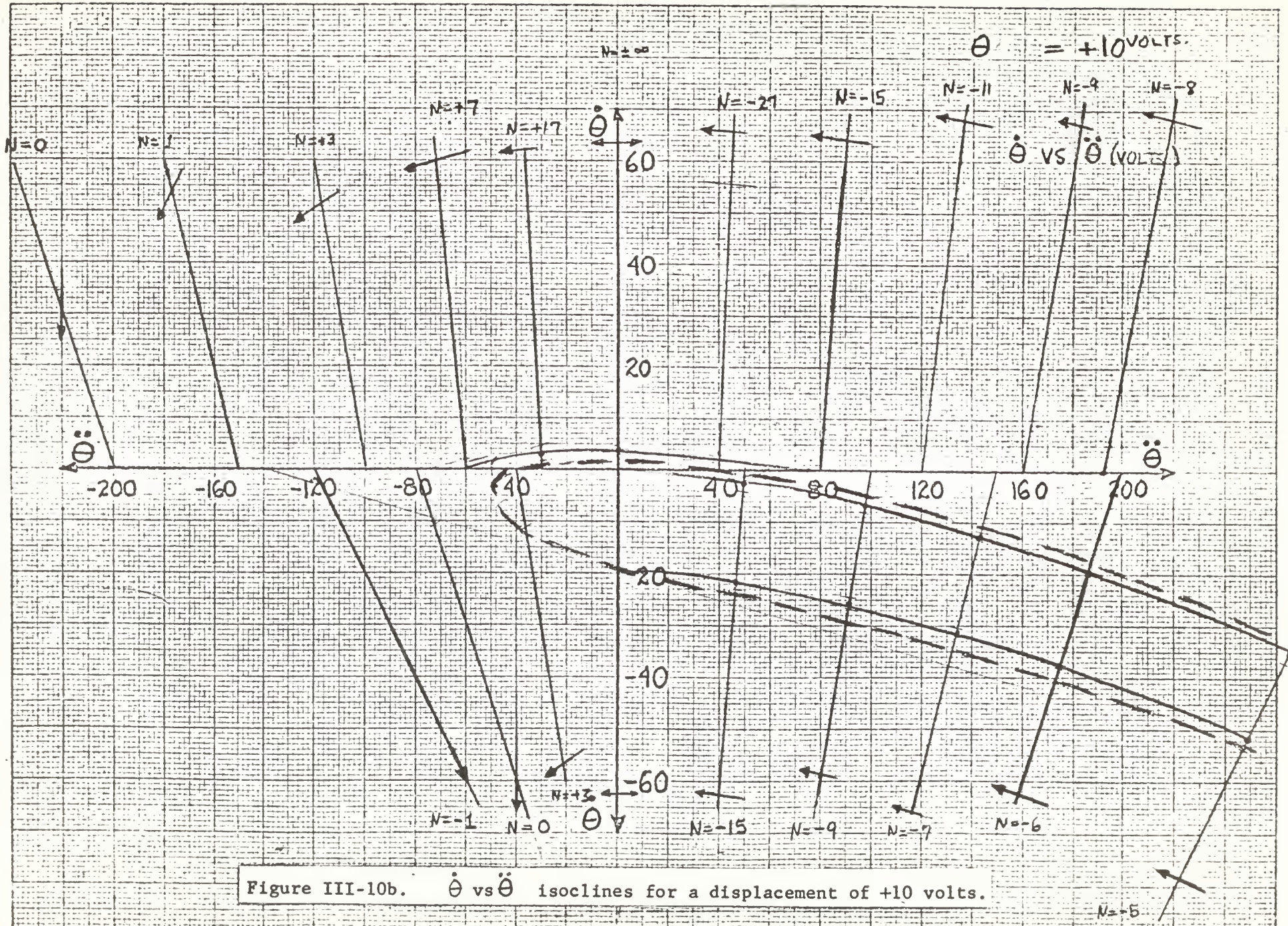

Figure III-10b. $\dot{\theta}$ vs $\ddot{\theta}$ isoclines for a displacement of +10 volts.

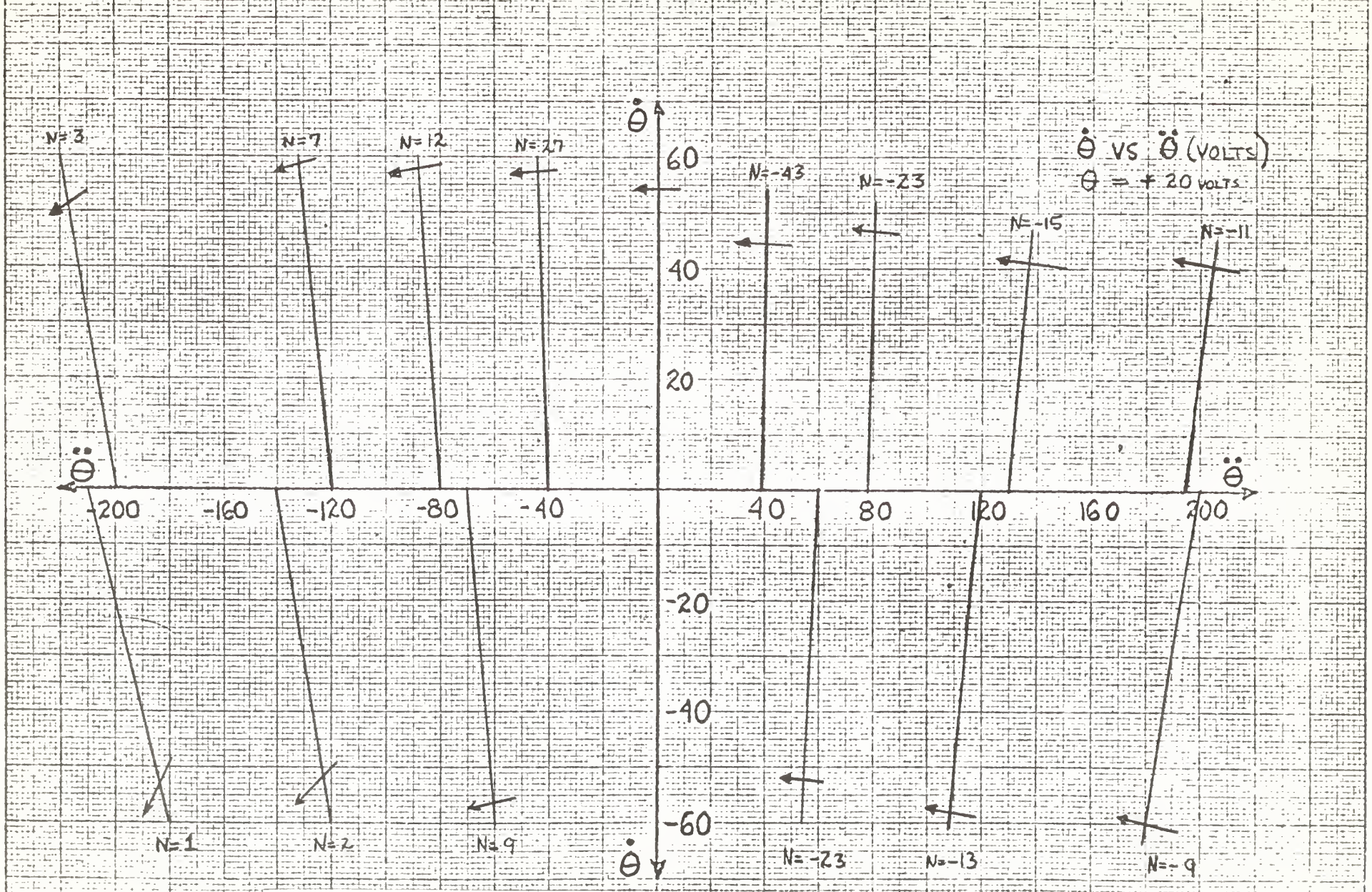

Figure III-10c. $\dot{\theta}$ vs $\ddot{\theta}$ isoclines for a displacement of +20 volts.

the predicted trajectory in the upper half of the $\dot{\theta}$ vs $\ddot{\theta}$ plane would tend toward one defined by the isoclines in Fig. III-10c. For $\dot{\theta}$ equal to zero, a second predicted trajectory to arrive at that point is drawn on Fig. III-10b. Using these two predicted trajectories, a region of stable runs is predicted on Fig. III-10b.

Once again, the $\dot{\theta}$ vs $\ddot{\theta}$ phase plane was searched for stable and unstable regions when $\theta(0)$ was ten volts. Figures III-11a through 11g are a sampling of the runs which were made in this search. When the locus of stable starting points is drawn, the region of stable runs is enclosed. Figure III-12 shows a portion of this region which corresponds closely with the region which was predicted.

According to the results plotted in Fig. III-12, when $\theta(0)$ is +10 volts no positive values of $\dot{\theta}$ are permitted if the system is to remain stable. Therefore, it is concluded that the system cannot remain stable for a step input greater than 10 volts by the reasoning which follows. Since the system is not critically damped, for a step input of 10 volts there will be some overshoot. As θ reaches 10 volts a positive velocity must exist to give overshoot. Therefore, the system will go unstable when θ is +10 volts and the velocity is positive.

Figure III-13a is a phase portrait of the $\dot{\theta}$ vs θ plane showing the trajectory for a step input of 10.1 volts. For this input, the system remained stable. Figure III-13b shows a recorder trace for the indicated variables versus time. Figure III-14 is the phase portrait of the $\dot{\theta}$ vs θ phase plane when the input was increased to 10.2 volts. For the 10.2 volt input, the system became unstable. No limit cycle operation could be found by varying the input between 10.1 and 10.2 volts. When the input is made in smaller steps, i.e., less than ten volts, and the system has

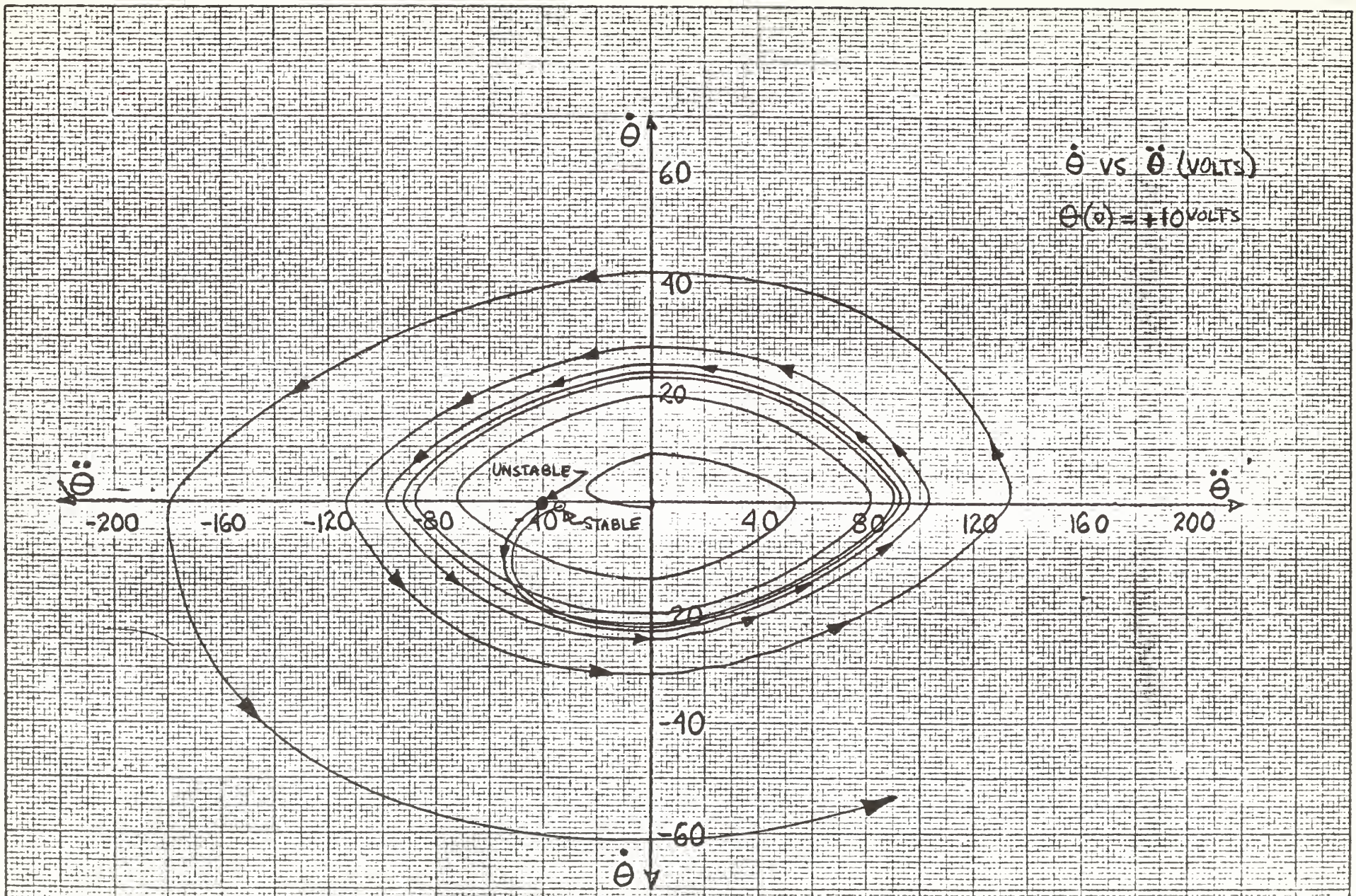

Figure III-11a. $\dot{\theta}$ vs $\ddot{\theta}$ trajectories.

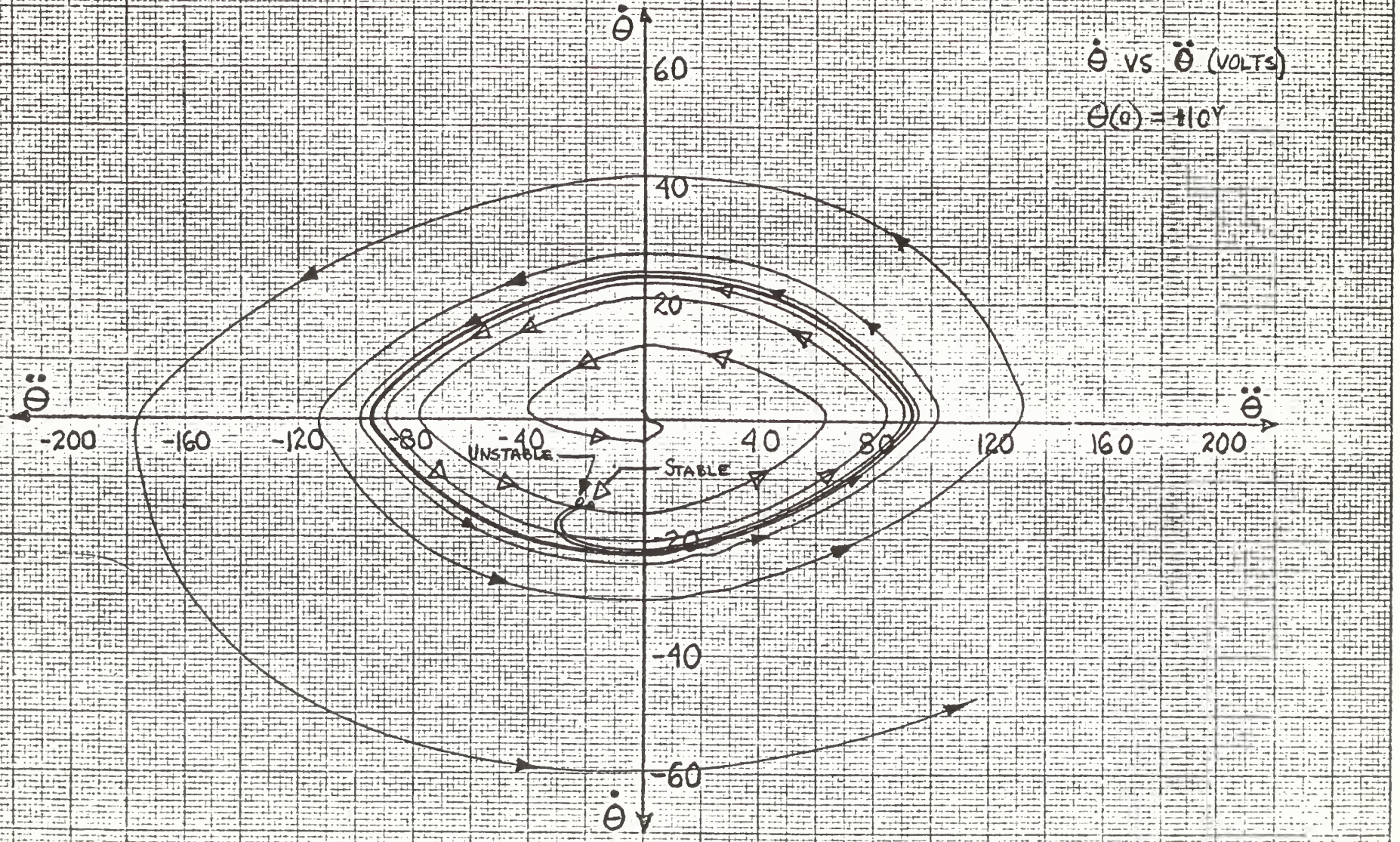

Figure III-11b. $\dot{\theta}$ vs $\ddot{\theta}$ trajectories.

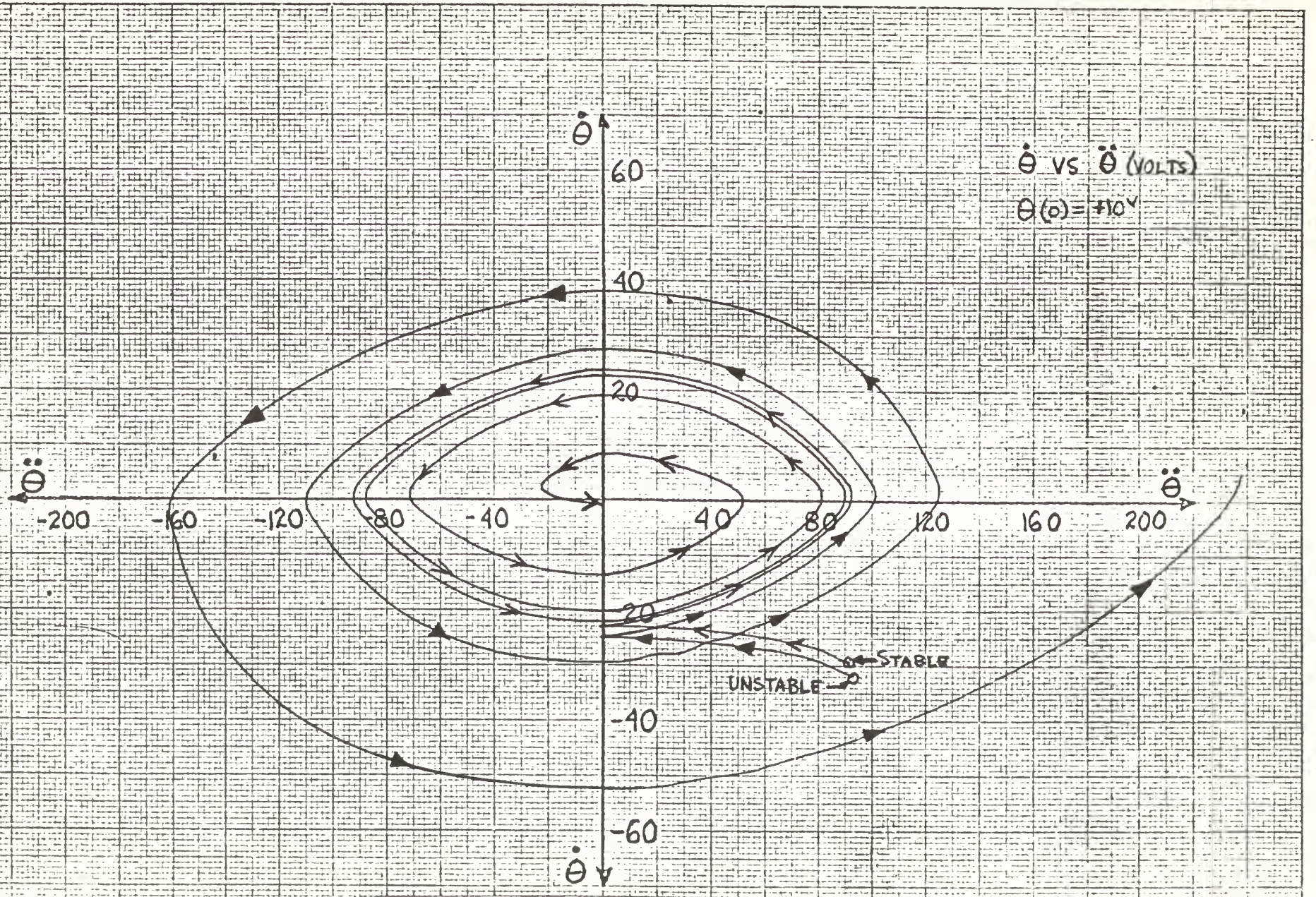

Figure III-11c. $\dot{\theta}$ vs $\ddot{\theta}$ trajectories.

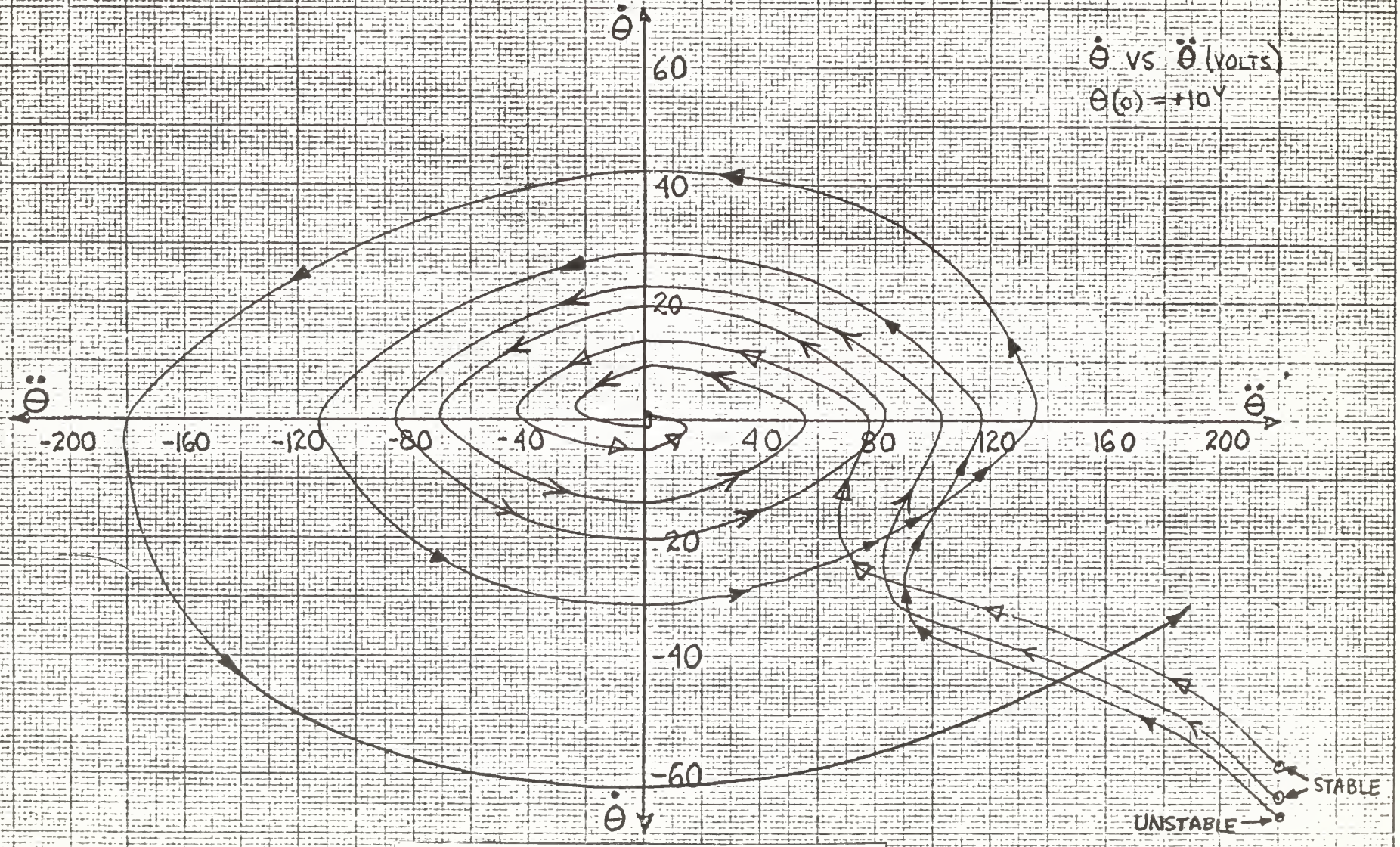

Figure III-11d. $\dot{\theta}$ vs. $\ddot{\theta}$ trajectories.

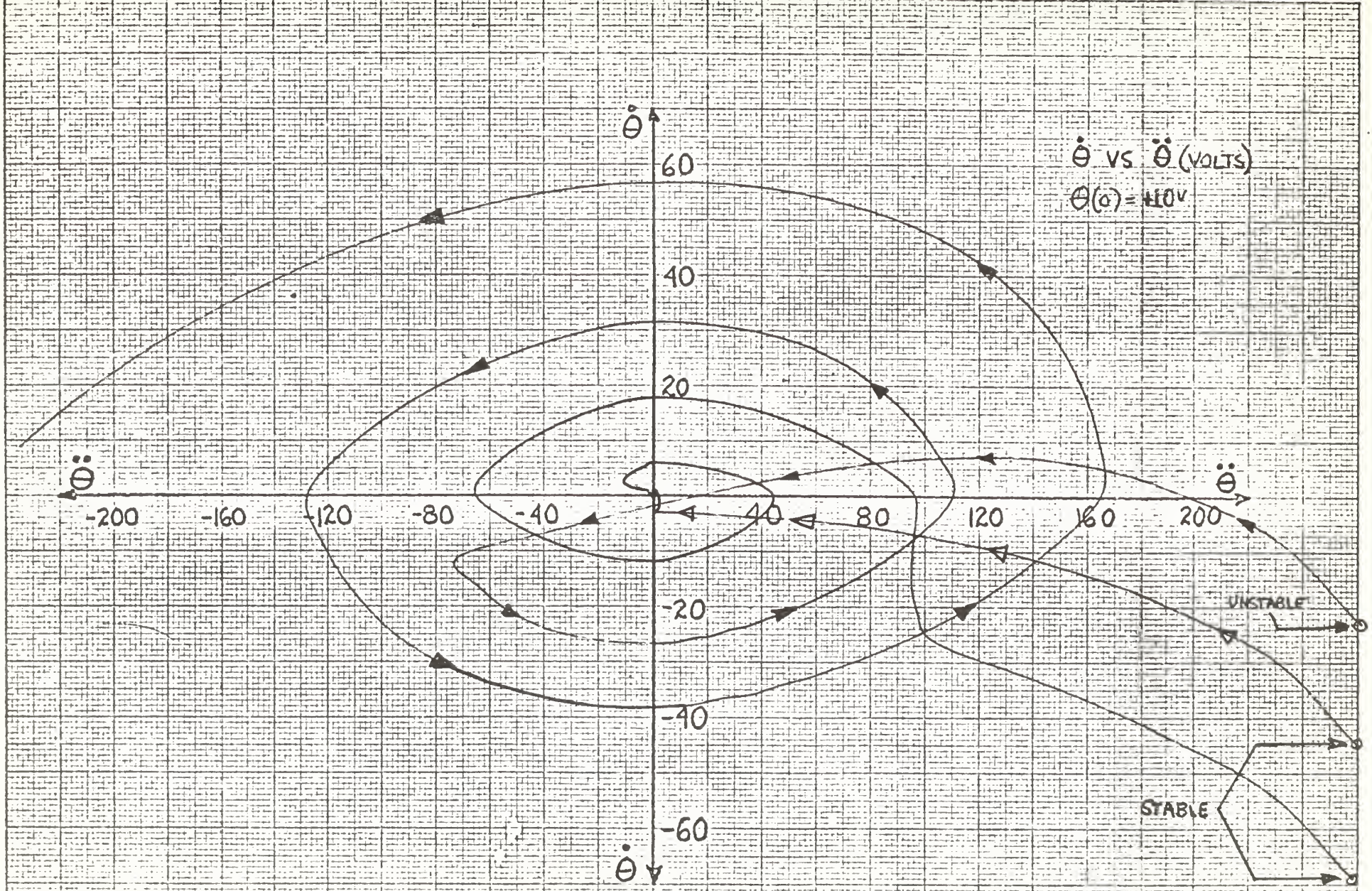

Figure III-11e. $\dot{\theta}$ vs $\ddot{\theta}$ trajectories.

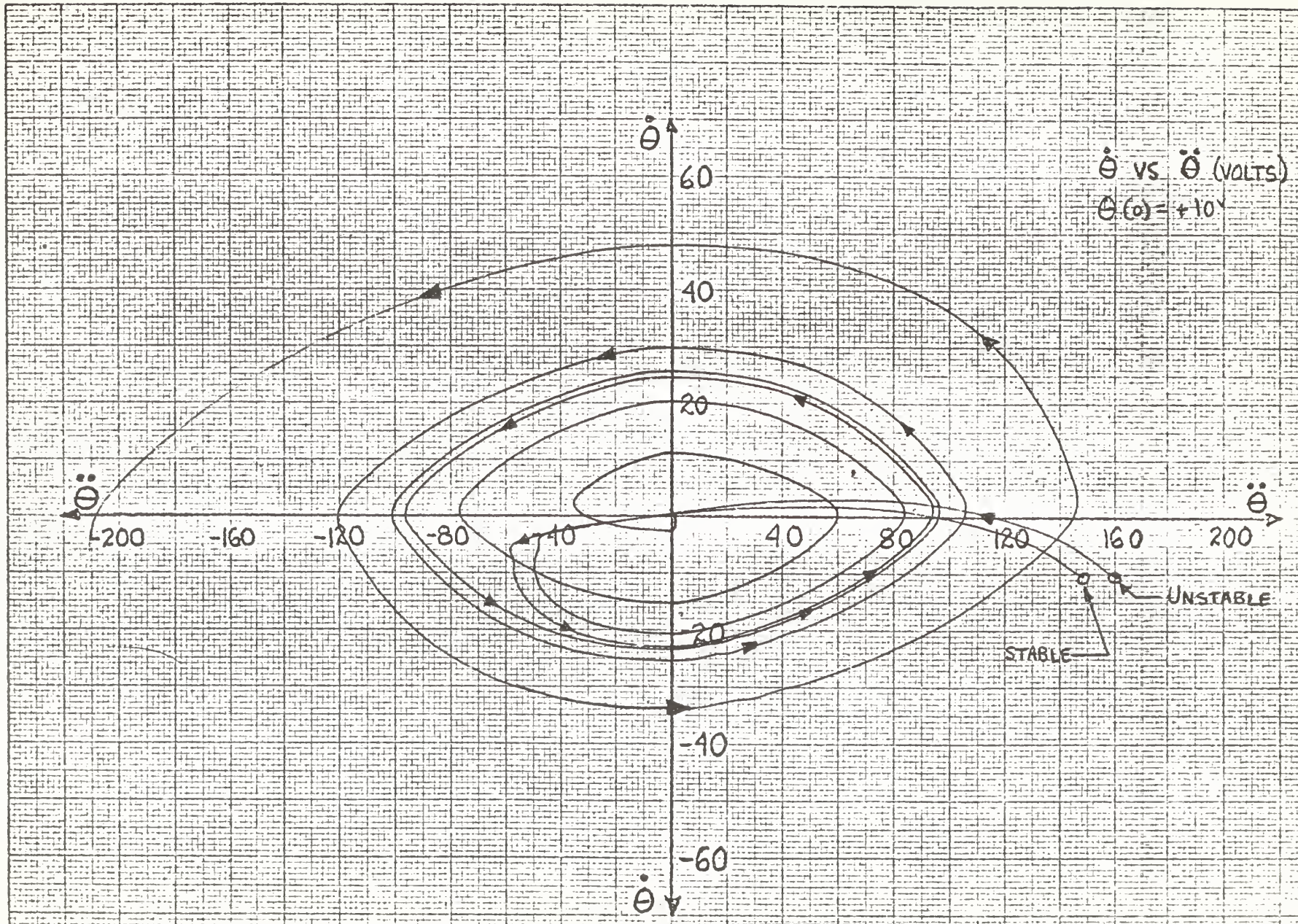

Figure III-11f. $\dot{\theta}$ vs $\ddot{\theta}$ trajectories.

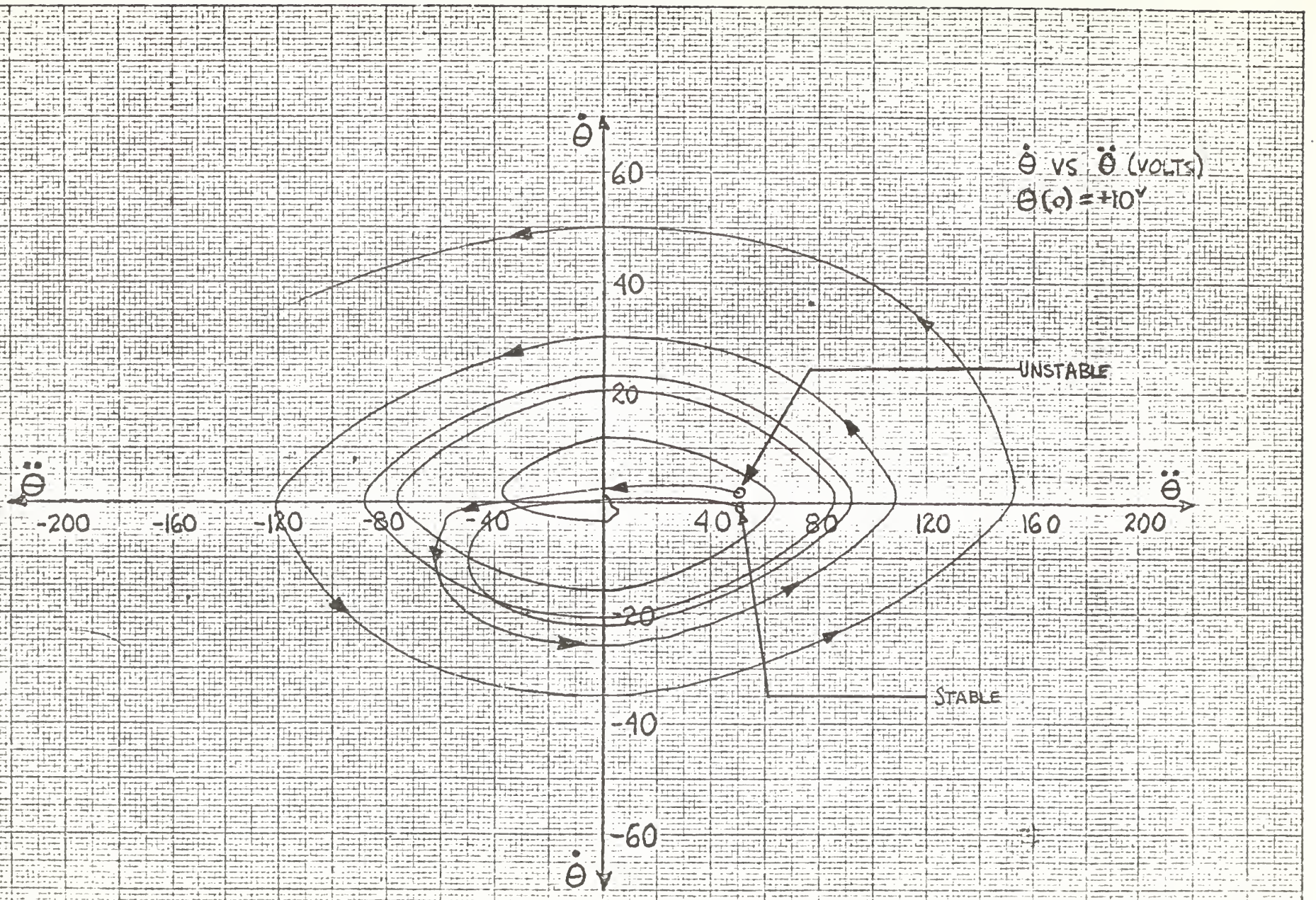

Figure III-11g. $\dot{\theta}$ vs $\ddot{\theta}$ trajectories.

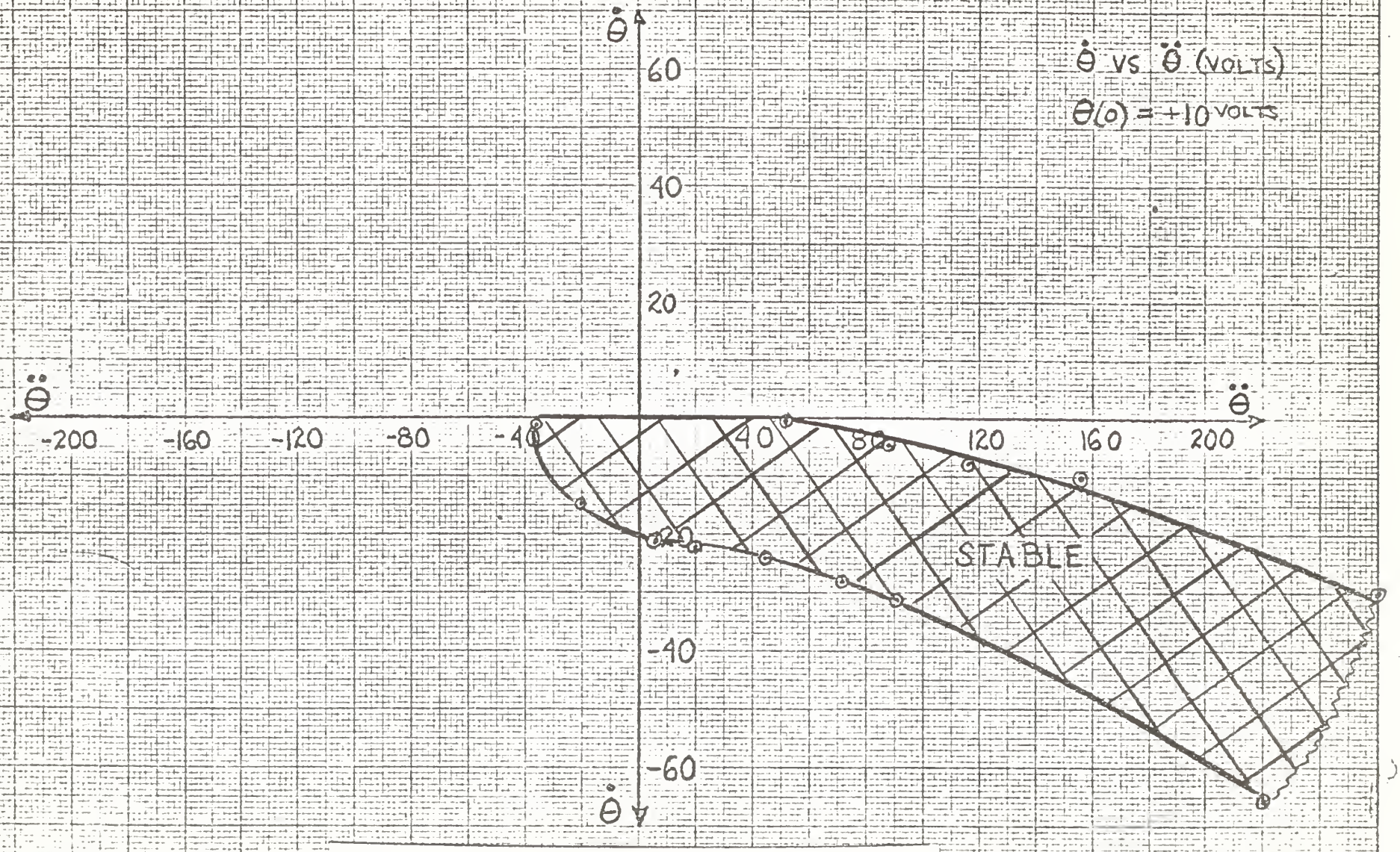

Figure III-12. $\dot{\theta}$ vs $\ddot{\theta}$ experimental stable region.

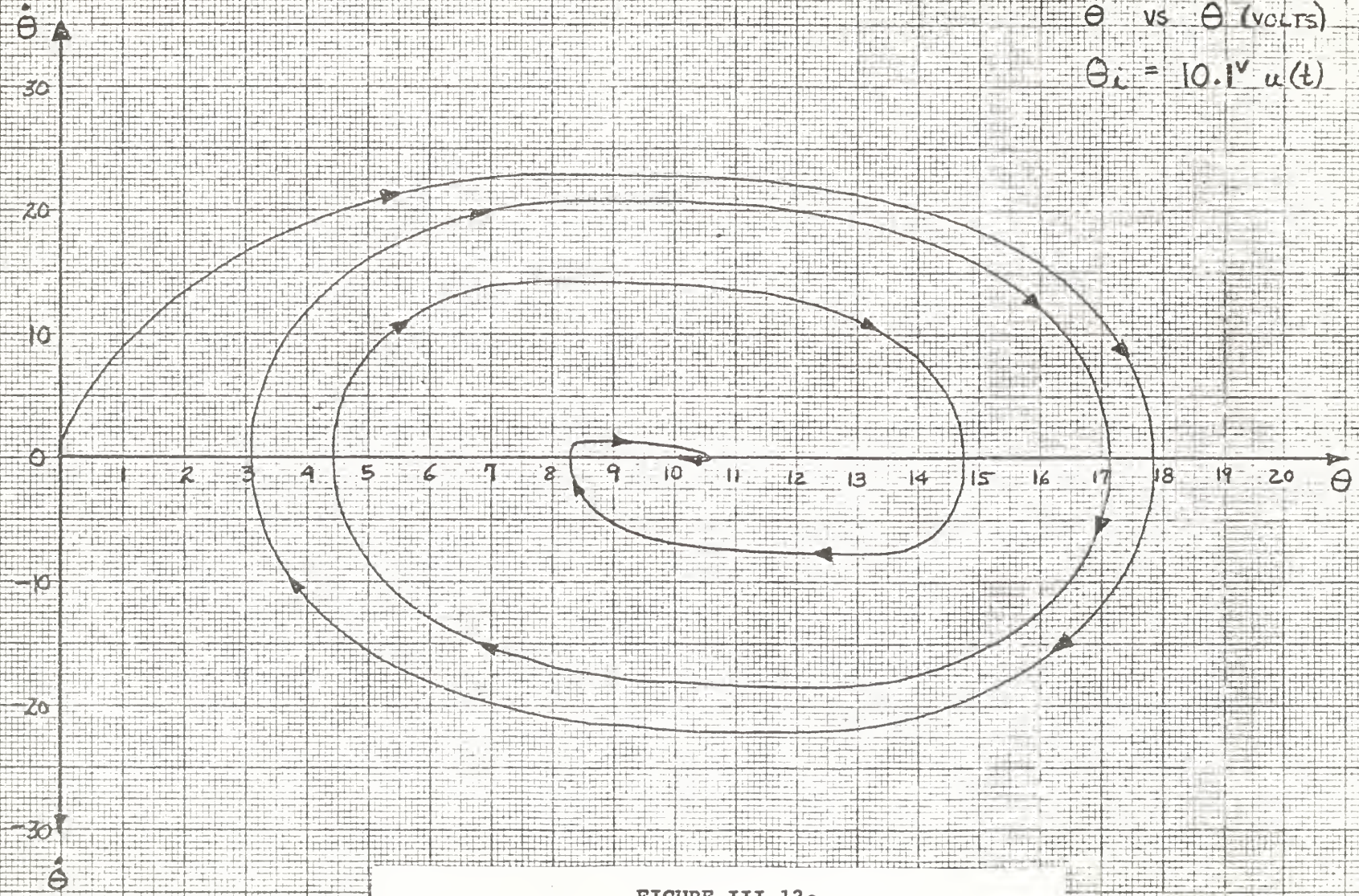

FIGURE III-13a

$\dot{\theta}$ vsθ trajectory for a step input of 10.1 volts.

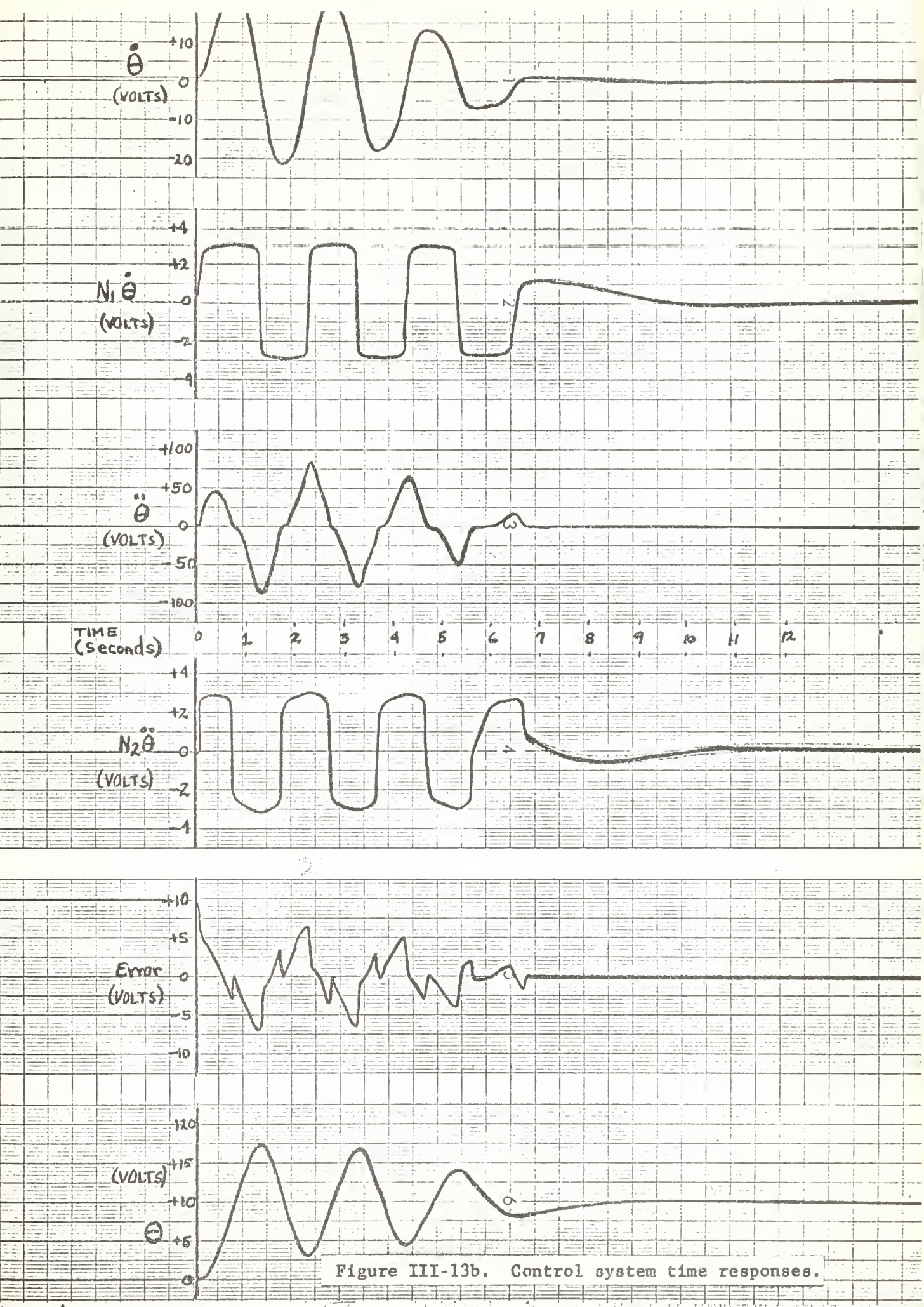

Figure III-13b. Control system time responses.

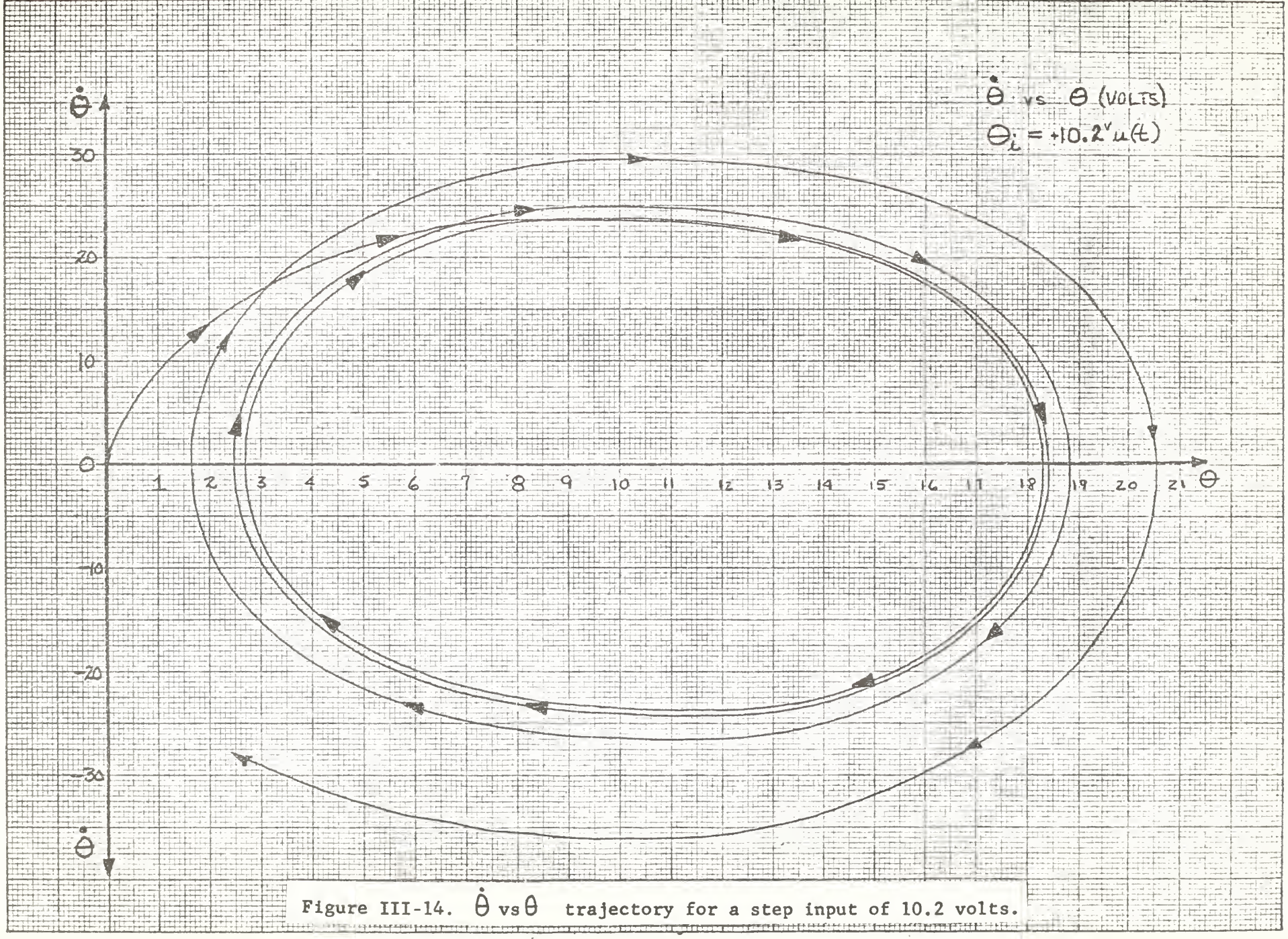

Figure III-14. $\dot{\theta}$ vs θ trajectory for a step input of 10.2 volts.

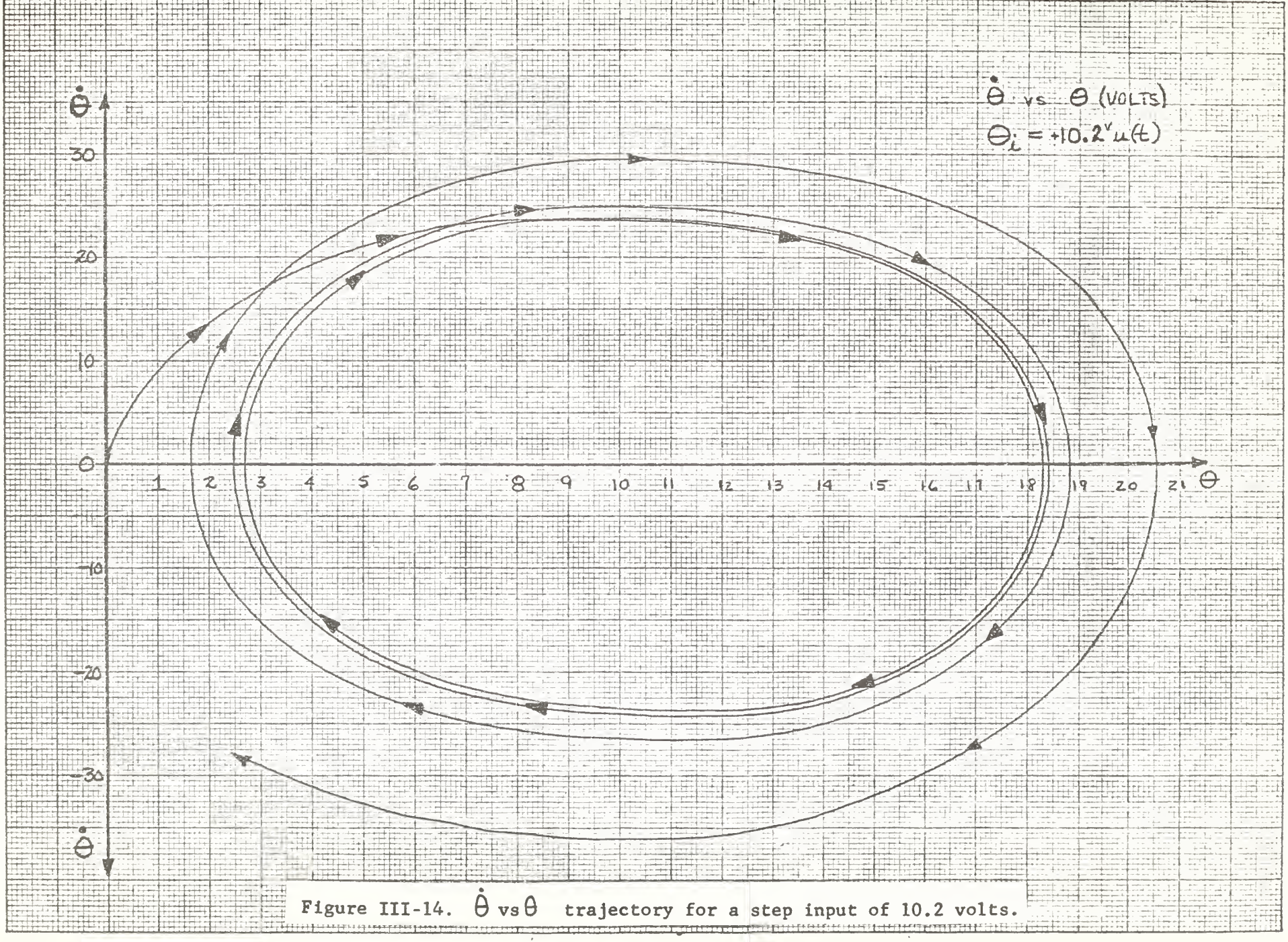

Figure III-14. $\dot{\theta}$ vs θ trajectory for a step input of 10.2 volts.

time to reach steady state between each successive step input the output will follow to any magnitude desired.

In the case of the tests described above, the $\dot{\theta}$ vs $\ddot{\theta}$ phase plane solutions for other stable regions when $\theta(0)$ was equal to π, 2π, 3π, and 4π units. Figures III-15a through 15d show the results of this study. It is concluded that, given any value of $\theta(0)$, a stable region can be found in the $\dot{\theta}$ vs $\ddot{\theta}$ phase plane. If a straight line were drawn through the approximate center of each such stable region, a relationship between $\ddot{\theta}(0)$ and $\dot{\theta}(0)$ which result in stable motion only can be stated as:

$$\ddot{\theta}_{(0)} = -5\dot{\theta}_{(0)},$$

where points are plotted for the limits of $\dot{\theta}(0)$ and a similar relationship between $\dot{\theta}(0)$ and θ [illegible]. This relationship is

$$\dot{\theta}_{(0)} = -5\theta_{(0)},$$

[illegible] are empirically derived and cannot be explained [illegible] theory, any of the preceding formulae, or the [illegible] method.

[illegible] existed for this system, it would have the shape [illegible] which was obtained from the near [illegible] run of Figure III-11b. When this limit cycle [illegible] $B_1 - B_2$ plane it produces a line shown as the limit [illegible] Figure III-17. Since a limit cycle implies a damping [illegible] ζ of 0, it appears that an effective value of ζ equal to [illegible] occurs at two places on the $B_1 - B_2$ plane - one at the limit [illegible] and one at the stability curve. When K_p and K_t

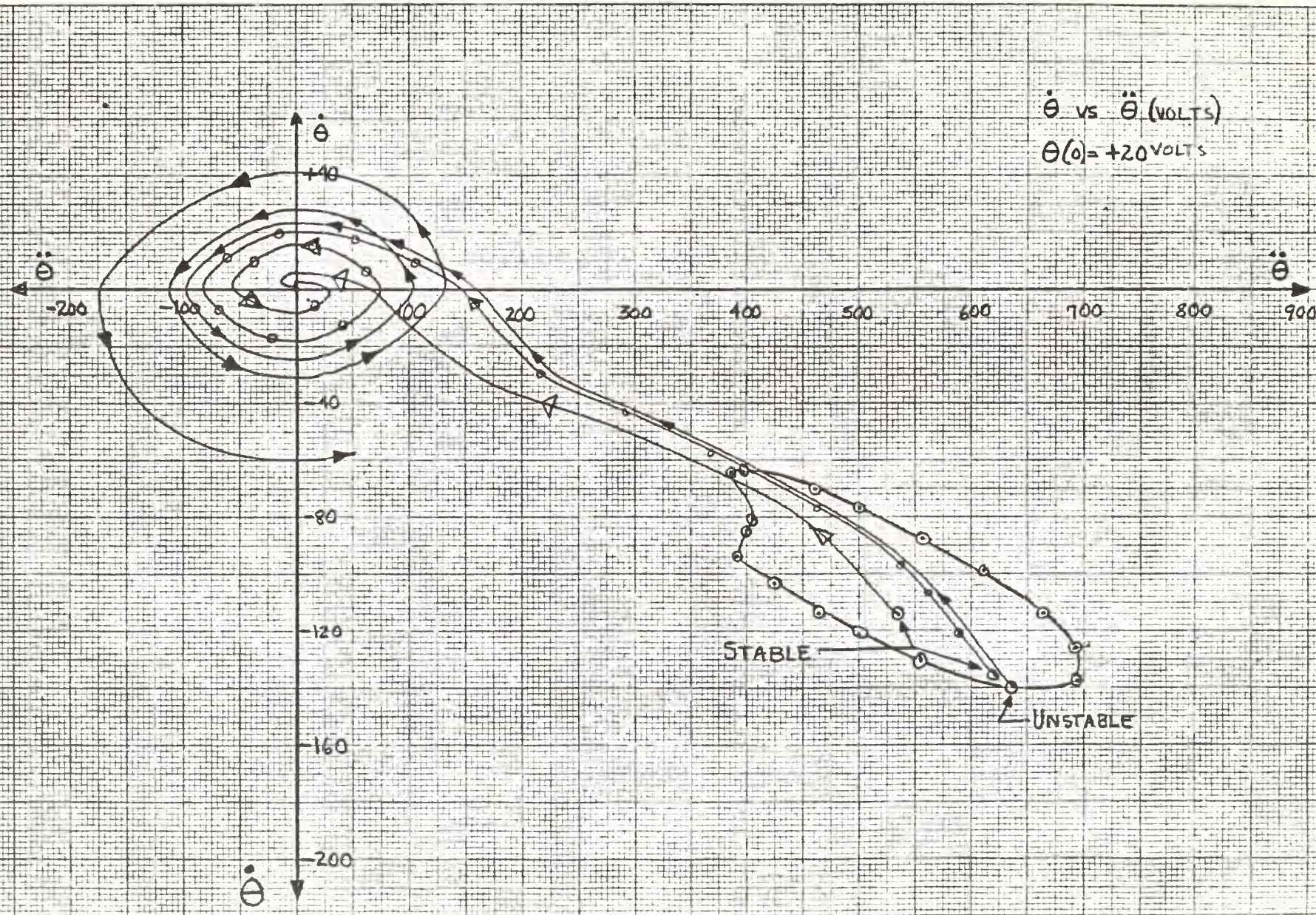

FIGURE III-15a

$\dot{\theta}$ vs $\ddot{\theta}$ trajectories and stability limits for an initial displacement of +20 volts.

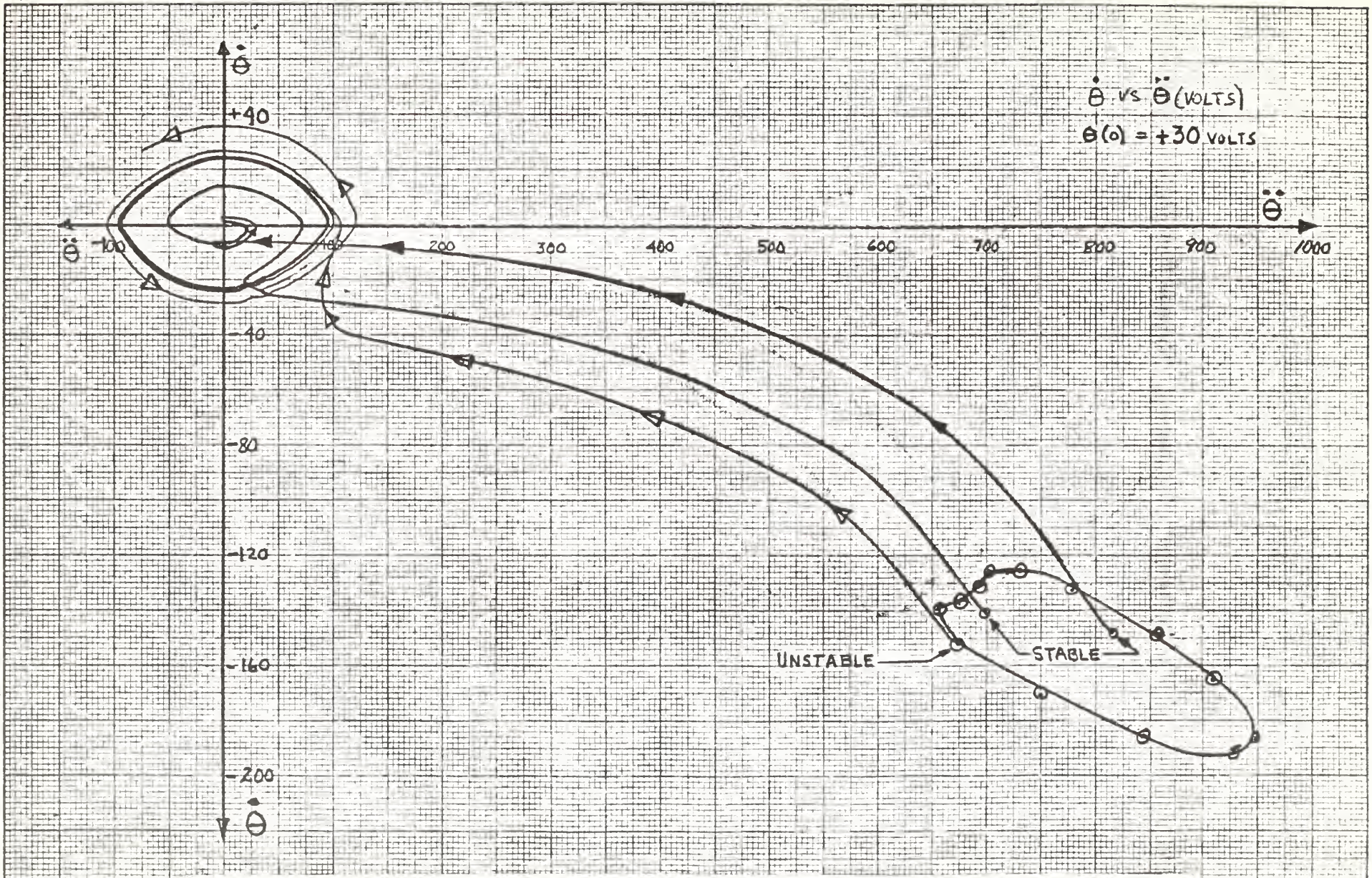

FIGURE III-15b

$\dot{\theta}$ vs $\ddot{\theta}$ trajectories and stability limits for an initial displacement of +30 volts.

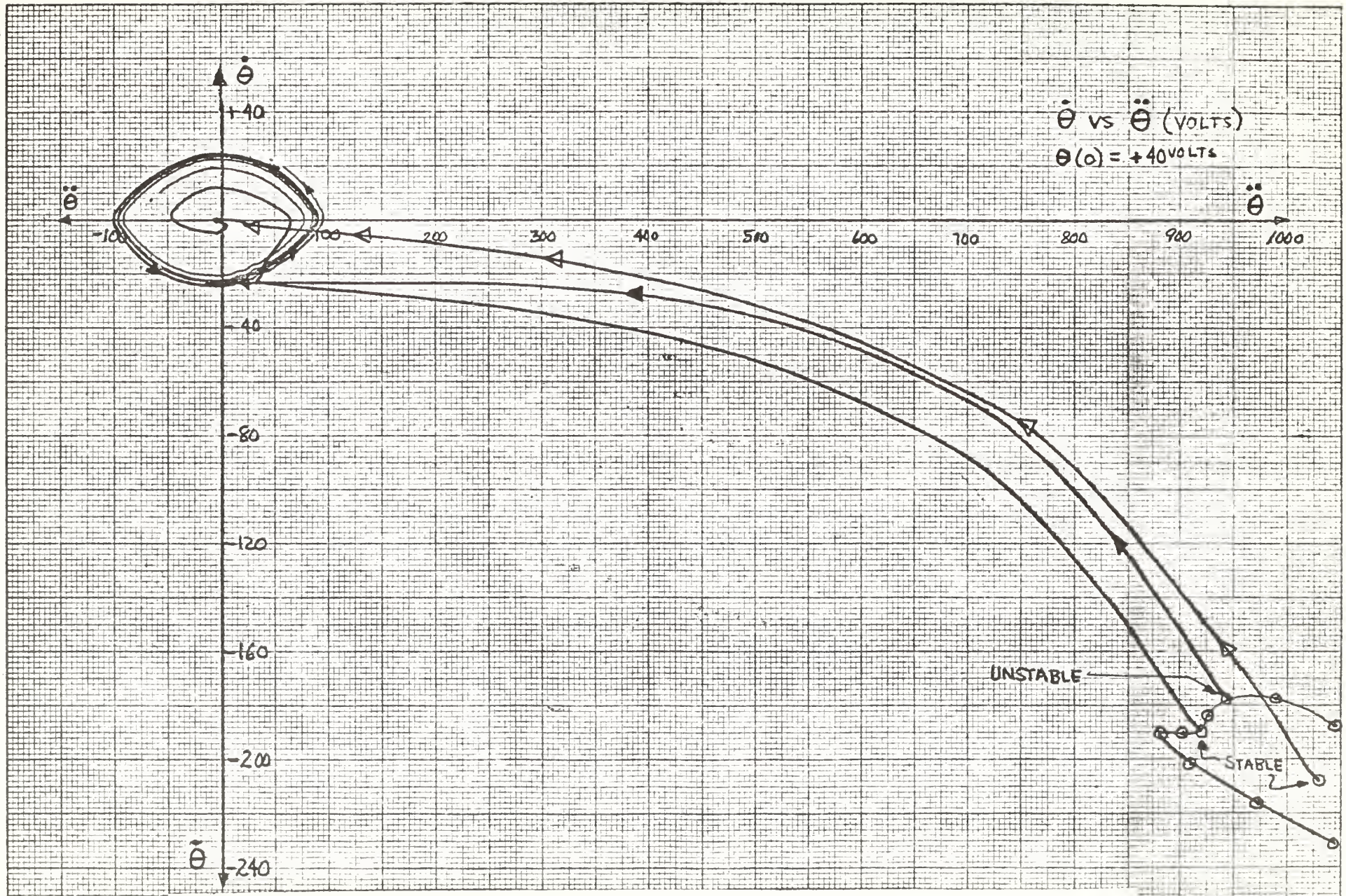

FIGURE III-15c

$\dot{\theta}$ vs $\ddot{\theta}$ trajectories and stability limits for an initial displacement of +40 volts.

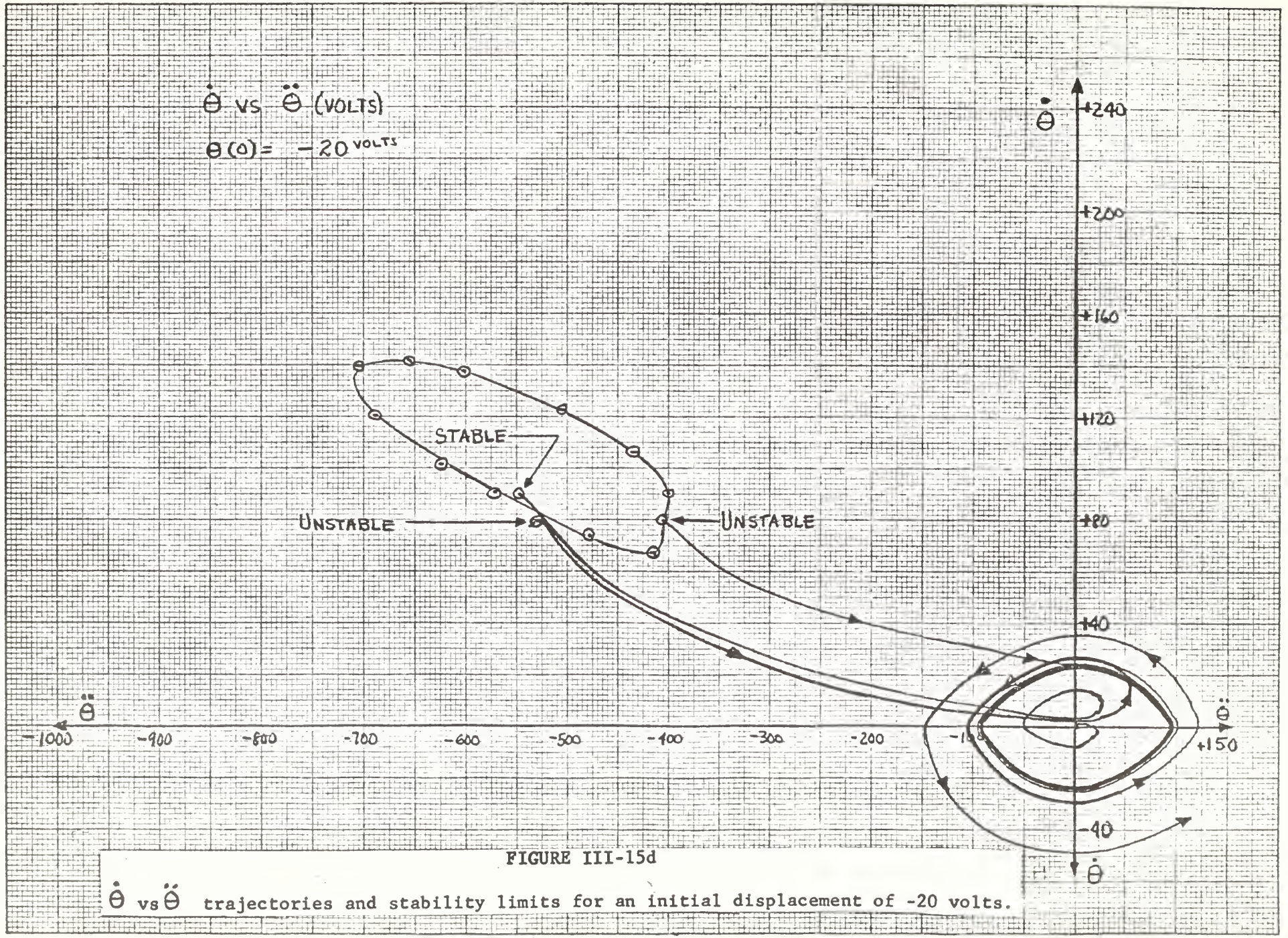

FIGURE III-15d

$\dot{\theta}$ vs $\ddot{\theta}$ trajectories and stability limits for an initial displacement of -20 volts.

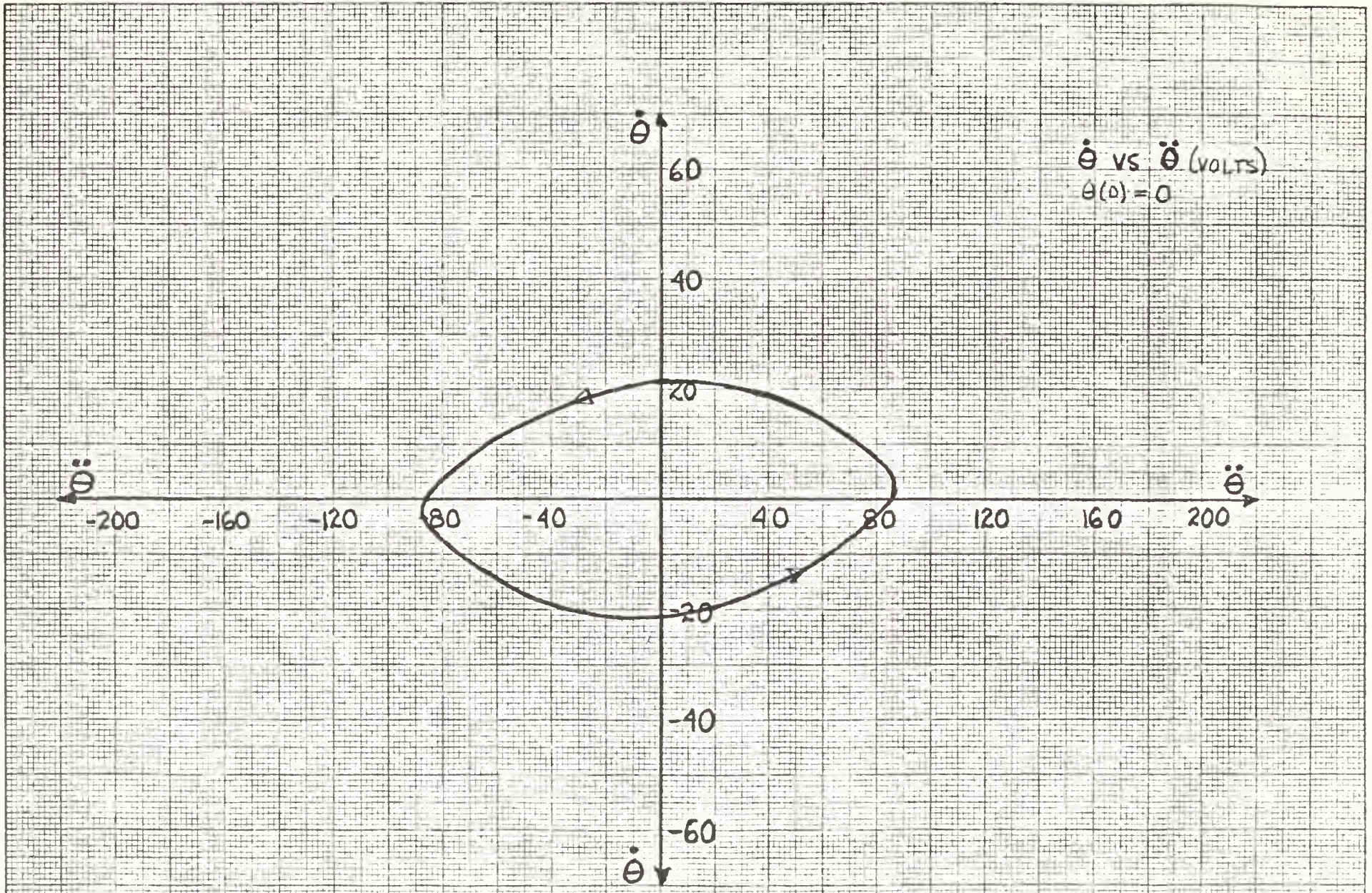

Figure III-16. Experimental unstable limit cycle locus on the $\dot{\theta}$ vs $\ddot{\theta}$ plane.

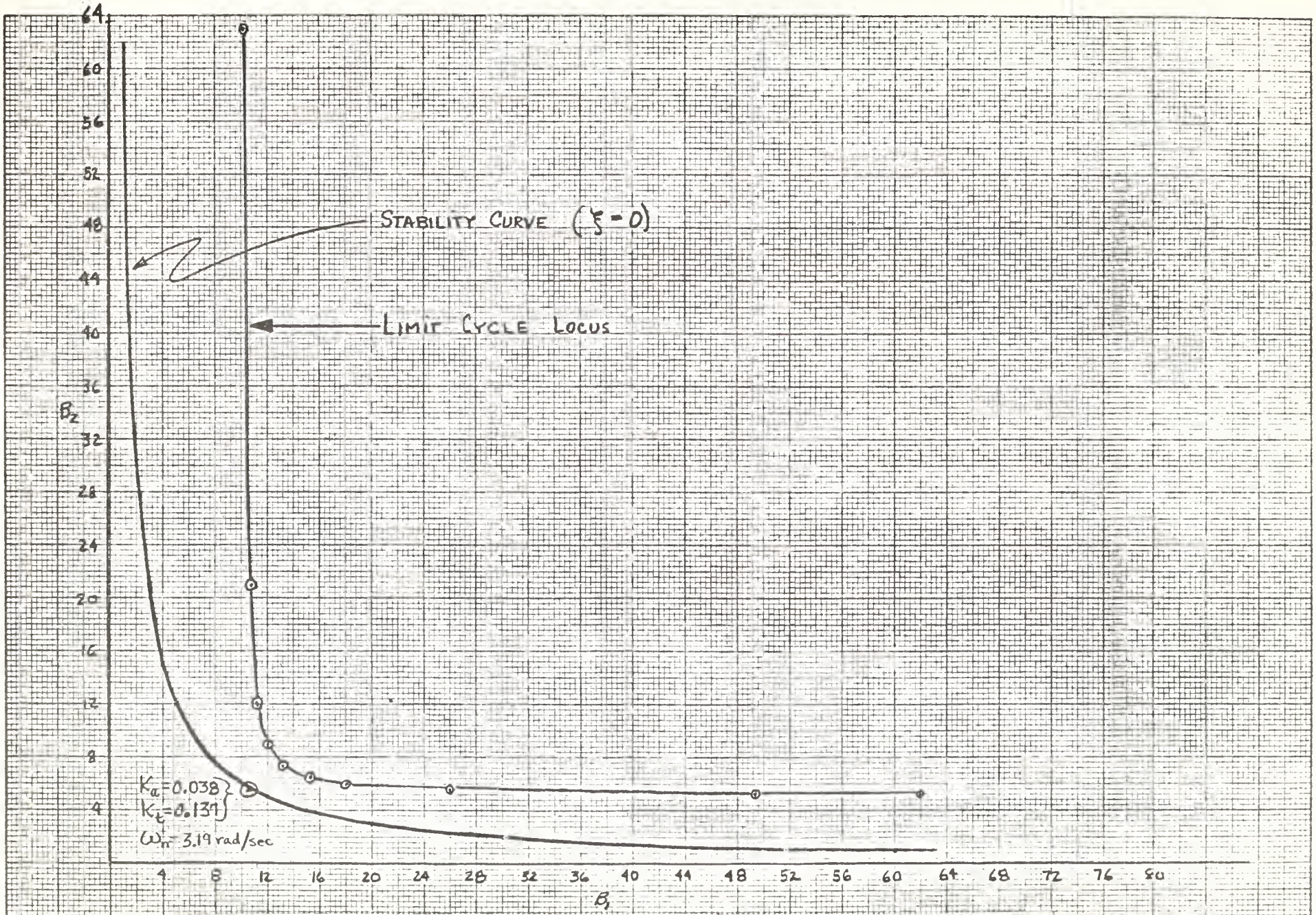

Figure III-17. Limit cycle locus and stability curve on the B_1 - B_2 plane.

are chosen to place the linear M-point on the stability curve, an unstable limit cycle results. An example of this type of run is shown in Fig. III-18 for the corresponding point from Fig. III-17.

Increasing the feedback gains K_a and K_t should widen the stable region of the $\dot{\theta}$ vs $\ddot{\theta}$ phase plane since the M-point would spend a longer period of time in the stable region of the $B_1 - B_2$ plane. Conversely, reducing the feedback gains should reduce the stable region. These two predictions were found to be true. Figure III-19 shows an unstable run results when K_t is reduced to 0.13 whereas, with $K_t = 1.0$, the starting point was in the stable region. Figure III-20 shows two stable runs when K_a and K_t are increased to 10. Both of these runs were unstable with unity feedback gains.

CONCLUSIONS.

It is concluded that an accurate prediction of system performance cannot be made using Mitrovic's method in conjunction with algebraic and graphical methods when two coefficients contain non-linear factors. From the investigations undertaken by this author, it appears that isocline theory by itself would provide the most accurate method of prediction. However, the use of isocline theory would require a large number of isocline plots, with accuracy being proportional to the number employed.

An analysis would proceed in the following manner, given the initial conditions at the starting point. Using the following relationship,

$$\Delta \ddot{\theta} = \frac{\dot{\theta}_2 - \dot{\theta}_1}{\Delta t}$$

and the values of $\ddot{\theta}$, $\dot{\theta}_2$, and $\dot{\theta}_1$ from a short trajectory, compute Δt. Then, from

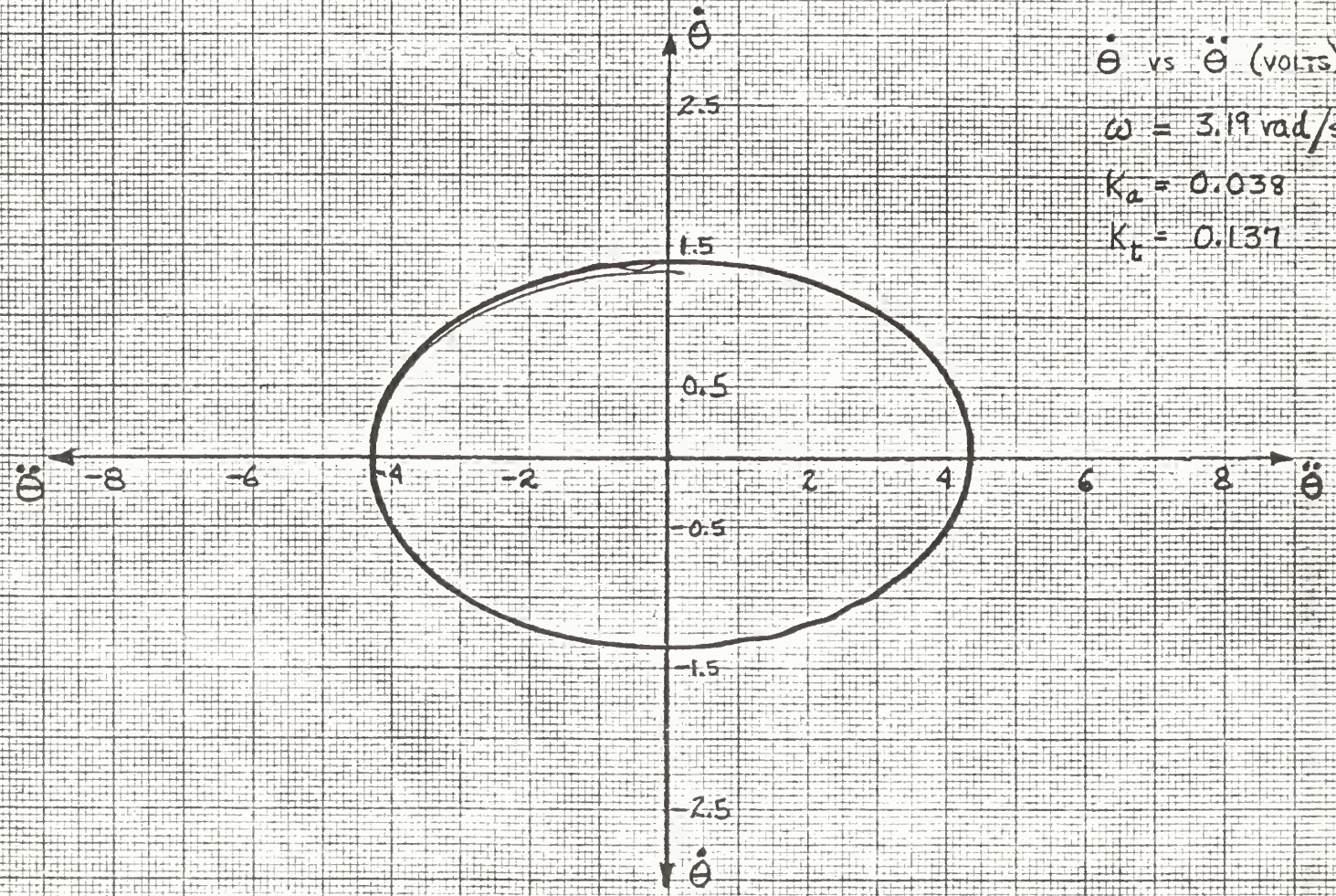

Figure III-18. Unstable limit cycle for reduced feedback gains.

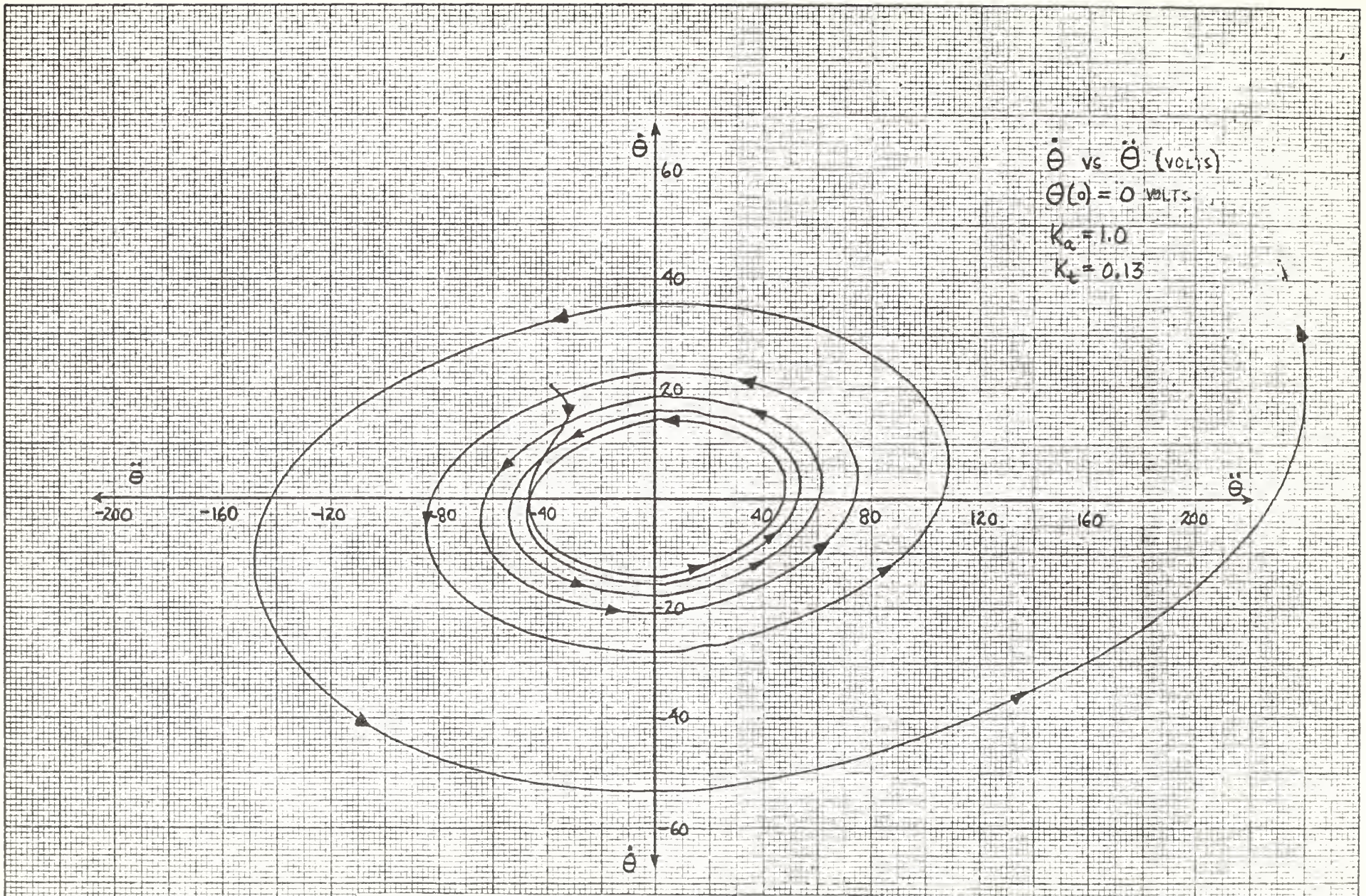

Figure III-19. $\dot{\theta}$ vs $\ddot{\theta}$ trajectory for reduced K_t.

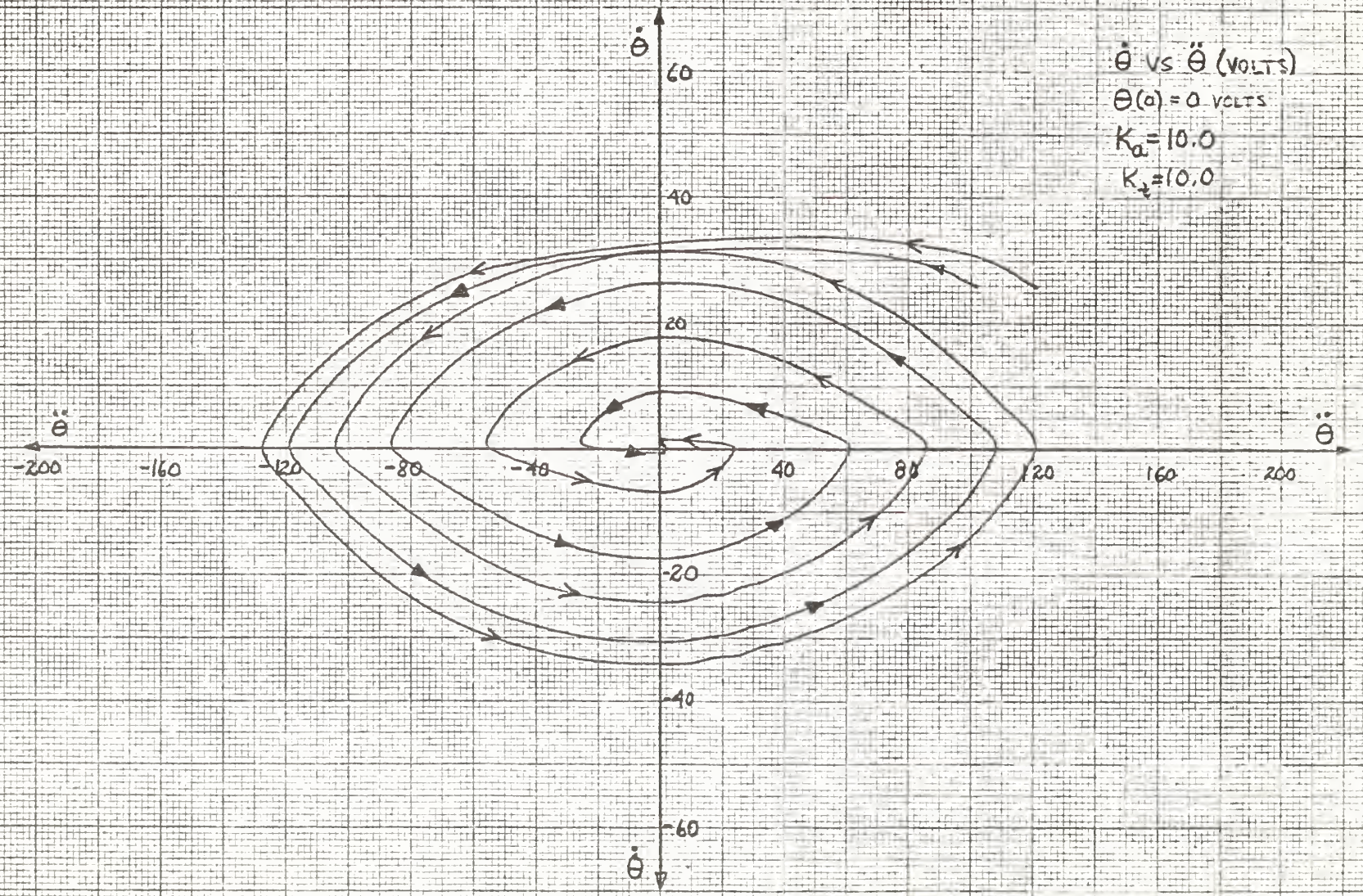

Figure III-20. $\dot{\theta}$ vs $\ddot{\theta}$ trajectories for increased feedback gains.

$$\Delta\theta = \Delta t \frac{\dot{\theta}_2 + \dot{\theta}_1}{2}$$

select a new isocline plot according to the new value of θ from a second short trajectory on the new isocline plot proceed as before. This process would be repeated until the trajectory either dies or becomes unstable. The isocline theory developed here would not be applicable to systems with characteristic equations of higher order than the third order equation for this system.

It is also concluded that the best means available to evaluate any system with two non-linearities is by analog or digital computer study. Unfortunately, computer methods can answer the question of what happens but not the more important question of why.

The dualism of the zeta equals zero line on the $P_1 - P_2$ plane is the single most disturbing and inexplicable phenomenon found in this study. If one such dualistic line exists it seems entirely possible that others might also be found. This factor alone would preclude the use of Mitrovic's method to predict system performance when two non-linearities are involved.

CHAPTER IV

MITROVIC'S METHOD APPLIED TO THE STABLE CONTROL SYSTEM

In Chapter III, the control system was studied to ascertain stability characteristics of the control system when the gain was high enough to cause the uncompensated system to be inherently unstable. By reducing the gain, the system can be made inherently stable. From Eq. (III-5), which is repeated here as Eq. (IV-1), the parametric equation for stability is:

$$B_1 B_2 = K, \tag{IV-1}$$

which may be rewritten as

$$(2 + KN_1K_t)(3 + KN_2K_a) = K. \tag{IV-2}$$

When K_a and K_t are zero, the maximum value which K may have for a stable system is six, which is found from Eq. (IV-2). The characterisitc equation for the system becomes

$$S^3 + B_1S^2 + B_2S + 6 = 0 \tag{IV-3}$$

The solution of Eq. (IV-3) with the appropriate B_1-B_2 Mitrovic equation pair from Appendix B gives the desired parametric equations for the B_1-B_2 plane:

$$B_1 = \omega_n^2 + \frac{6(2\zeta)}{\omega_n}$$

$$B_2 = \frac{6}{\omega_n^2} + (2\zeta)\omega_n \tag{IV-4}$$

The graphical solutions to Eqs. (IV-4) are shown in Fig. IV-1. Since B_1 cannot be less than two and B_2 cannot be less than three, the corresponding areas are ruled out in Fig. IV-1. Thus, the M-point must always be in the stable region and the control system is inherently stable. No dualism of the zeta equals zero line could be found by varying either initial conditions or the size of the step input.

It is desirable to predict an average M-point motion on the B_1-B_2 plane. If such a prediction were possible, system performance could be accurately described. Two approaches to the prediction problem were attempted. The first approach was a linear approximation to a step input response. The second approach was to analyze the results of many runs to ascertain if some definite "pattern" of performance could be determined.

LINEAR APPROXIMATION METHOD.

The procedure in this method was to choose a step input for the system and a starting M-point. It was assumed throughout that the system could be regarded as a second order system and, therefore, that the values of zeta and natural frequency, ω_n, would govern system performance.

The step input size was chosen as ten volts. Initial values of K_t = 2.57 and K_a = 0.6 were chosen to place the starting M-point at B_1 = 17.4 and B_2 = 6.6. At this point, the value of zeta is 0.4 and ω_n = 3.8 rad/sec.

If θ were sinusoidal then $\dot{\theta}$ would lag θ by 90 degrees and $\ddot{\theta}$ would lag $\dot{\theta}$ by 90 degrees. Therefore, if θ goes from its initial value of zero to the maximum value, M_{pt}, in time, t, then $\dot{\theta}$ would arrive at its maximum value in t/2 and $\ddot{\theta}$ would have a maximum in time t/4.

Defining $\dot{\theta}_{max}$ as,

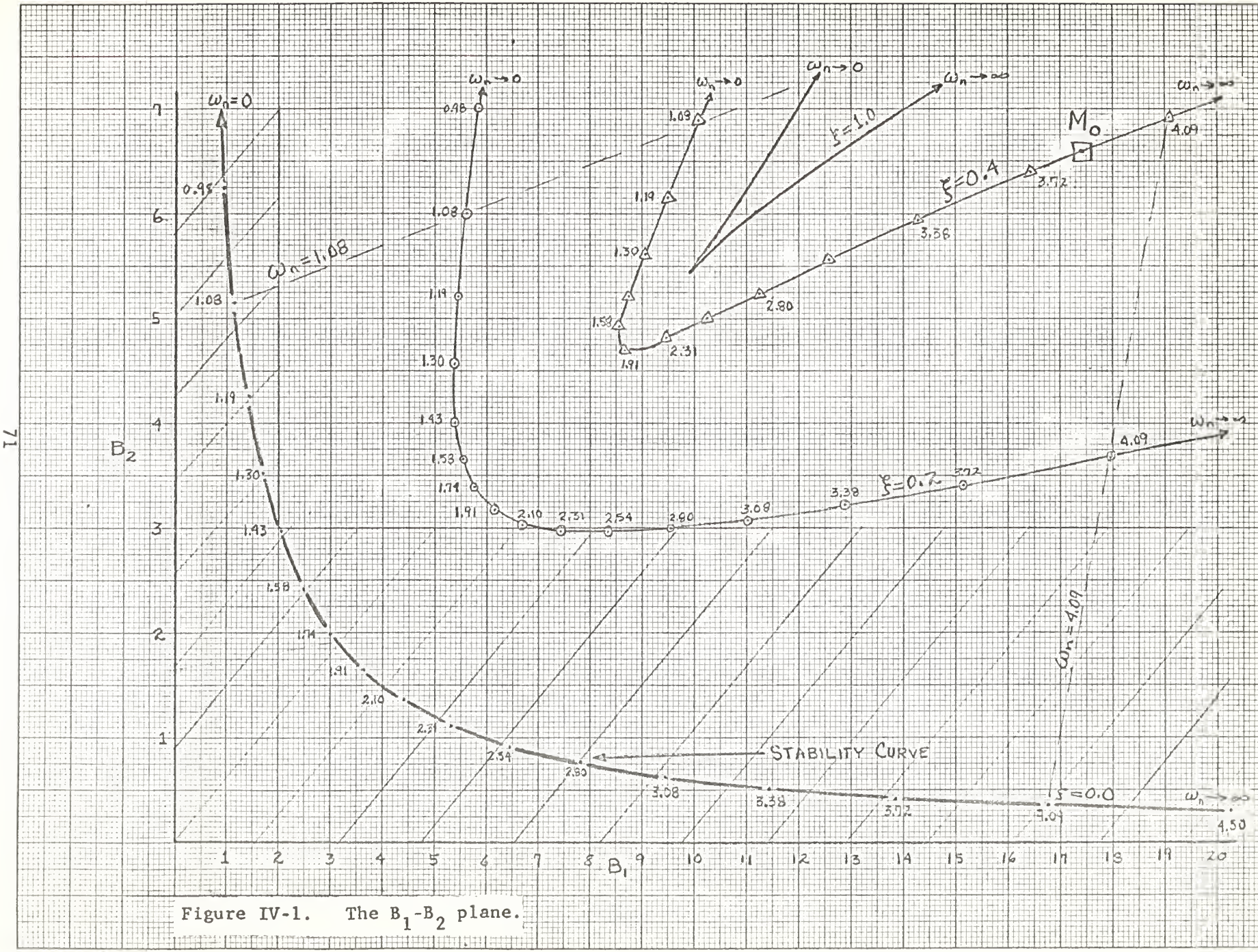

Figure IV-1. The B_1-B_2 plane.

$$\dot{\theta}_{max} = \frac{\theta_{max} - \theta(0)}{t} \qquad \text{(IV-5)}$$

and $\ddot{\theta}_{max}$ as

$$\ddot{\theta}_{max} = \frac{\dot{\theta}_{max} - \theta(0)}{t/2} \qquad \text{(IV-6)}$$

provides a basis for predicting M-point motion on the B_1-B_2 plane.

For zeta equal to 0.4 the maximum overshoot would be 1.25. Therefore, for a ten volt input, θ_{max} is 12.5 volts. For ω_n equal to 3.8 rad/sec, t equals 0.414. Substituting these values in Eq. (IV-5) gives a $\dot{\theta}_{max}$ of 30.2 volts. Therefore, $B_{1\ min}$ equals 2.231. The values of $\ddot{\theta}_{max}$ is predicted from Eq. (IV-6) as 146 volts, which corresponds to a $B_{2\ min}$ of 3.206. Thus, the M-point would be bounded by the straight dashed lines shown in Fig. IV-2. A revision to the first approximation is now made by choosing an average trajectory along the zeta equals 0.2 line and guessing at an average value of ω_n of 1.43 rad/sec. from the corner value of ω_n. Under these conditions, M_{pt} is 1.5 and t equals 1.10 seconds. Using this value of M_{pt}, θ_{max} is 15 volts and, from Eq. (IV-5), $\dot{\theta}_{max}$ is 13.6 volts and, therefore $B_{1\ min}$ is 2.52. The revised value of $\ddot{\theta}_{max}$ is computed from Eq. (IV-6) as 24.3 volts, which corresponds to a $B_{2\ min}$ of 4.23. A second revision is now made based on the curved dash line of Fig. IV-2, using a value of zeta equals 0.3 and an ω_n of 1.4. From this data, M_{pt} is 1.35, $\dot{\theta}_{max}$ is 12.0 volts and $\ddot{\theta}_{max}$ is 21.3 volts. Corresponding to $B_{1\ min} = 3.50$ and $B_{2\ min} = 3.85$. Since this second revision shows about the same M-point motion (shown by the curved dashed line in Fig. IV-2) no further revisions are made.

To predict M-point motion after the first peaks are reached, it is assumed that in one complete cycle position, velocity, and acceleration

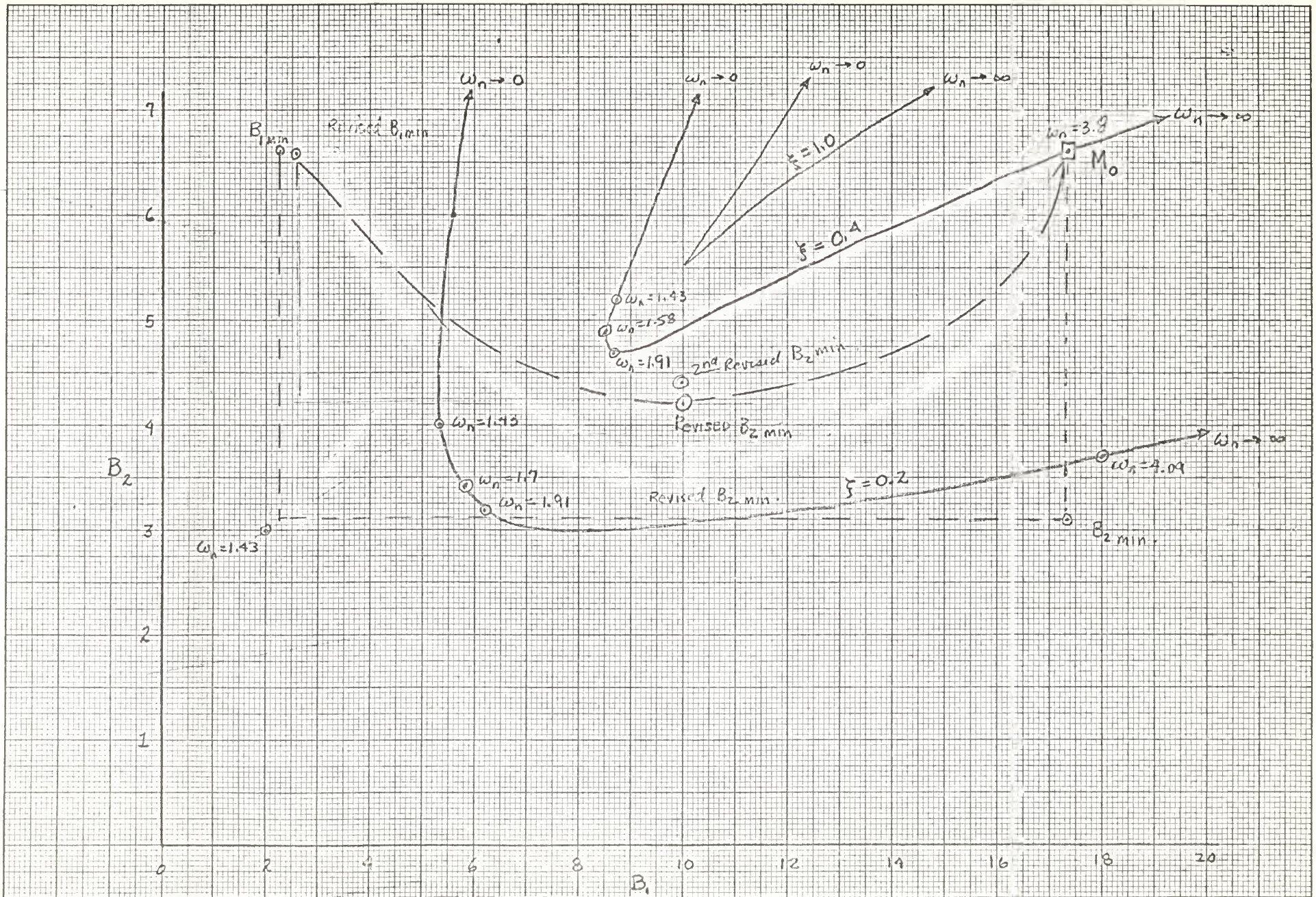

Figure IV-2. Approximate trajectories on the B_1-B_2 plane.

are all damped by a factor of $\epsilon^{-\xi}$. The following derivation of M-point motion over any one cycle is made assuming that B_1 and B_2 are non-linear throughout the entire cycle and, therefore, have values given by

$$B_1 = 2 + \frac{18}{|\dot{\theta}|}$$

and

$$B_2 = 3 + \frac{18}{|\ddot{\theta}|} .$$

It is also assumed that velocity and acceleration have an average magnitude over one cycle equal to the average magnitude of a sine wave over one cycle, i.e.,

$$\dot{\theta}_{ave} = .636\ \dot{\theta}_{peak}$$

and

$$\ddot{\theta}_{ave} = .636\ \ddot{\theta}_{peak} .$$

Therefore:

$$B_{11\ ave} = 2 + \frac{18}{.636\ |\dot{\theta}_1|} ,$$

$$B_{12\ ave} = 2 + \frac{18}{.636\ |\dot{\theta}_2|} ,$$

and

$$\Delta B_{1\ ave} = B_{12\ ave} - B_{11\ ave} = \frac{18}{.636}\left[\frac{1}{|\dot{\theta}_2|} - \frac{1}{|\dot{\theta}_1|}\right]$$

Since $|\dot{\theta}_2| = |\dot{\theta}_1|\,\epsilon^{-\xi}$, then

$$\Delta B_1 = \frac{18}{.636\ |\dot{\theta}_1|}\left[\frac{1 - \epsilon^{-\xi}}{\epsilon^{-\xi}}\right] = \frac{28.4}{|\dot{\theta}_1|}\,\delta \qquad \text{(IV-7)}$$

where δ is the damping factor.

Similarly,

$$\Delta B_2 = \frac{28.4}{|\ddot{\theta}_1|}\,\delta . \qquad \text{(IV-8)}$$

The δ factors appearing in Eqs. (IV-7 and IV-8) are tabulated in Table IV-1. Using the values of δ from the table and Eqs. (IV-7 and IV-8), a predicted average M-point trajectory is plotted in Fig. IV-3.

TABLE IV-1

ξ	δ
0.0	0.00
0.1	0.105
0.2	0.222
0.3	0.352
0.4	0.493
0.5	0.640
0.6	0.823
0.7	1.011
0.8	1.222
0.9	1.461
1.0	1.719

The results of the computations for average M-point trajectory are shown in Table IV-2.

The revised predicted trajectory for a ten volt step input was based on peak magnitudes of velocity and acceleration. If a single point average value is used based on the average value of a sine wave over a complete

TABLE IV-2

B_1	B_2	$\lvert\dot{\theta}\rvert$ (volts)	$\lvert\ddot{\theta}\rvert$ (volts)	δ	ΔB_1	ΔB_2
3.50	3.50	12.0	36.0	.105	.25	.08
3.75	3.58	10.3	31.0	.110	.30	.10
4.05	3.68	8.8	26.5	.140	.45	.15
4.50	3.83	7.2	21.7	.165	.65	.22
5.15	4.05	5.7	17.1	.210	1.05	.35
6.20	4.40	4.3	12.9	.285	1.88	.63
8.08	5.03	3.0	8.9	.423	4.00	1.35
12.08	6.38	1.8	5.3	1.719	27.10	9.20
*17.40	**6.60					

* B_1 is linear for $B_1 = 17.4$.

**B_2 is linear for $B_2 = 6.6$.

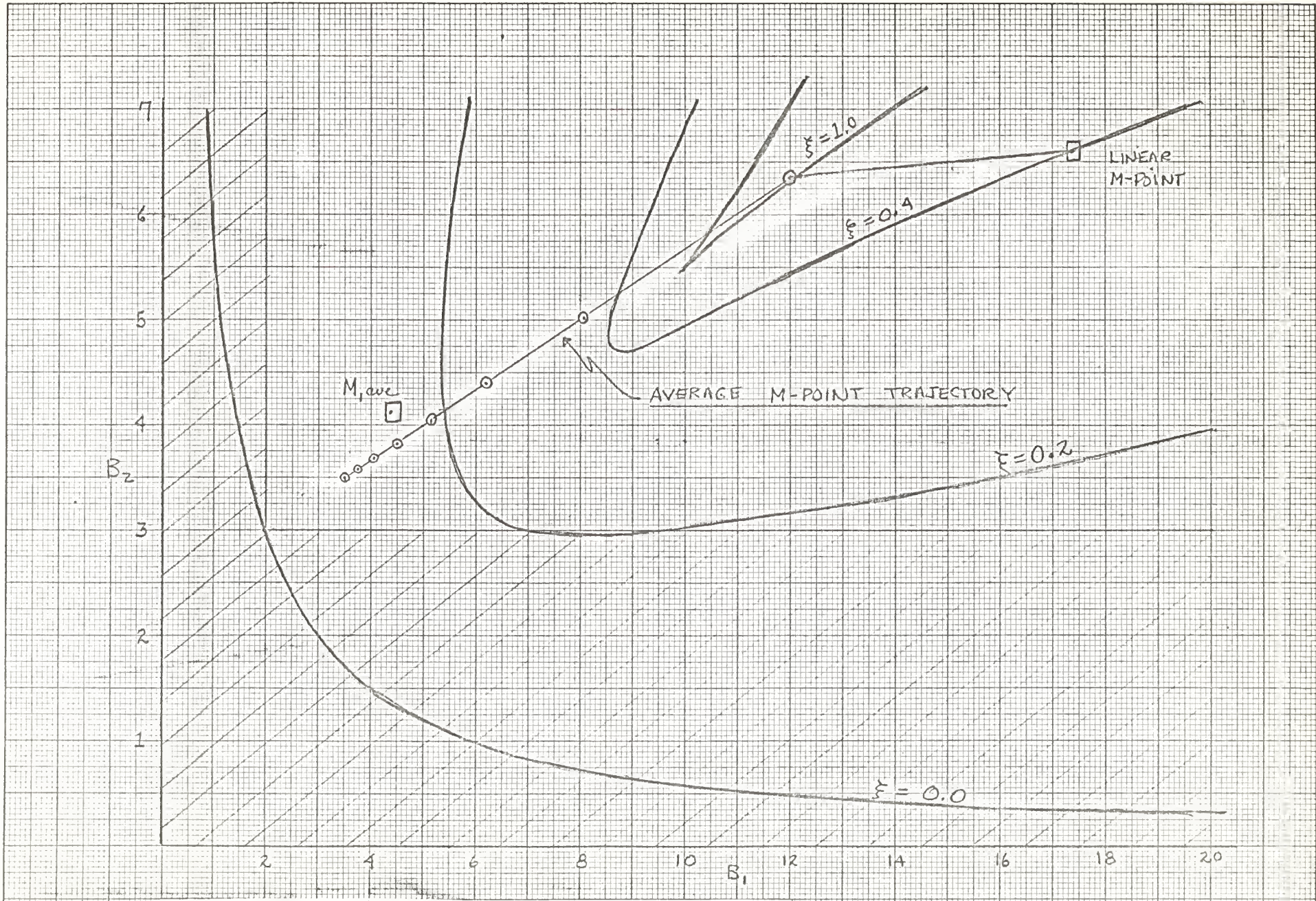

Figure IV-3. Average M-point motion on the B_1-B_2 plane.

cycle then $\dot{\theta}_{ave} = 0.63\ \dot{\theta}_{max}$ and $\ddot{\theta}_{ave} = 0.63\ddot{\theta}_{max}$. For the ten volt step input, $\dot{\theta}_{ave} = 7.55$ volts and $\ddot{\theta}_{ave} = 13.4$ volts corresponding to a $B_{1\ ave} = 4.39$ and a $B_{2\ ave} = 4.13$. This point is shown as $M_{1\ ave}$ in Fig. IV-3. According to the predictions developed here, if the first $M_{1\ ave}$ is as shown in Fig. IV-3 then about three complete oscillations should take place before the average M-point arrives at the linear M-point.

Figure IV-5 is an M-point trajectory for a 10 volt step input, for which the $\dot{\theta}$ vs $\ddot{\theta}$ phase portrait is shown in Fig. IV-4. There is only one complete oscillation in the actual system. Figures IV-6 through IV-12 are phase portraits and M-point trajectories for step inputs of 20, 30, 40, and 50 volts.

The average M-point trajectory does follow the general trend of the predicted average trajectory. However, the predicted trajectory allows for nearly twice the number of cycles as actually occur.

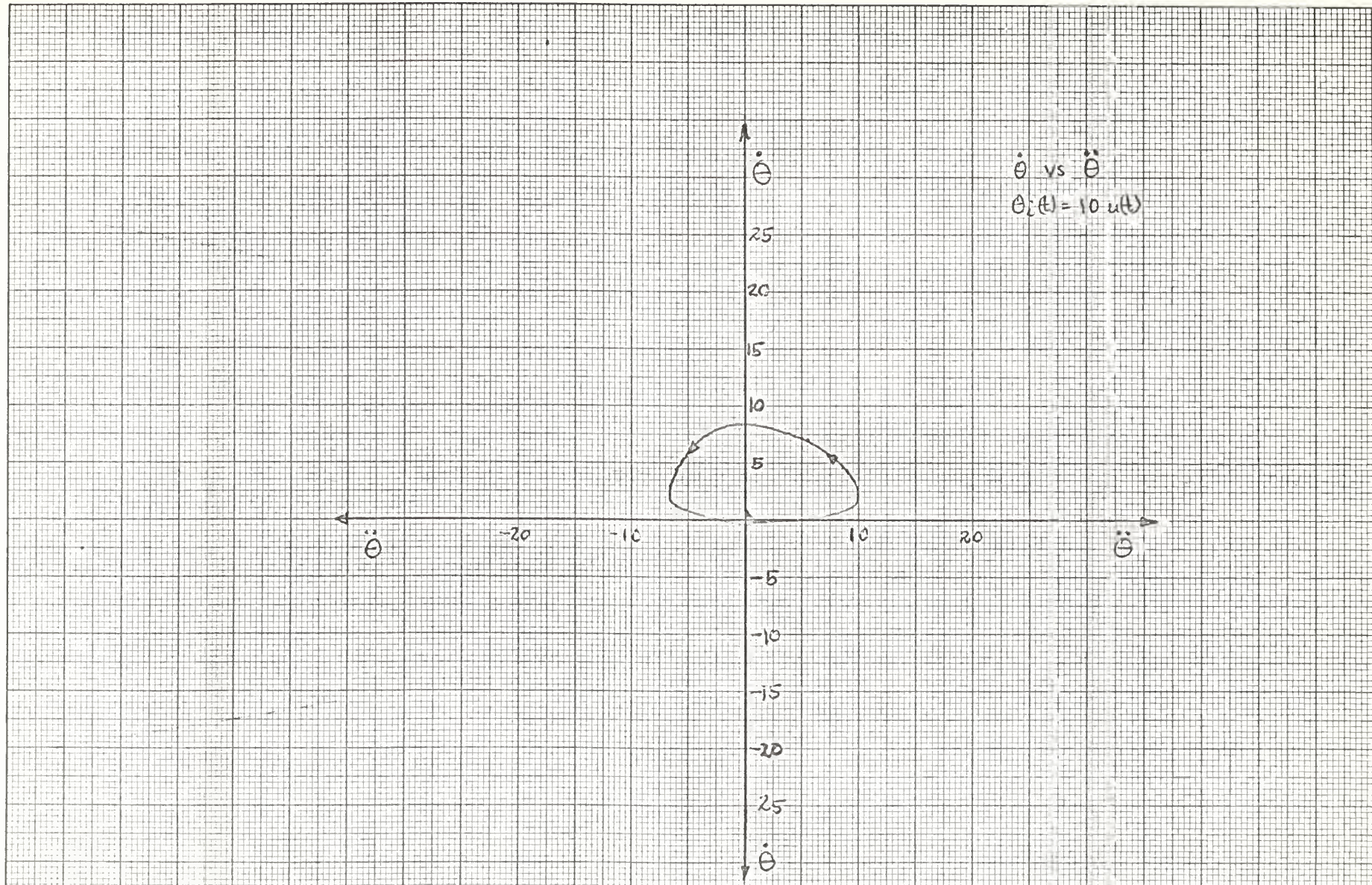

Figure IV-4. $\dot{\theta}$ vs $\ddot{\theta}$ phase portrait for 10 volt step input.

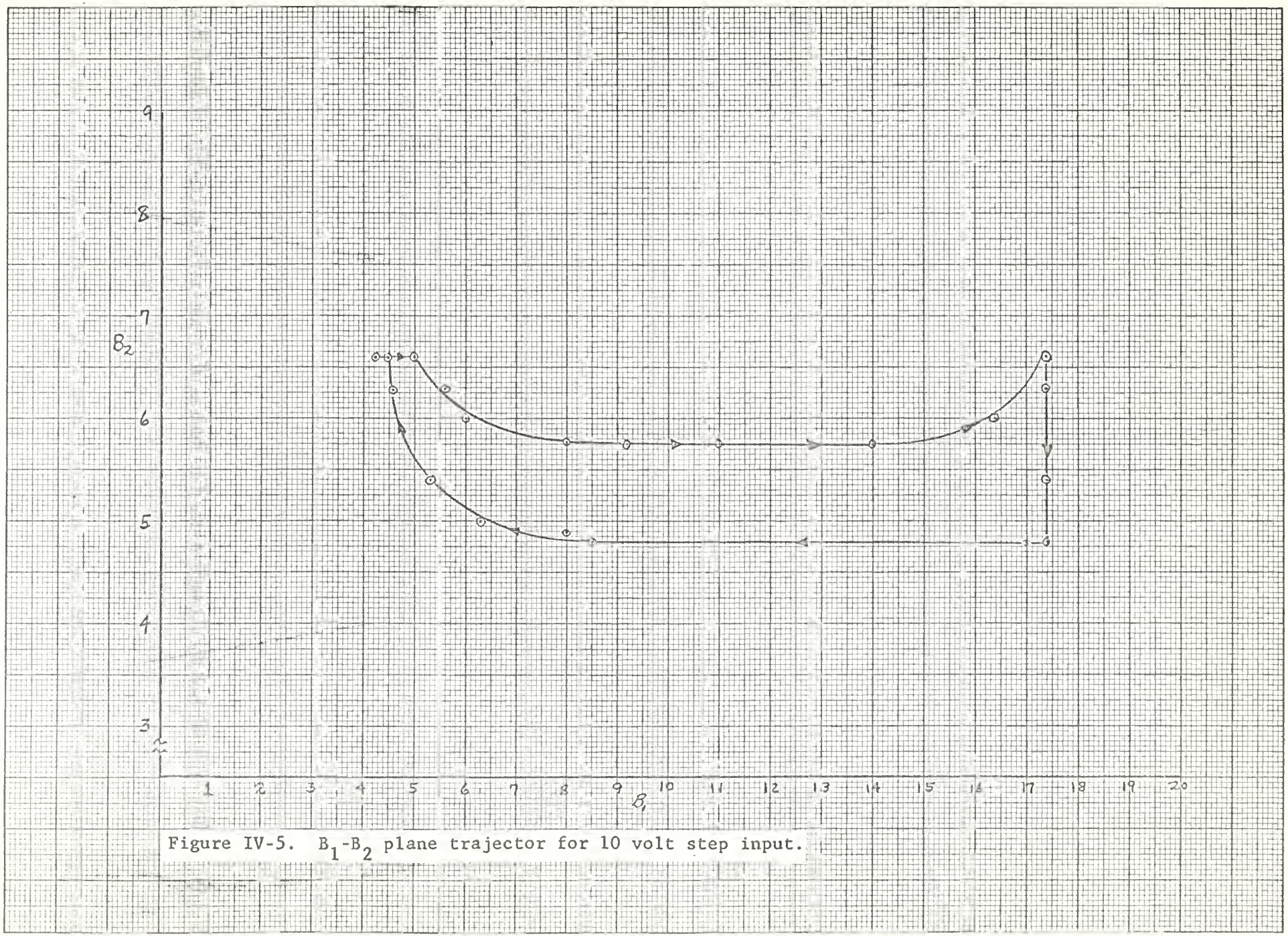

Figure IV-5. B_1-B_2 plane trajector for 10 volt step input.

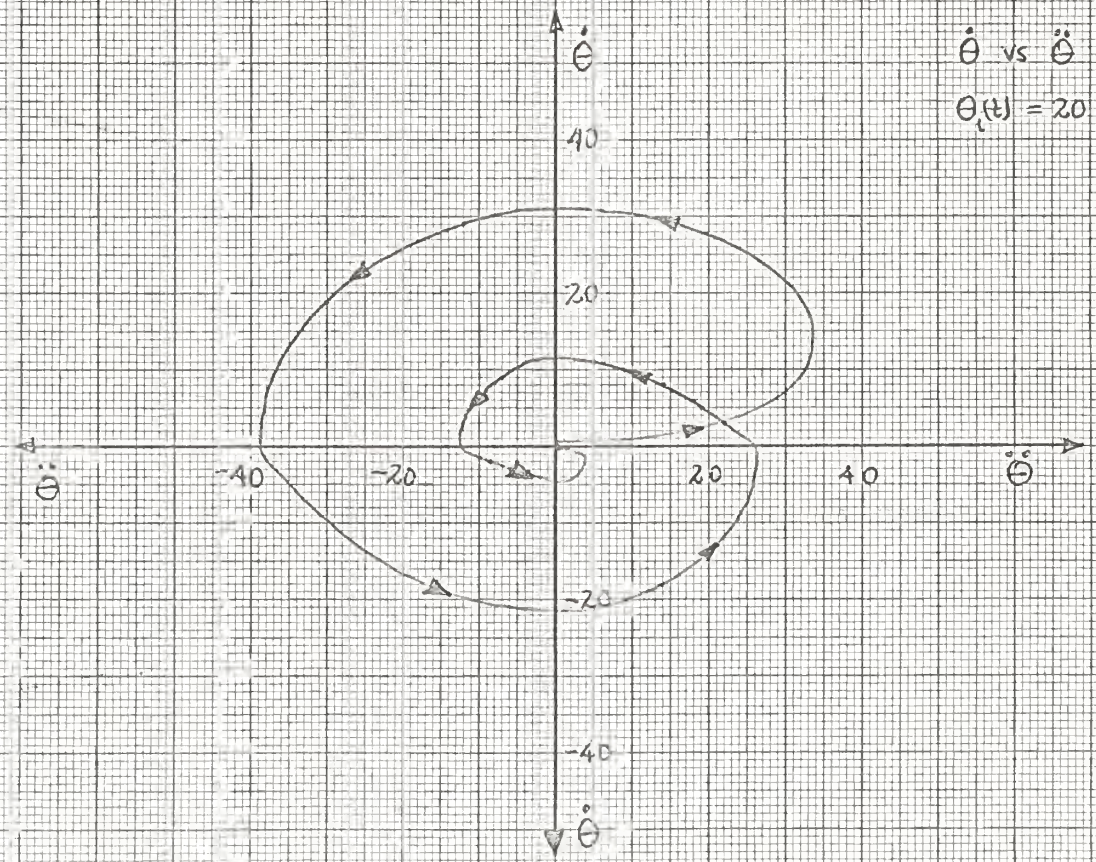

Figure IV-6. $\dot{\theta}$ vs $\ddot{\theta}$ phase portrait for 20 volt step input.

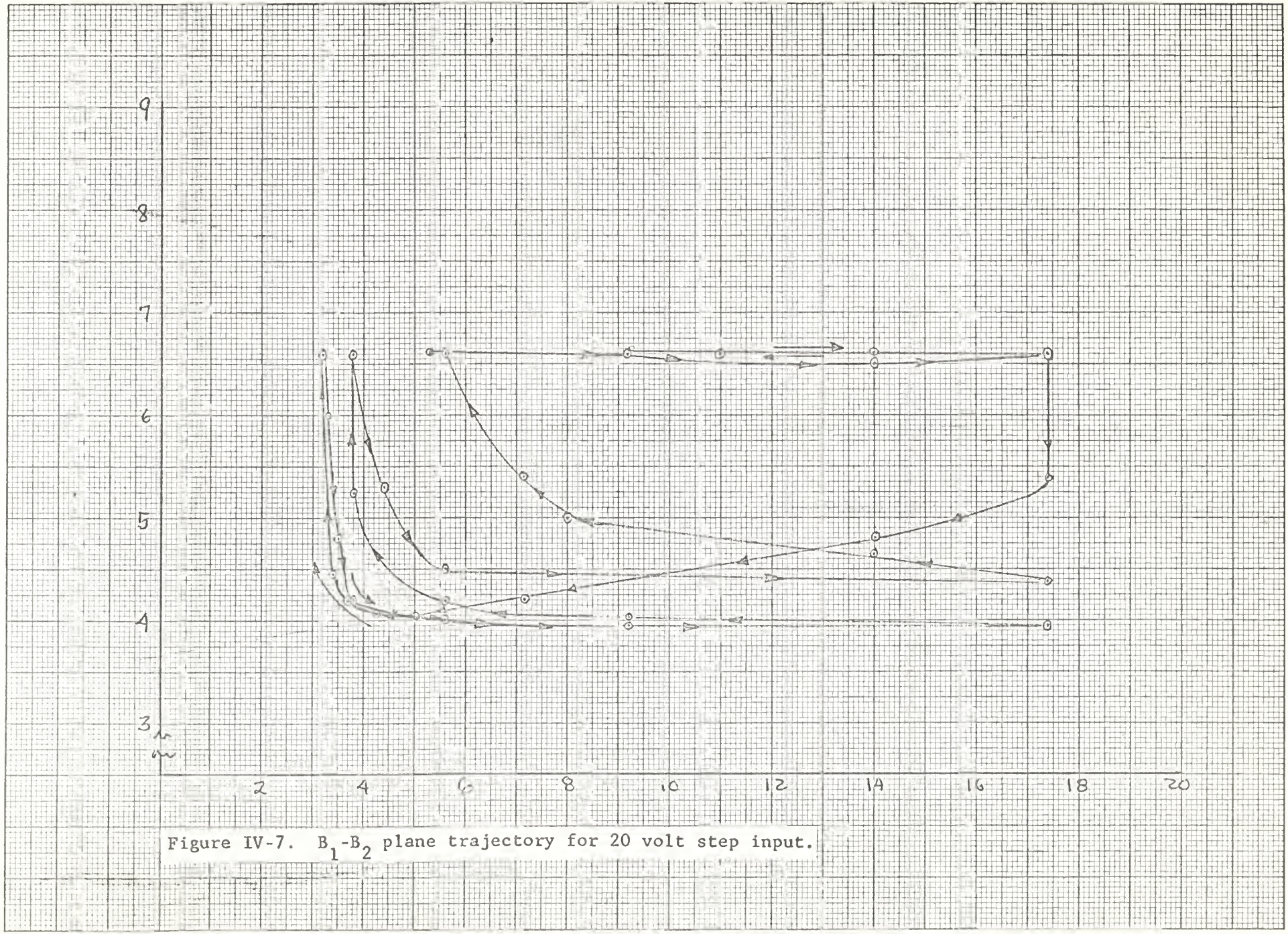

Figure IV-7. B_1-B_2 plane trajectory for 20 volt step input.

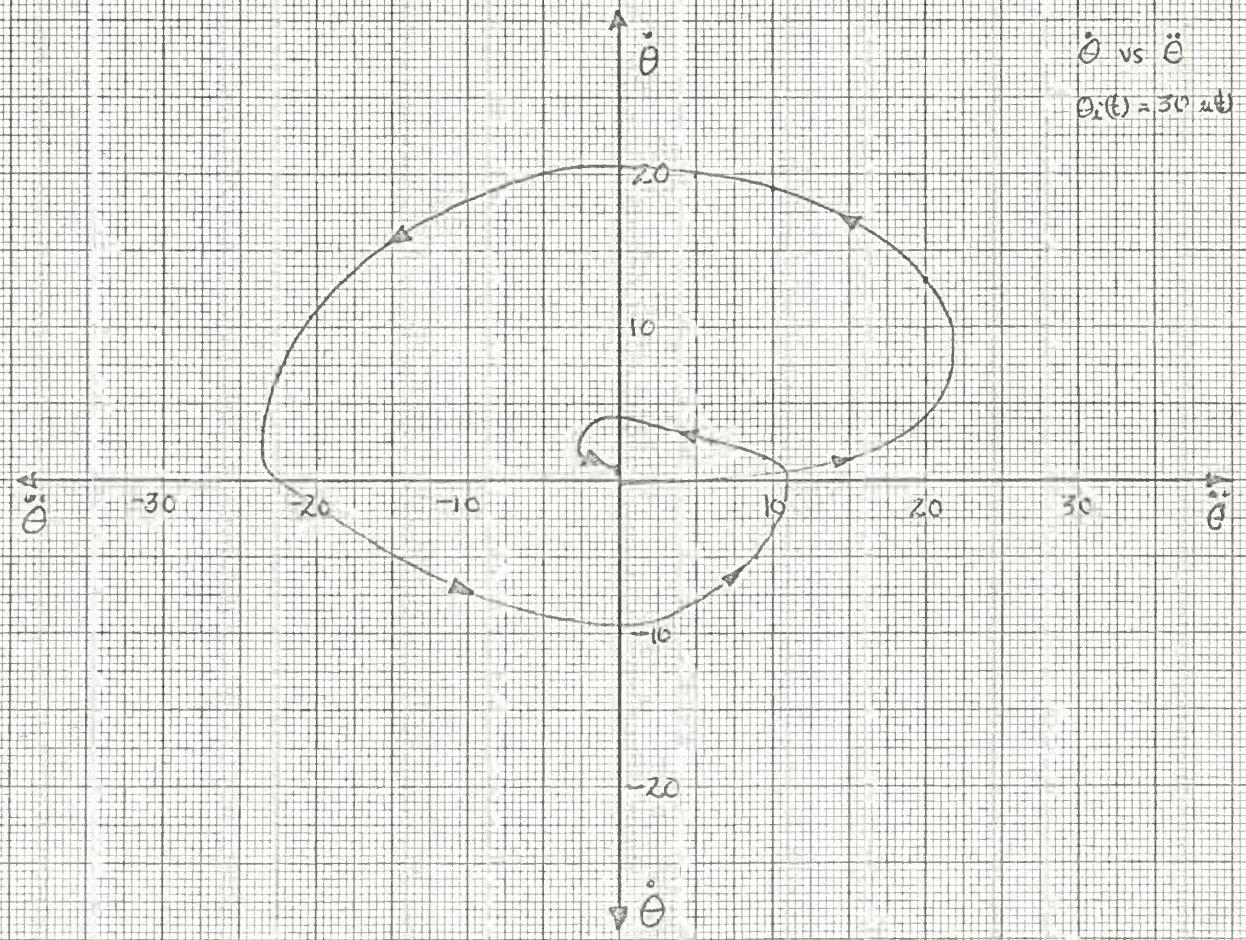

Figure IV-8. $\dot{\theta}$ vs $\ddot{\theta}$ phase portrait for 30 volt step input.

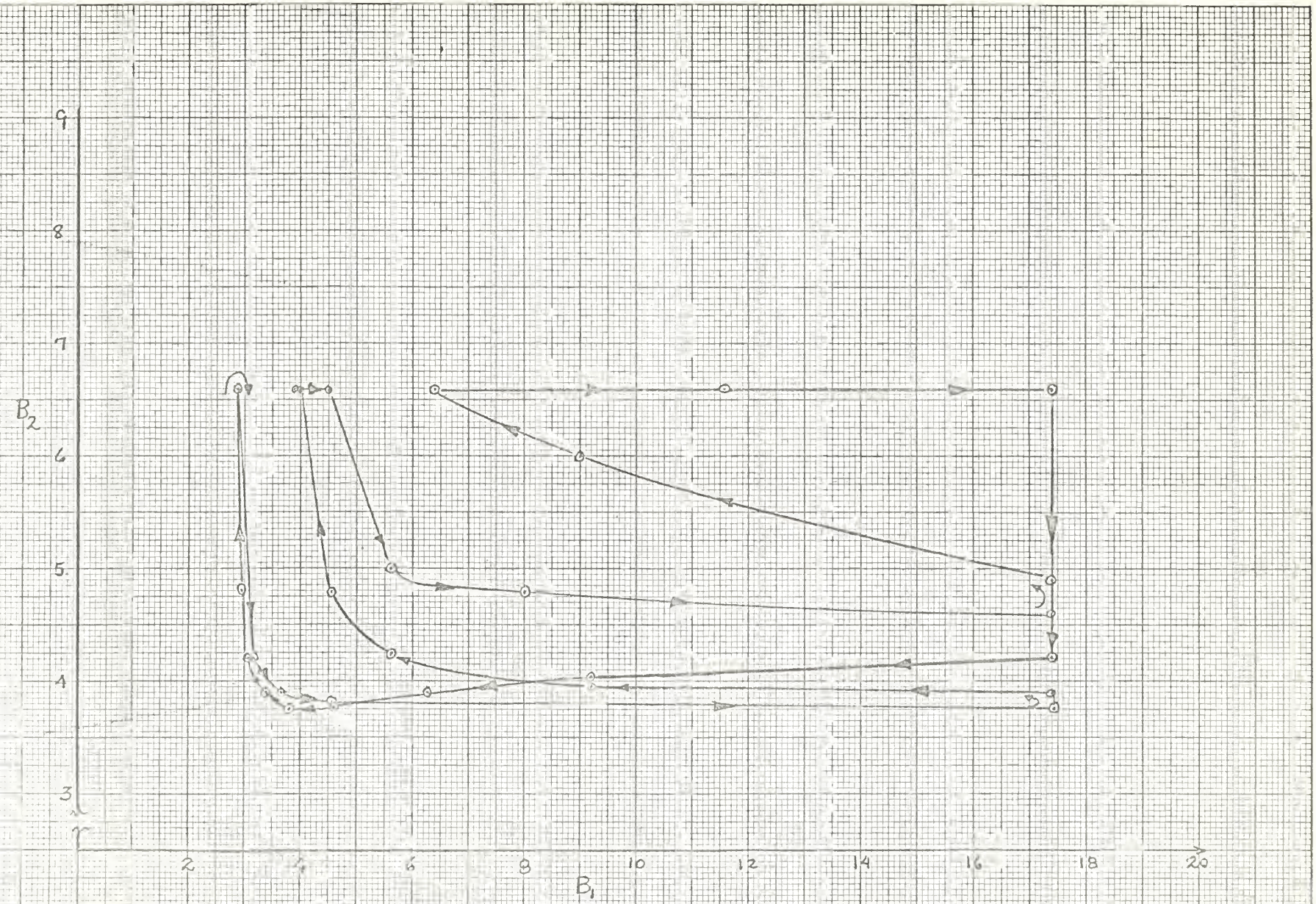

Figure IV-9. B_1-B_2 plane trajectory for 30 volt step input.

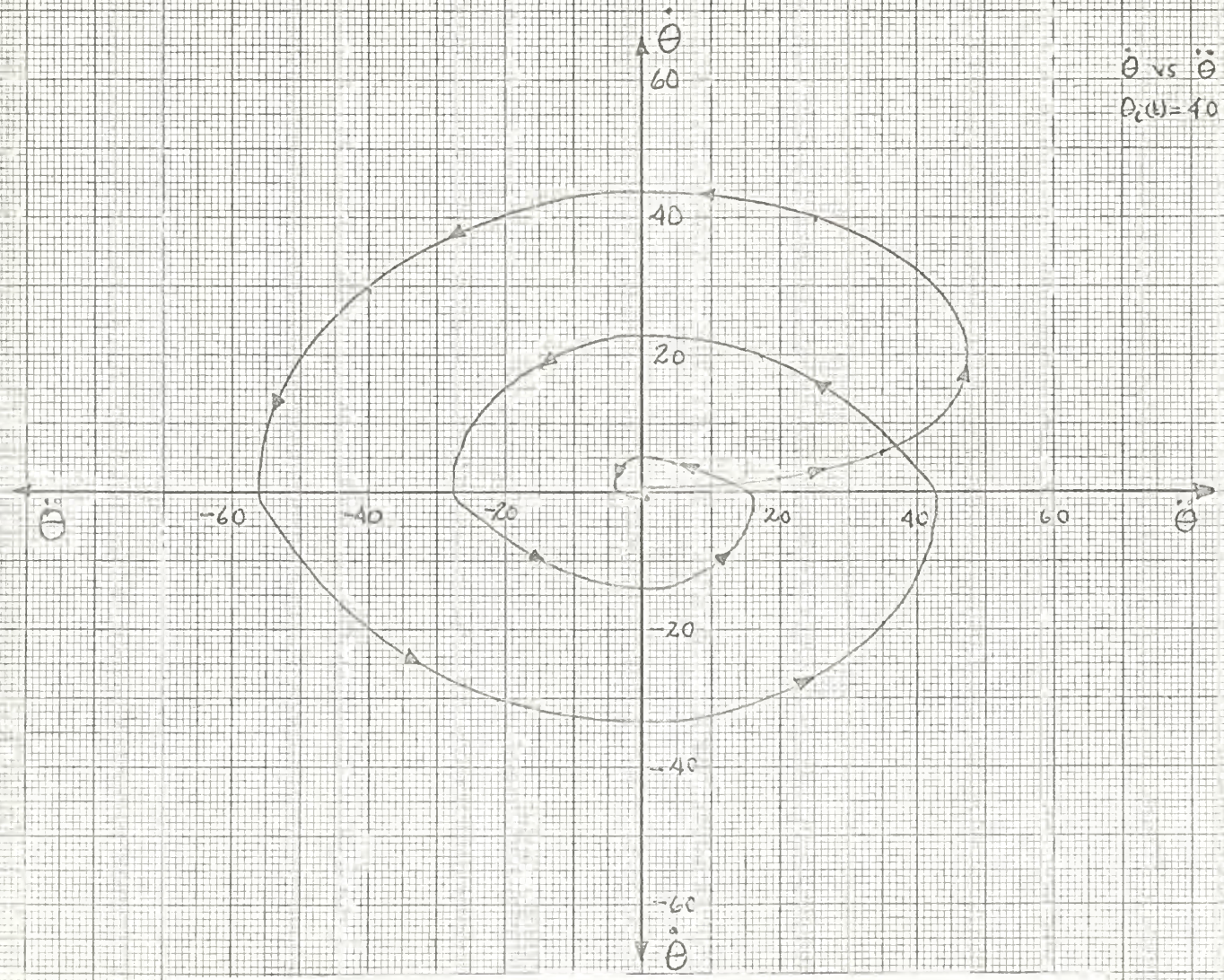

Figure IV-10. $\dot{\theta}$ vs $\ddot{\theta}$ phase portrait for 40 volt step input.

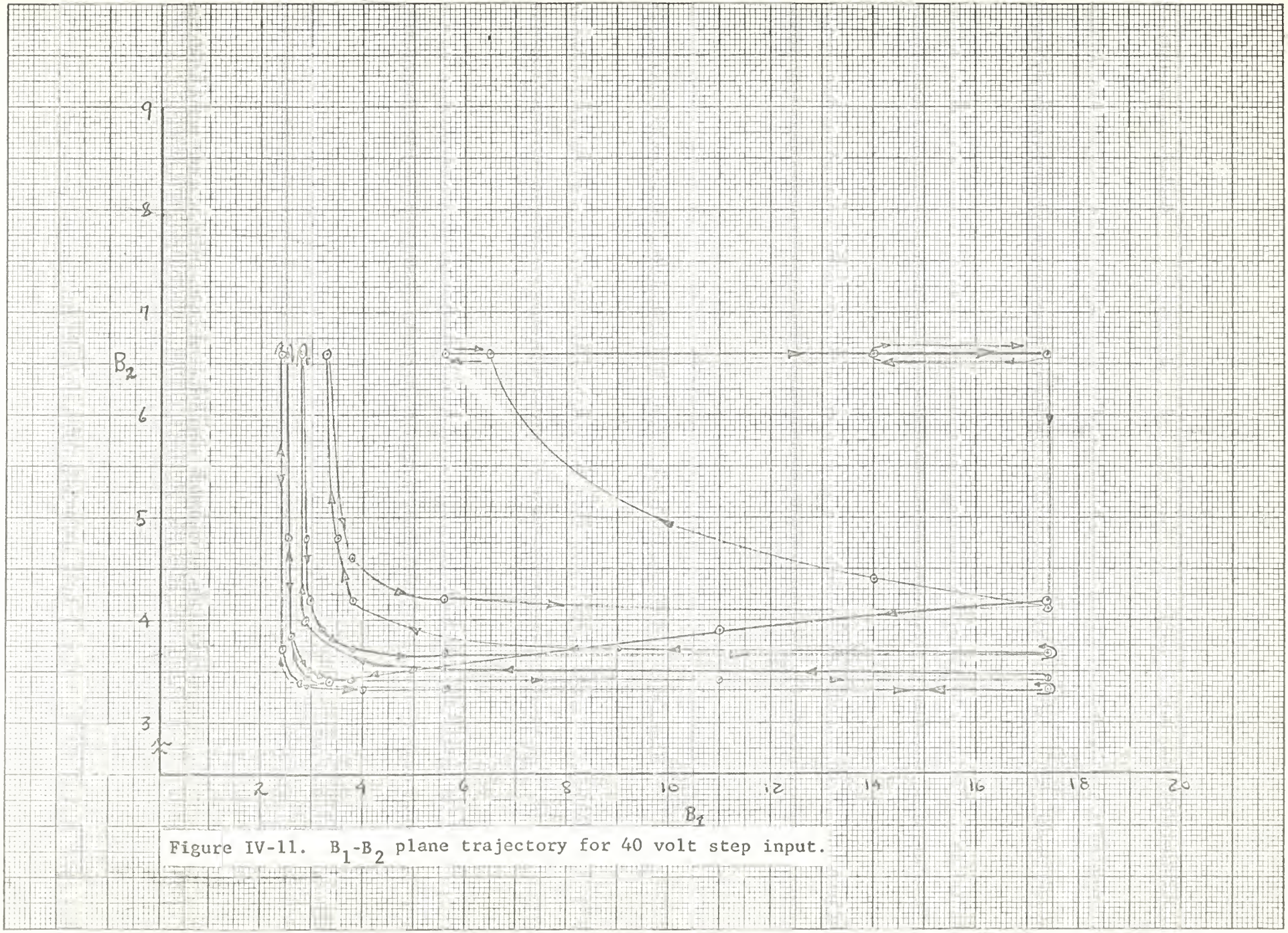

Figure IV-11. B_1-B_2 plane trajectory for 40 volt step input.

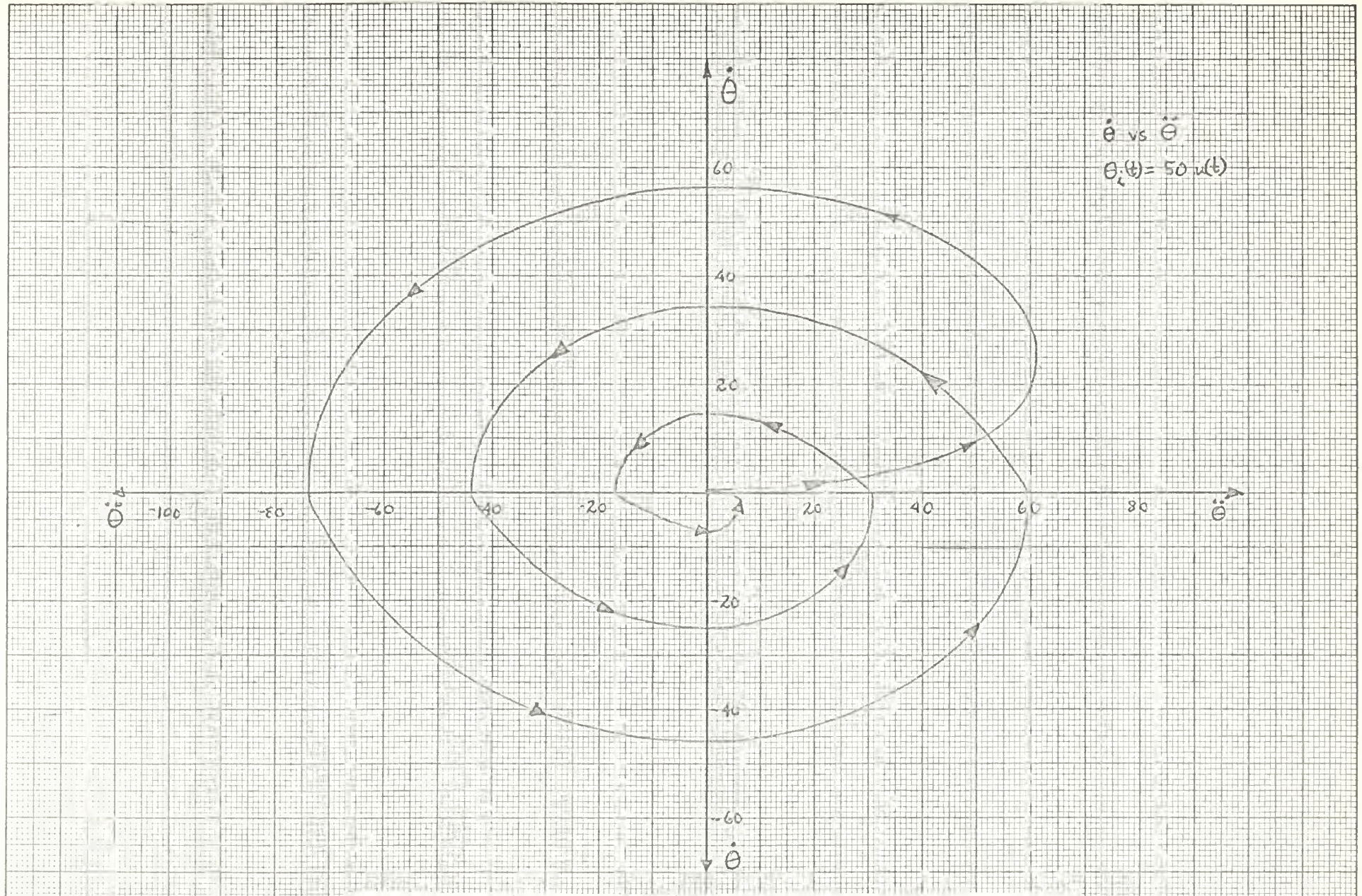

Figure IV-12. $\dot{\theta}$ vs $\ddot{\theta}$ phase portrait for 50 volt step input.

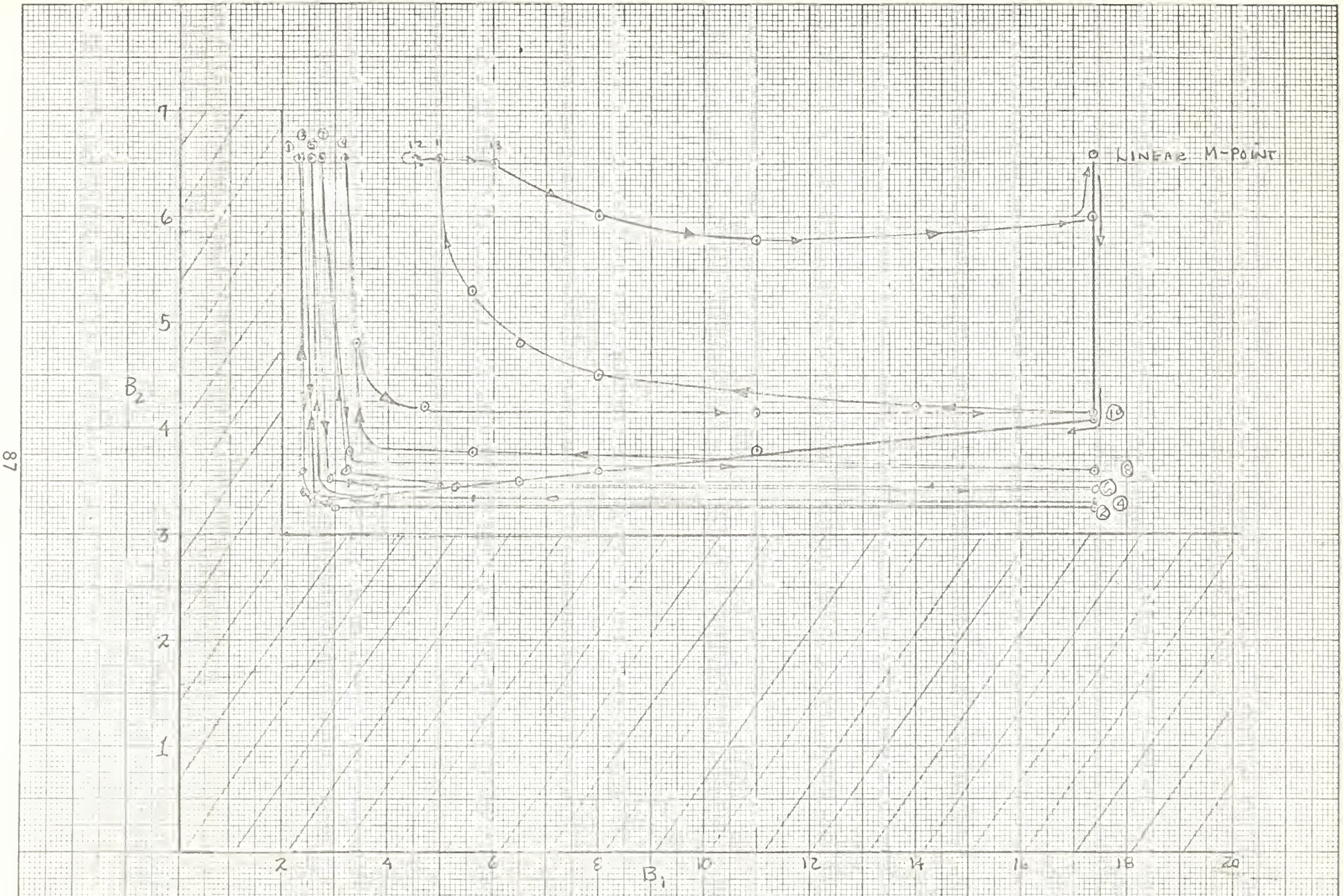

Figure IV-13. B_1-B_2 plane trajectory for 50 volt step input.

CONCLUSIONS.

There are two primary sources for error in the predicted M-point trajectory. The first source is in predicting the initial values of velocity and acceleration and is due to the delay in position response after the step input is applied. This results in erroneous values of the first velocity and acceleration peak magnitudes.

The second source is in assuming a sinusoidal response when the actual response is a damped sinusoid. The damped sinusoid has a lower average magnitude over a cycle than a pure sinusoid and, thus, the predicted number of complete oscillations are greater than the actual number.

APPENDIX A

SECOND ORDER SYSTEMS WITH SINGLE NONLINEARITIES

CASE I. SATURATION IN THE ERROR CHANNEL.

The block diagram of the system to be analyzed and the analog computer simulation of the system are shown in Fig. A-1. The closed loop transfer function for this system is

$$\frac{\theta_o(s)}{\theta_i(s)} = \frac{10\,N}{S^3 + 3S^2 + 2S + 10N} \tag{A-1}$$

where N represents the instantaneous variable gain of the saturation nonlinearity. By choosing the last two coefficients of the characteristic equation as the variable coefficients, the characteristic equation becomes

$$S^3 + 3S^2 + B_1 S + B_o = 0. \tag{A-2}$$

From Appendix B, Mitrovic's equations for B_0 and B_1 are:

$$B_o = -\left[3\omega_n^2 \phi_1(\xi) + \omega_n^3 \phi_2(\xi)\right] \tag{A-3}$$

and

$$B_1 = 3\omega_n \phi_2(\xi) + \omega_n^2 \phi_3(\xi) \; . \tag{A-4}$$

Substituting the values of the ϕ functions for $\xi = 0$ from Appendix B in Eqs. (A-3) and (A-4) gives the parametric equations of the stability curve as

$$B_o = 3\omega_n^2 \tag{A-5}$$

and

$$B_1 = \omega_n^2 \; . \tag{A-6}$$

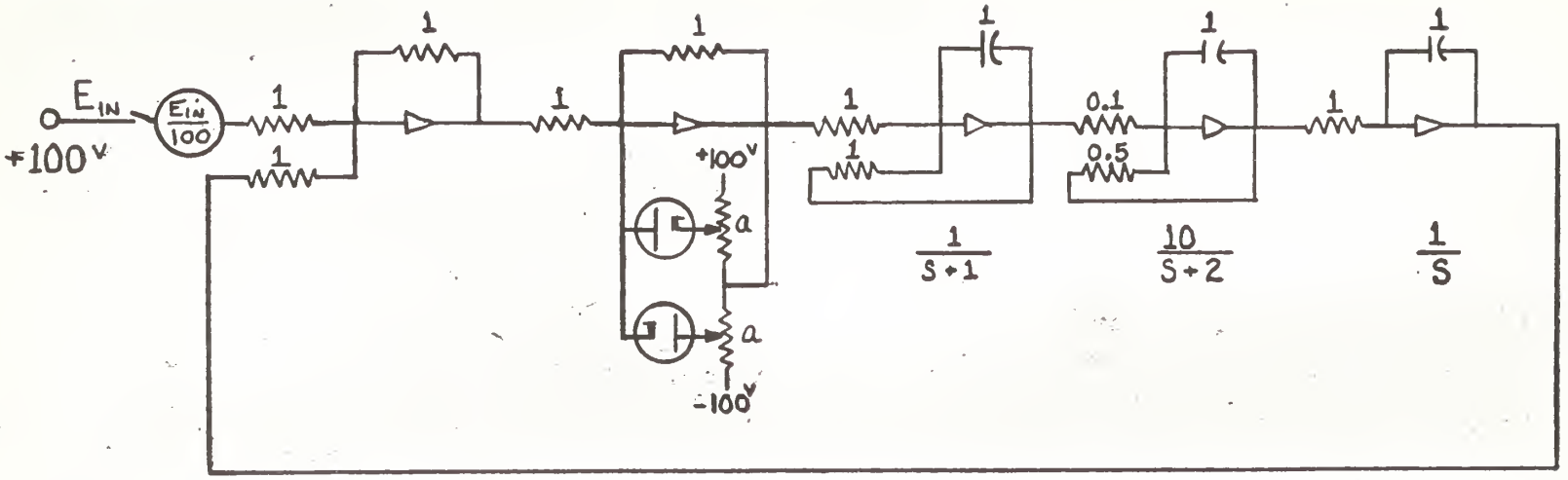

(a) COMPUTER SIMULATION (RESISTANCE IN MEGOHMS, CAPACITANCE IN μFARADS, $a = 0.05$)

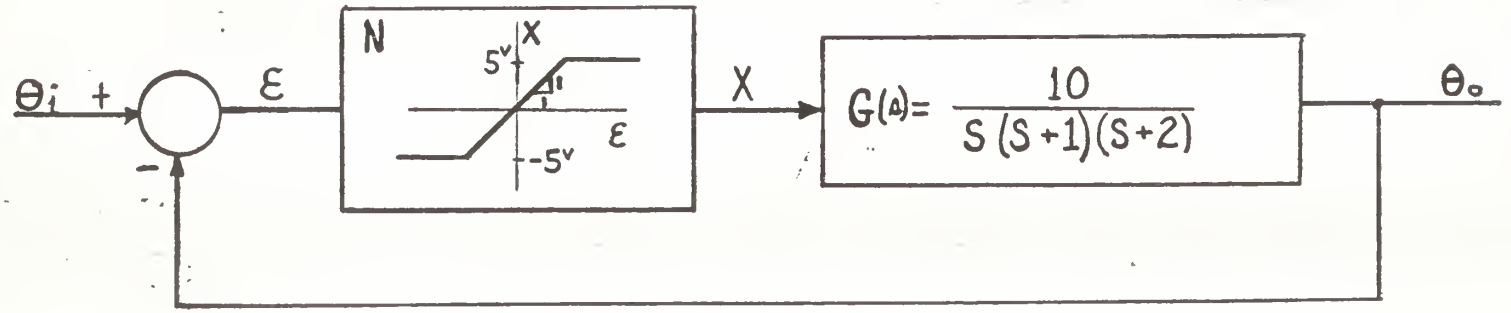

(b) BLOCK DIAGRAM

FIGURE A-1

CONTROL SYSTEM WITH SATURATION IN THE ERROR CHANNEL.

Fig. [illegible] is the B_0 - B_1 plane with the values of B_0 and B_1 from Eq. (A-5) and (A-6) plotted as ω_n is varied. Thus the stability curve is shown. By comparing Eq. (A-1) with Eq. (A-2), it is seen that $B_1 = 2$ and $B_0 = 10N$ where N has a maximum value of one. Thus an N point locus is specified on the B_0 - B_1 plane.

The intersection of the N-point locus with the stability curve defines a single point where all the equations for B_0 and B_1 are satisfied. At this point,

$$B_o = 3\omega_n^2 = 10N \tag{A-7}$$

and

$$B_1 = \omega_n^2 = 2 . \tag{A-8}$$

The solution of Eq. (A-8) gives $\omega_n = 1.414$ rad/sec. Substituting this value of ω_n in Eq. (A-7) yields $N = 0.6$. Since the variable gain of the saturation nonlinearity is defined as the ratio of the output to the input, the magnitude of the error signal can be predicted from Eq. (A-9) below as 8.3 volts.

$$\mathcal{E} = \frac{5}{N} \text{ volts} \tag{A-9}$$

The linear system with a gain of 10 is unstable. Thus, if any disturbance occurs in the system, the output signal will begin to increase in magnitude. Therefore, the error signal also increases in magnitude. When the error channel saturates the gain of the system is decreased. As the system gain is decreased, the system becomes more stable and the error signal begins to decrease. A decrease in the error signal increases the system gain and the above process is repeated.

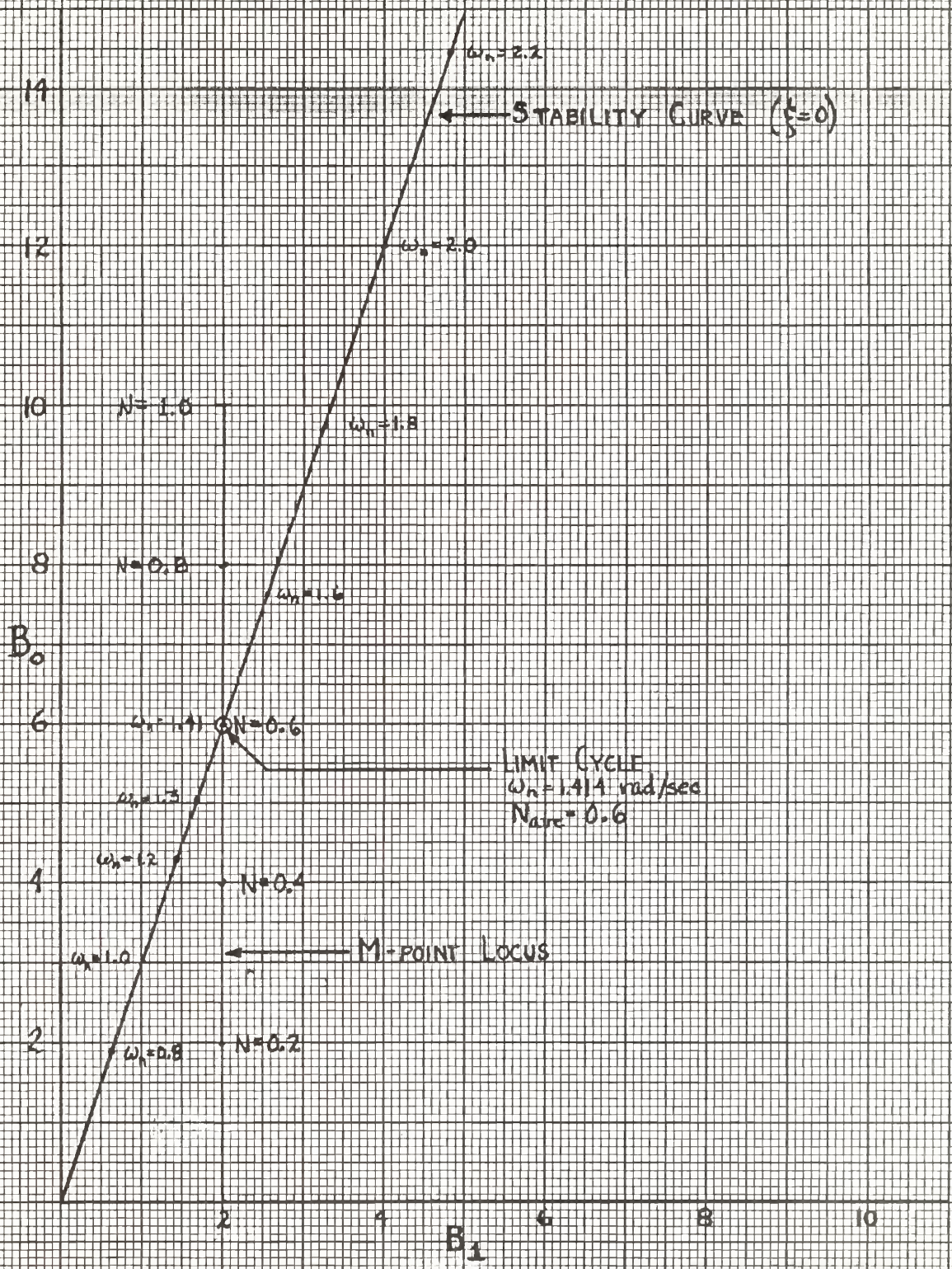

FIGURE A-2

Graphical solution to error channel saturation

Eventually a dynamic equilibrium is reached in which the system oscillates along the M-point locus at the intersection of the M-point locus and the stability curve. The value of the nonlinear gain, N, and the magnitude of the error signal, $\mathcal{E}$, are therefore time averaged values.

Fig. A-3 is a phase portrait of this system obtained with an analog computer simulation of the system. The radian frequency of 1.395 rad/sec. agrees within one percent of the predicted value of $\omega_n = 1.414$ rad/sec. As previously stated, the magnitude of the error signal, $\mathcal{E}$, when the system is operating in a limit cycle can be predicted as 8.33 volts. When the error channel saturates, the system will be driven with a constant input of five volts. Therefore, the system should be driven at the same rate in either a positive or a negative direction and the error signal channel should spend the same amount of time in positive saturation as it does in negative saturation. The predicted magnitude of the error signal should then be an average value which is independent of the sign of the error signal. On Fig. A-3 a vertical line was drawn at $\mathcal{E} = -8.4$ volts. Then, for the limit cycle, the area marked "A" can be compared to the area marked "B" by counting the number of squares contained in each area. The two areas are equal and, therefore, the average magnitude of the error signal is 8.4 volts which agrees closely with the predicted value.

Fig. A-4 shows the graphical solution to this nonlinear problem on the $B_0 - B_3$ plane and the $B_0 - B_2$ plane. The solution for the $B_0 - B_3$ plane follows the same pattern as that for the $B_0 - B_1$ plane. Solving this problem on the $B_0 - B_2$ plane is, however, somewhat unique and is explained in the following paragraphs.

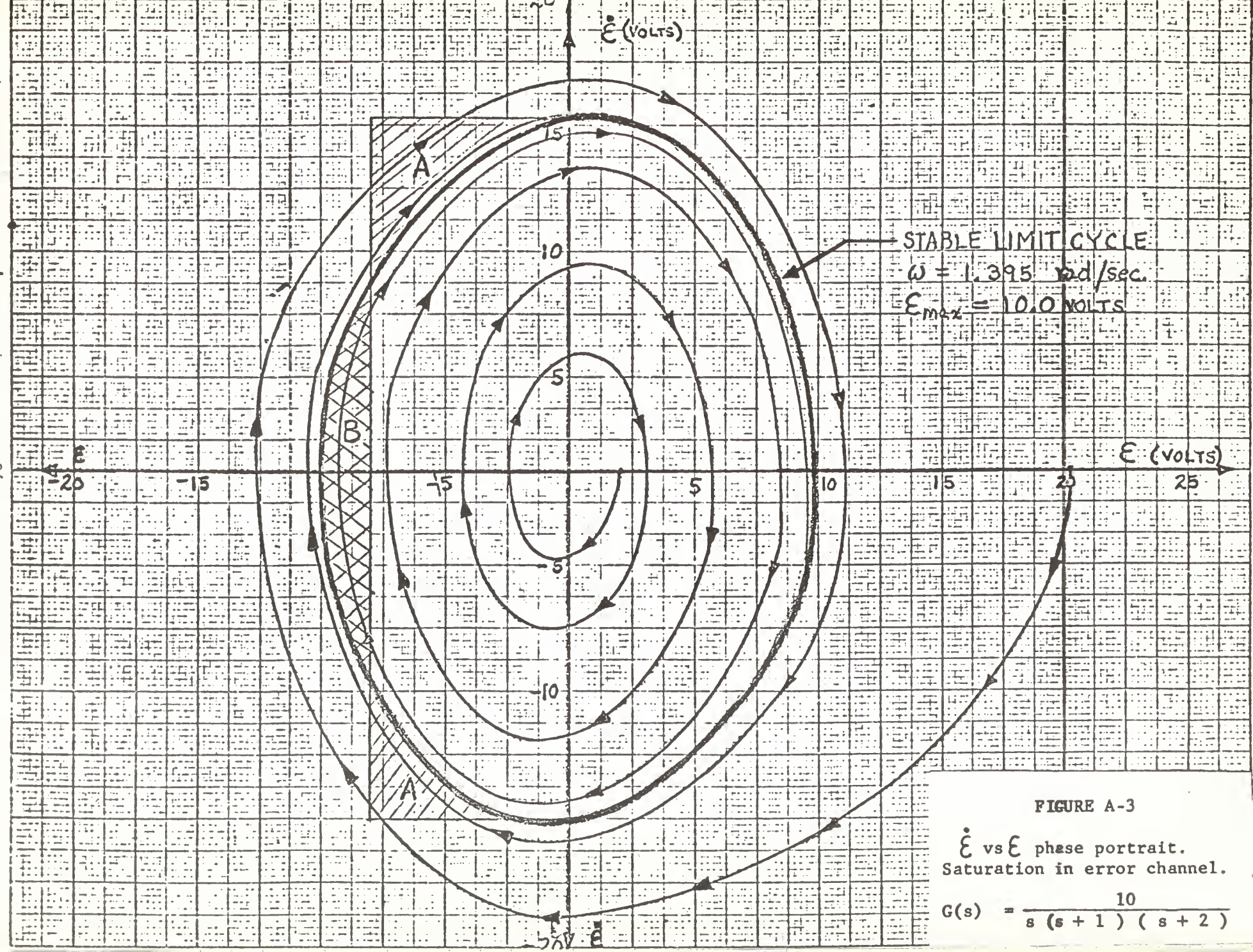

FIGURE A-3

$\dot{\varepsilon}$ vs ε phase portrait.
Saturation in error channel.

$$G(s) = \frac{10}{s\,(s+1)\,(s+2)}$$

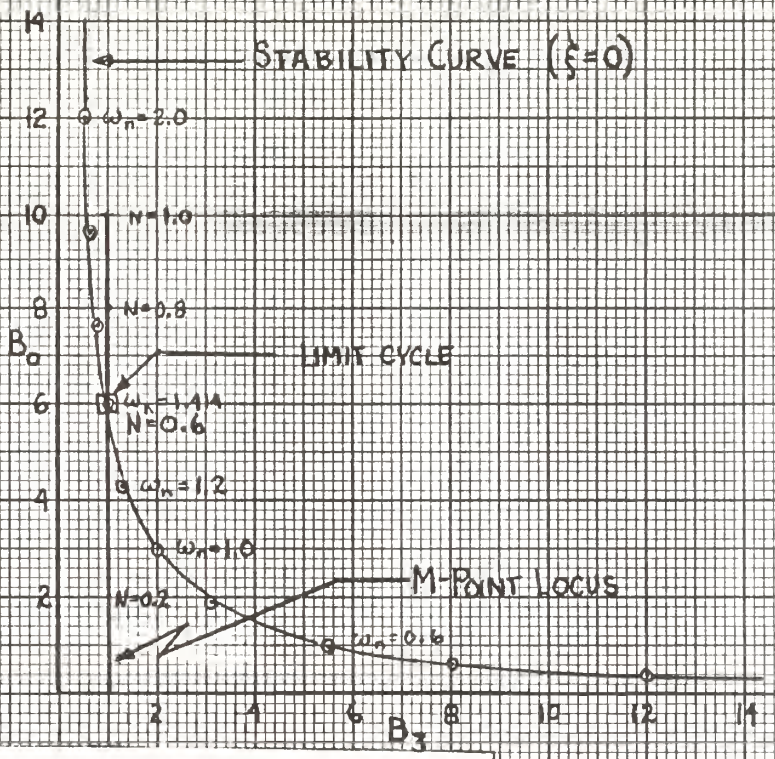

A-4a. B_0 - B_3 graphical solution.

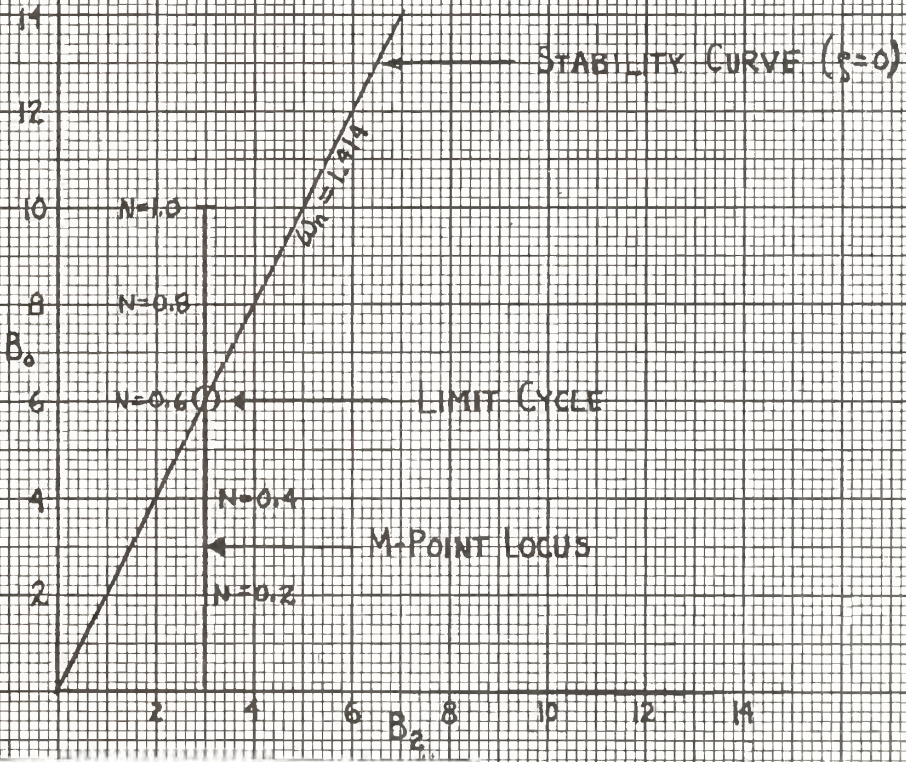

A-4b. B_0 - B_2 graphical solution.

Figure A-4. Graphical solution to error channel saturation.

From Appendix I, the Nitrovic equations for this system and the appropriate coefficients from the characteristic equation used are

$$B_0 = \frac{1}{\phi_2(\xi)} \left[2\omega_n \phi_1(\xi) + \omega_n^3 \phi_1(\xi) \right] \tag{A-10}$$

and

$$B_2 = \frac{1}{\omega_n^2 \phi_2(\xi)} \left[-2\omega_n \phi_1(\xi) - \omega_n^3 \phi_3(\xi) \right]. \tag{A-11}$$

When the $\phi(\xi)$ functions are substituted in Eqs. (A-10) and (A-11) they become:

$$B_0 = \frac{1}{2\xi} \left[2\omega_n + \omega_n^3 \right] \tag{A-12}$$

and

$$B_2 = \frac{1}{\omega_n^2 (2\xi)} \left[2\omega_n - \omega_n^3 (1 - 4\xi^2) \right]. \tag{A-13}$$

The substitution of $\xi = 0$ in Eqs. (A-12) and (A-13) results in singularities in both equations. But, for $\xi = 0$, $s = j\omega_n$. Substituting this quantity for s in Eq. (A-2) yields

$$-j\omega_n^3 - B_2\omega_n^2 + 2j\omega_n + B_0 = 0. \tag{A-14}$$

Requiring the real and imaginary parts of Eq. (A-14) to go to zero independently produces the following equation pair.

$$j\omega_n(2 - \omega_n^2) = 0 \tag{A-15}$$

$$B_0 - B_2\omega_n^2 = 0. \tag{A-16}$$

The solution to Eq. (A-15), after first dividing out $j\omega_n$, is $\omega_n^2 = 2$. Thus, $\omega_n = 1.414$ rad/sec and, from Eq. (A-16), $B_0 = 2B_2$. Since $B_2 =$

3 from the characteristic equation, then $B_0 = 6$ and $N = 0.6$. The $B_0 - B_2$ curves are then plotted and a graphical solution is obtained which is consistent with the solutions from the $B_0 - B_1$ and $B_0 - B_3$ planes.

CASE II. SATURATION IN THE VELOCITY FEEDBACK CHANNEL.

The block diagram of the system to be analyzed and the analog computer simulation of the system are shown in Fig. A-5. The closed loop transfer function for this system is

$$\frac{\theta_o(s)}{\theta_i(s)} = \frac{30}{s^4 + 7s^3 + 14s^2 + (8+120N)s + 30} \qquad \text{(A-17)}$$

where N represents the variable gain of the nonlinearity. As in Case I, the last two coefficients of the characteristic equation are chosen as the variable coefficients. The characteristic equation is

$$s^4 + 7s^3 + 14s^2 + B_1 s + B_o = 0 \qquad \text{(A-18)}$$

where

$$B_o = 30, \qquad \text{(A-19)}$$

and

$$B_1 = 8 + 120N. \qquad \text{(A-20)}$$

From Appendix B, Mitrovic's equations for B_0 and B_1 are:

$$B_o = -\left[14\omega_n^2\phi_1(\xi) + 7\omega_n^3\phi_2(\xi) + \omega_n^4\phi_3(\xi)\right] \qquad \text{(A-21)}$$

and

$$B_1 = 14\omega_n\phi_2(\xi) + 7\omega_n^2\phi_3(\xi) + \omega_n^3\phi_4(\xi), \qquad \text{(A-22)}$$

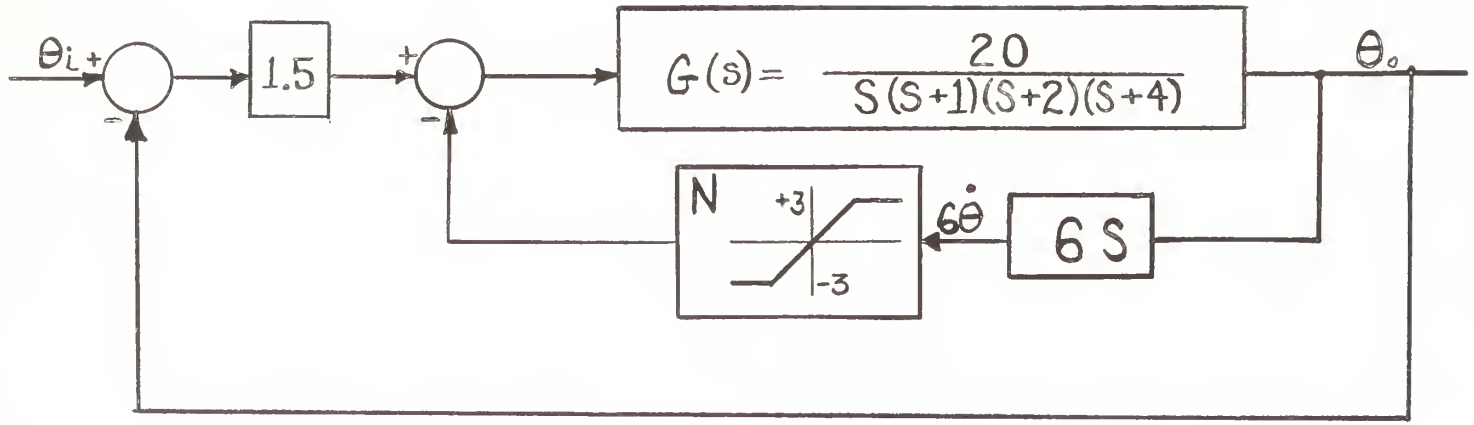

(a) System block diagram.

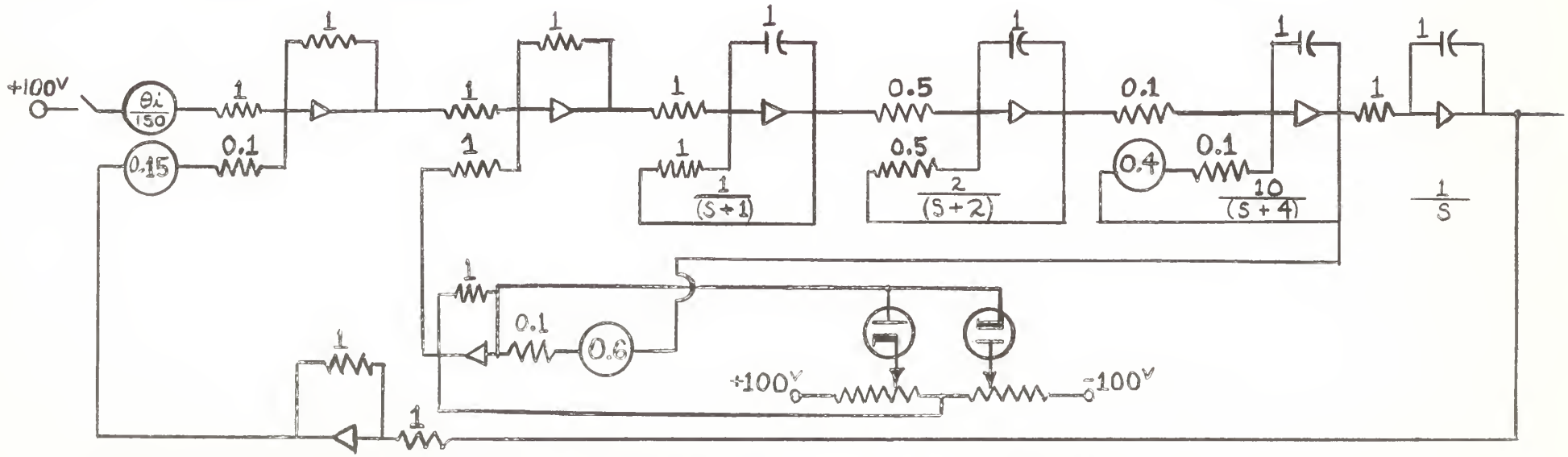

(b) Computer simulation (resistance in meghoms, capacitance in microfarads.)

Figure A-5

Feedback control system with saturation in the tachometer feedback channel.

Substituting the $\Psi(\xi)$ functions for $\xi = 0$ from Appendix B in Eqs (A-21) and (A-22) provides the following equations for the stability curves.

$$B_0 = 14\omega_n^2 - \omega_n^4. \tag{A-23}$$

$$B_1 = 7\omega_n^2. \tag{A-24}$$

The stability curve and M-point locus are plotted on the B_0 - B_1 plane on Fig. A-6.

The graphical solution to this problem reveals both a stable and an unstable limit cycle. The gain of the linear system (N = 1.0) is high enough so that the linear system is unstable. Any disturbance that occurs in the system produces an oscillatory state. When the velocity feedback signal saturates the feedback channel, the value of the nonlinear gain is reduced. The M-point moves to the left toward the stability curve. If the average M-point moves to the left of (or inside) the stability curve the system is damped. As the oscillations decrease in magnitude the nonlinear gain increases and the M-point returns to the stability curve. Eventually a dynamic equilibrium is reached and a stable limit cycle results. At the intersections of the M-point locus and the stability curve Eq. (A-19) and Eq. (A-23) are equivalent and, therefore,

$$\omega_n^4 - 14\omega_n^2 + 30 = 0. \tag{A-25}$$

The solutions to Eq. (A-25) are:

$$\omega_n = 1.63 \text{ rad/sec} \tag{A-26}$$

and

$$\omega_n = 3.37 \text{ rad/sec}. \tag{A-27}$$

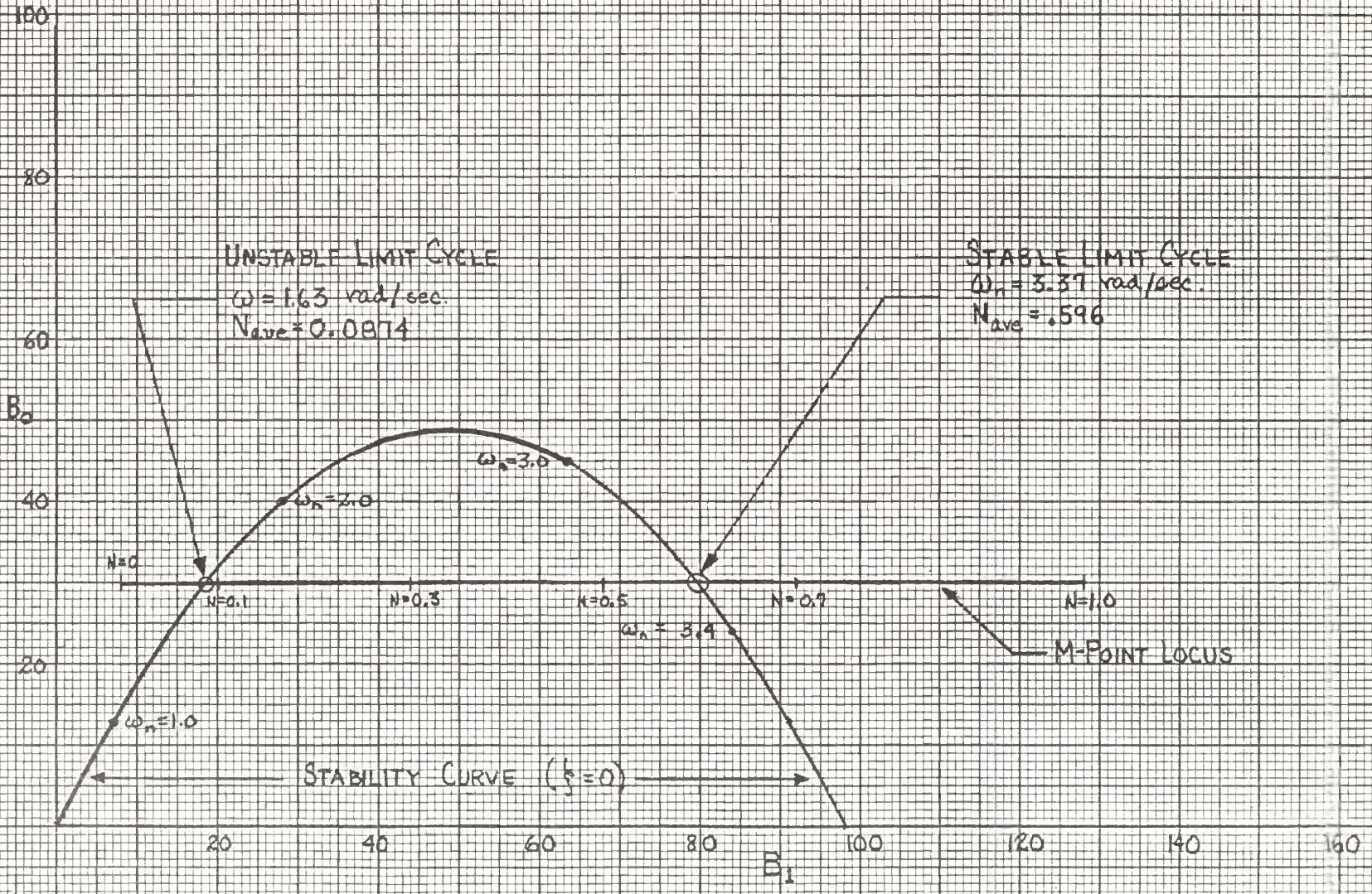

Figure A-6. Graphical solution for saturation in tachometer feedback channel.

At each intersection of the M-point locus Eqs. (A-25) and (A-26) are equivalent and

$$120N = 7\omega_n^2 - 8. \tag{A-28}$$

For the stable limit cycle, using the value of ω_n from Eq. (A-27), the solution of Eq. (A-28) is N equals 0.596. For the unstable limit cycle Eq. (A-26) applies and the solution to Eq. (A-28) is N equals 0.0874.

The unstable limit cycle results when the magnitude of the velocity feedback signal is large enough to produce saturation such that N is equal to or less than 0.0874. This condition will exist for any magnitude of $\dot{\theta}$ equal to or greater than 5.73 rad/sec, a value derived from the following equation:

$$N = \frac{3}{6|\dot{\theta}|} < 0.0874. \tag{A-29}$$

For any $\dot{\theta}$ whose magnitude satisfies Eq. (A-29), the system is unstable and the oscillations begin to grow. This increase in the magnitude of $\dot{\theta}$ further reduces the value of N and the oscillations continue to greater magnitudes. Fig. A-7 is a phase portrait of this system showing operation at both limit cycles.

It is emphasized here that the operation of the system at either limit cycle is <u>not</u> in a small region about the intersection of the stability curve and the M-point locus. As the value of $\dot{\theta}$ passes through zero in either direction, the value of N is one, since the velocity feedback channel is not saturated. Thus, the instantaneous values of N cause the system to operate through a long portion of the M-point locus. The unstable limit cycle, for example, would produce values of B_A between eight and 128.

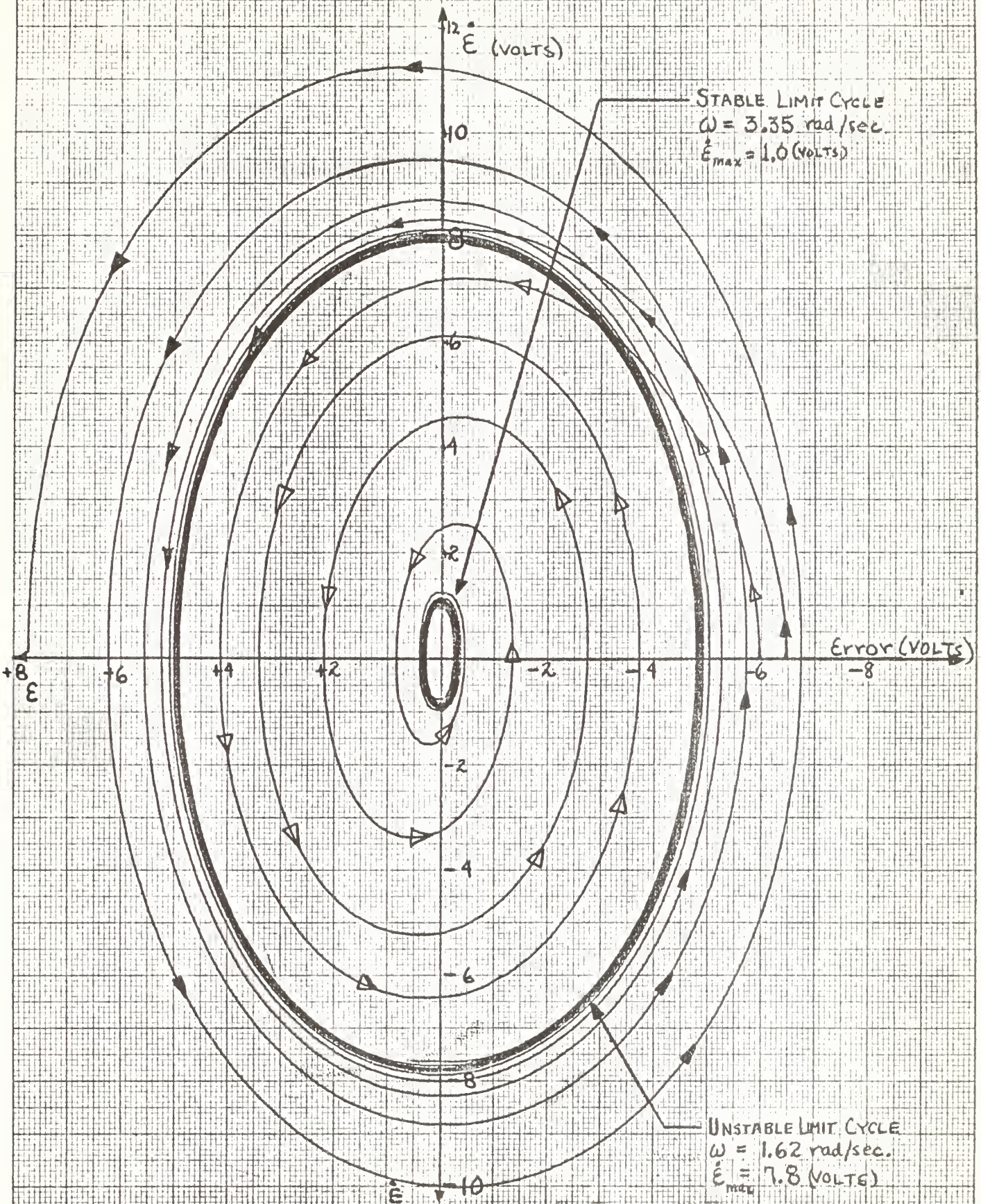

Figure A-7. $\dot{\varepsilon}$ vs ε phase portrait. Velocity channel feedback saturation.

CASE III SATURATION IN THE ACCELERATION FEEDBACK CHANNEL.

The block diagram of the system to be analyzed and the analog computer simulation of the system are shown in Fig. A-8. The closed loop transfer function of the system was found from which the characteristic equation is:

$$S^4 + 7S^3 + (14 + 10N)S^2 + 8S + 20 = 0 \qquad (A\text{-}30)$$

where,

$$B_1 = 8 \qquad (A\text{-}31)$$

and,

$$B_2 = 14 + 10N. \qquad (A\text{-}32)$$

The B_1 B_2 Mitrovic equation pair are selected from Appendix F. With the correct coefficients from Eq. (A-30) and the $\phi(\xi)$ functions for $\xi = 0$, the parametric equations for the stability curve are:

$$B_1 = 7\omega_n^2 \qquad (A\text{-}33)$$

$$B_2 = \frac{20}{\omega_n^2} . \qquad (A\text{-}34)$$

At the intersection of the M-point locus and the stability curve Eqs. (A-31) and (A-33) are equivalent. Therefore, $\omega_n = 1.069$ rad/sec. For this value of ω_n, B_2 equals 18.64, from Eq. (A-34), and N equals 0.464, from Eq. (A-32).

The graphical solution to this problem is shown in Fig. A-9. If the magnitude of the acceleration signal is large enough such that N is less than 0.464, then the system is unstable and oscillations increase in magnitude. This increases the peak magnitude of the acceleration signal, reduces the magnitude of N, and causes the system to become more unstable. Therefore the system will never attain a stable state.

For small signal magnitudes of acceleration the system operates near

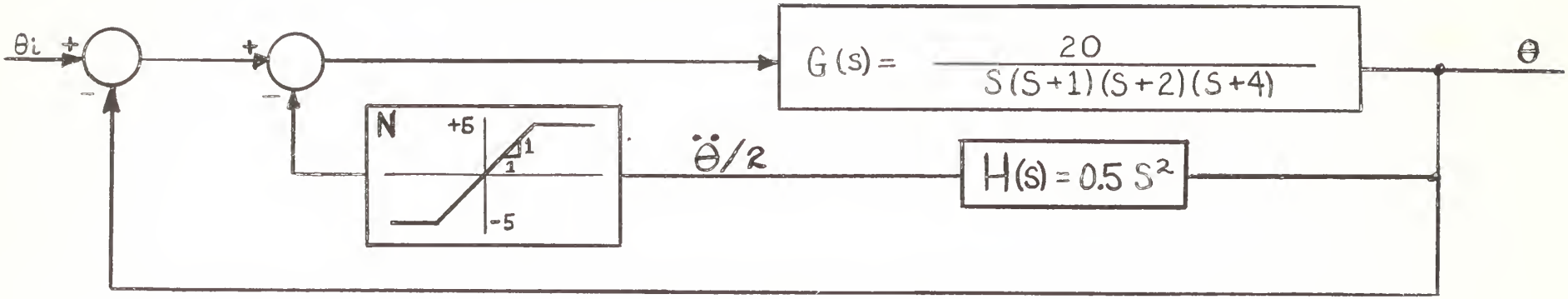

(a) System block diagram.

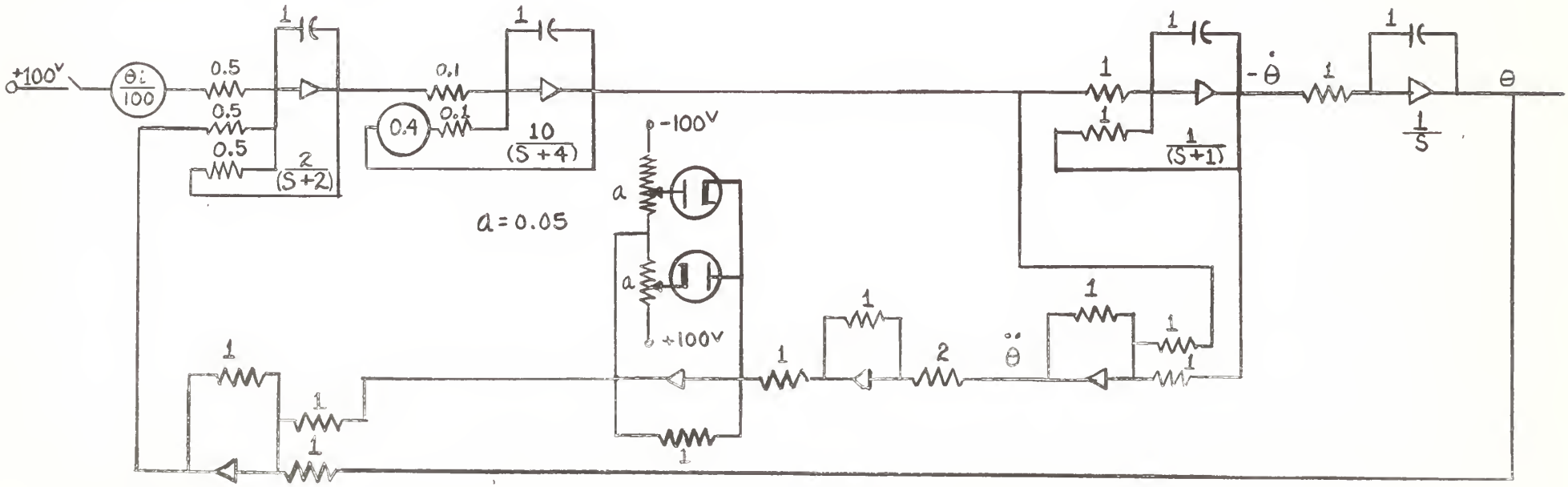

(b) Computer simulation. (Resistance in megohms, capacitance in microfarads).

FIGURE A-8

Control system with saturation in acceleration feedback channel

the point where N is unity. In this region the system has some damping ratio, ζ, greater than zero. As the oscillations are decreased in magnitude, the value of N approaches unity. In this mode of operation the oscillations will eventually die out and the system will operate in a linear, stable state. Fig. A-10 is a phase portrait of this system which illustrates the stable mode of operation, the unstable limit cycle, and the unstable mode of operation.

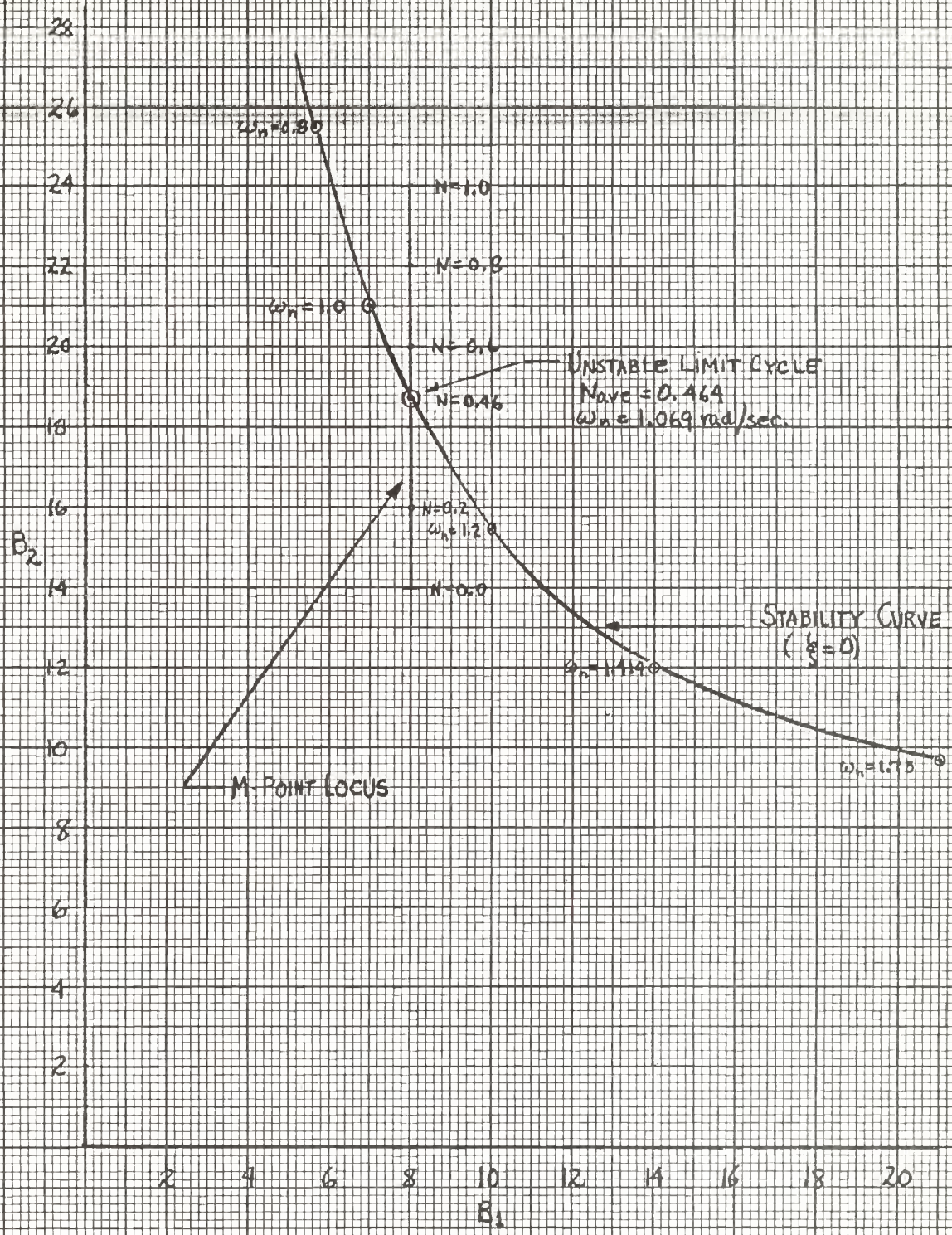

Figure A-9. Graphical solution for acceleration feedback channel saturation.

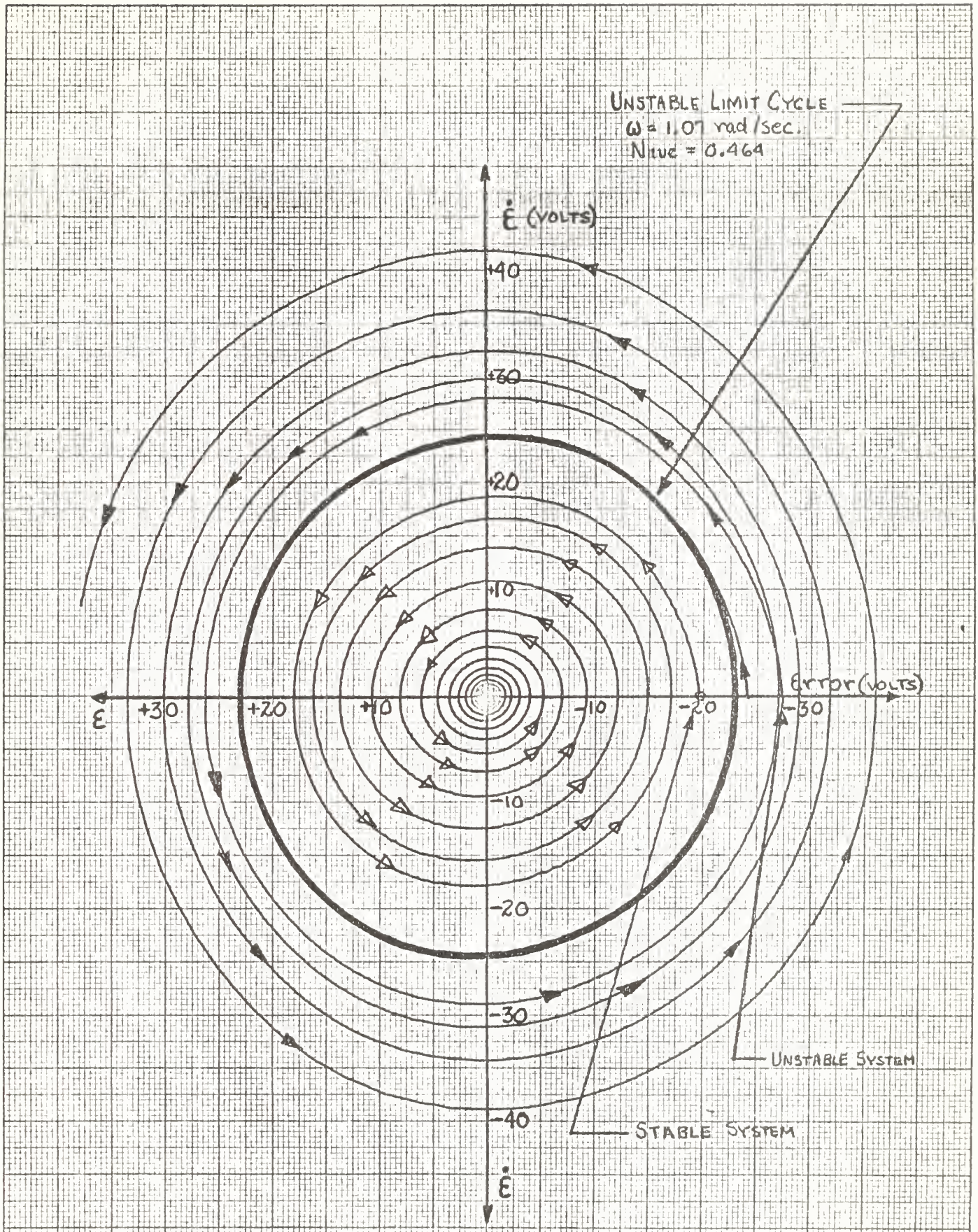

Figure A-10. $\dot{\epsilon}$ vs ϵ phase portrait. Acceleration feedback saturation.

TABLE [illegible] (Continued)

(1) $B_0 - B_1$

$$B_0 = -\left[A_2\omega_n^2\phi_1(\xi) + A_3\omega_n^3\phi_2(\xi) + \cdots + A_n\omega_n^n\phi_{n-1}(\xi)\right]$$

$$B_1 = A_2\omega_n\phi_2(\xi) + A_3\omega_n^2\phi_3(\xi) + \cdots + A_n\omega_n^{n-1}\phi_n(\xi)$$

(2) $B_0 - B_2$

$$B_0 = \frac{1}{\phi_2(\xi)}\left[A_1\omega_n\phi_1(\xi) + A_3\omega_n^3\phi_1(\xi) + A_4\omega_n^4\phi_4(\xi) + \cdots + A_n\omega_n^n\phi_{n-2}(\xi)\right]$$

$$B_2 = -\frac{1}{\omega_n^2\phi_2(\xi)}\left[A_1\omega_n\phi_1(\xi) + A_3\omega_n^3\phi_3(\xi) + A_4\omega_n^4\phi_4(\xi) + \cdots + A_n\omega_n^n\phi_n(\xi)\right]$$

(3) $B_0 - B_3$

$$B_0 = -\frac{1}{\phi_3(\xi)}\left[A_1\omega_n\phi_2(\xi) + A_2\omega_n^2\phi_1(\xi) - A_4\omega_n^4\phi_1(\xi) - \cdots - A_n\omega_n^n\phi_{n-3}(\xi)\right]$$

$$B_3 = -\frac{1}{\omega_n^3\phi_3(\xi)}\left[A_1\omega_n\phi_1(\xi) + A_2\omega_n^2\phi_2(\xi) + A_4\omega_n^4\phi_4(\xi) + \cdots + A_n\omega_n^n\phi_n(\xi)\right]$$

(4) $B_0 - B_4$

$$B_0 = \frac{1}{\phi_4(\xi)}\left[A_1\omega_n\phi_3(\xi) + A_2\omega_n^2\phi_2(\xi) + A_3\omega_n^3\phi_1(\xi) - A_5\omega_n^5\phi_1(\xi) - \cdots - A_n\omega_n^n\phi_{n-4}(\xi)\right]$$

$$B_4 = -\frac{1}{\omega_n^4\phi_4(\xi)}\left[A_1\omega_n\phi_1(\xi) + A_2\omega_n^2\phi_2(\xi) + A_3\omega_n^3\phi_3(\xi) + A_5\omega_n^5\phi_1(\xi) + \cdots + A_n\omega_n^n\phi_n(\xi)\right]$$

(5) $B_1 - B_2$

$$B_1 = -\frac{1}{\omega_n}\left[-A_0\phi_2(\xi) + A_3\omega_n^3\phi_1(\xi) + A_4\omega_n^4\phi_2(\xi) + \cdots + A_n\omega_n^n\phi_{n-2}(\xi)\right]$$

$$B_2 = \frac{1}{\omega_n^2}\left[-A_0\phi_1(\xi) + A_3\omega_n^3\phi_2(\xi) + A_4\omega_n^4\phi_3(\xi) + \cdots + A_n\omega_n^n\phi_{n-1}(\xi)\right]$$

[illegible] ξ [illegible]

[illegible] ξ [illegible]

(6) $B_1 - B_3$

$$B_1 = \frac{1}{\omega_n \phi_2(\xi)}\left[-A_0\phi_3(\xi) - A_2\omega_n^2\phi_2(\xi) + A_4\omega_n^4\phi_1(\xi) + \cdots + A_n\omega_n^n\phi_{n-3}(\xi)\right]$$

$$B_3 = -\frac{1}{\omega_n^3\phi_2(\xi)}\left[A_0 + A_2\omega_n^2\phi_1(\xi) + A_4\omega_n^4\phi_3(\xi) + \cdots + A_n\omega_n^n\phi_{n-1}(\xi)\right]$$

(7) $B_1 - B_4$

$$B_1 = \frac{1}{\omega_n \phi_3(\xi)}\left[-A_0\phi_4(\xi) - A_2\omega_n^2\phi_2(\xi) - A_3\omega_n^3\phi_1(\xi) + A_5\omega_n^5\phi_1(\xi) + \cdots + A_n\omega_n^n\phi_{n-4}(\xi)\right]$$

$$B_4 = -\frac{1}{\omega_n^4\phi_4(\xi)}\left[A_0 + A_2\omega_n^2\phi_1(\xi) + A_3\omega_n^3\phi_2(\xi) + A_5\omega_n^5\phi_4(\xi) + \cdots + A_n\omega_n^n\phi_{n-1}(\xi)\right]$$

(8) $B_2 - B_3$

$$B_2 = \frac{1}{\omega_n^2}\left[-A_0\phi_3(\xi) - A_1\omega_n\phi_2(\xi) + A_4\omega_n^4\phi_1(\xi) + A_5\omega_n^5\phi_2(\xi) + \cdots + A_n\omega_n^n\phi_{n-3}(\xi)\right]$$

$$B_3 = \frac{1}{\omega_n^3}\left[-A_0\phi_2(\xi) - A_1\omega_n\phi_1(\xi) + A_4\omega_n^4\phi_2(\xi) + \cdots + A_n\omega_n^n\phi_{n-2}(\xi)\right]$$

(9) $B_2 - B_4$

$$B_2 = \frac{1}{\omega_n^3\phi_2(\xi)}\left[-A_0\phi_4(\xi) - A_1\omega_n\phi_3(\xi) - A_3\omega_n^3\phi_1(\xi) + A_5\omega_n^5\phi_1(\xi) + \cdots + A_n\omega_n^n\phi_{n-4}(\xi)\right]$$

$$B_4 = -\frac{1}{\omega_n^4\phi_2(\xi)}\left[-A_0\phi_2(\xi) - A_1\omega_n\phi_1(\xi) + A_3\omega_n^3\phi_1(\xi) + A_5\omega_n^5\phi_3(\xi) + \cdots + A_n\omega_n^n\phi_{n-2}(\xi)\right]$$

(10) $B_3 - B_4$

$$B_3 = \frac{1}{\omega_n^3\phi_1(\xi)}\left[-A_0\phi_4(\xi) - A_1\omega_n\phi_3(\xi) - A_2\omega_n^2\phi_2(\xi) + A_5\omega_n^5\phi_1(\xi) + \cdots + A_n\omega_n^n\phi_{n-4}(\xi)\right]$$

$$B_4 = -\frac{1}{\omega_n^4\phi_1(\xi)}\left[-A_0\phi_3(\xi) - A_1\omega_n\phi_2(\xi) - A_2\omega_n^2\phi_1(\xi) + A_5\omega_n^5\phi_2(\xi) + \cdots + A_n\omega_n^n\phi_{n-3}(\xi)\right]$$

* ---Singularity at $\xi = 0.0$

** ---Singularity at $\xi = 0.5$

TABLE II. Equations for the $\phi_k(\xi)$ functions appearing in [illegible]

$$\phi_0(\xi) = 0$$

$$\phi_1(\xi) = -1$$

$$\phi_2(\xi) = 2\xi$$

$$\phi_3(\xi) = 1 - 4\xi^2$$

$$\phi_4(\xi) = -4\xi + 8\xi^3$$

$$\phi_5(\xi) = -1 + 12\xi^2 - 16\xi^4$$

$$\phi_6(\xi) = 6\xi - 32\xi^3 + 32\xi^5$$

$$\phi_7(\xi) = 1 - 24\xi^2 + 80\xi^4 - 64\xi^6$$

$$\vdots$$

$$\phi_K(\xi) = -\left[2\xi\phi_{K-1}(\xi) + \phi_{K-2}(\xi)\right] \quad \text{for } K \geq 2$$

BIBLIOGRAPHY

1. Mitrovic, Dusan., Graphical Analysis and Synthesis of Feedback Control System. Part I - Theory and Analysis. AIEE Transactions Part II (Applications and Industry), Vol. 77, 1958 (Jan. 1959 Section) : 476-487.

2. Mitrovic, Dusan., Graphical Analysis and Synthesis of Feedback Control Systems. Part II - Synthesis. Ibid. 487-496.

3. Thaler, G. J. and Brown, R. G., Analysis and Design of Feedback Control Systems. McGraw-Hill, 1960.

4. Thaler, G. J. and Pastel, M. P., Analysis and Design of Nonlinear Feedback Control Systems. McGraw-Hill, 1962.

5. Thaler, G. J. and Ohta, T., Mitrovic's Method - Some Fundamental Techniques. United States Naval Postgraduate School, Research Paper, No. 39, January 1964.

6. United States Naval Postgraduate School. Use of Mitrovic's Method in Predicting Limit Cycles in Feedback Control Systems with One and Two Coin Variable Nonlinearities by LT P. L. Wilson, USN. May 1964.